THERMOMECHANICAL MODELING OF STRESS DEVELOPMENT AND PHASE EVOLUTION DURING COOLING OF CONTINUOUSLY-CAST BORON-CONTAINING STEEL

by

Duo Huang

A Dissertation

Submitted to the Faculty of Purdue University

In Partial Fulfillment of the Requirements for the degree of

Doctor of Philosophy

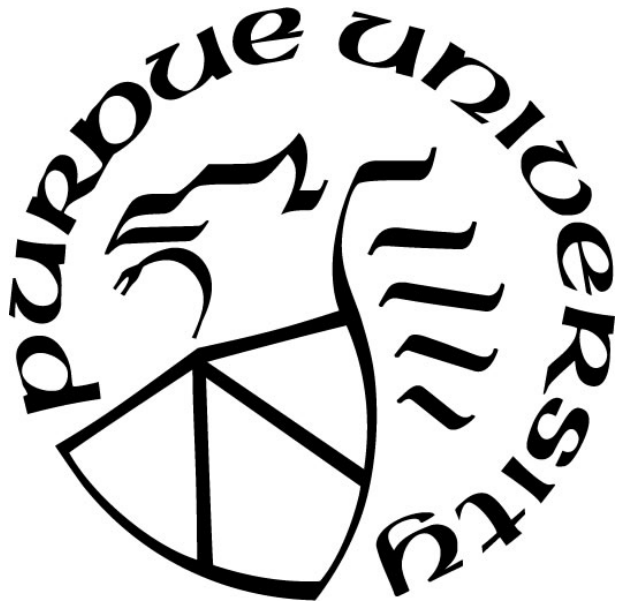

School of Materials Engineering

West Lafayette, Indiana

May 2022

THE PURDUE UNIVERSITY GRADUATE SCHOOL
STATEMENT OF COMMITTEE APPROVAL

Dr. David R. Johnson, Co-Chair
School of Materials Engineering

Dr. Matthew J. M. Krane, Co-Chair
School of Materials Engineering

Dr. Michael S. Titus
School of Materials Engineering

Dr. Lia A. Stanciu
School of Materials Engineering

Approved by:
Dr. David Bahr

This work is dedicated to my parents, Lin Huang and Huirong Wang.

ACKNOWLEDGMENTS

First and foremost, I would like to express my gratitude to my advisors, Professor David Johnson and Professor Matthew Krane, for their continuous support and advice on my academic development over the last six years. I am very grateful to Professor Johnson for spending time in the lab teaching me experimental techniques as well as those inspiring discussions. To Professor Krane, thank you for teaching me how to think as an engineer. I also want to thank my committee members: Professor Michael Titus, Professor Lia Stanciu, and Professor Maria Okuniewski for their valuable support, guidance, and patience throughout my entire PhD years.

I would also like to acknowledge the East Chicago (USA) Center of ArcelorMittal Global R&D for providing support for this work. Specifically, I would like thank Dr. Hongbin Yin for supporting this work and providing valuable insights and assistance.

I also want to thank my friends and colleagues in School of Materials Engineering, Dr. Kara Luitjohan, Dr. Yaohui Fan, Dr. Pengyu Xu, and Matthew Binkley for their help and support in my work and also my personal life. It is always a pleasure to work with you. My thanks also go to staff members of the MSE, Vicki Cline and Rosemary Son, for providing academic advising and support. My special thanks to Dr. Karen Morgan for her patience and valuable help in my last year.

Last but not least, I would express my deepest gratitude to my parents and family. Although we could only talk through video calls for years, you have always brought light and joy to my life. Without your love, encouragement and endless support, my graduate career would not have been possible.

TABLE OF CONTENTS

LIST OF TABLES

LIST OF FIGURES

NOMENCLATURE

Latin symbols

a_P	Diagonal coefficients in FVM solution matrix
a_N	Off-diagonal coefficients in FVM solution matrix
$[A]$	Solution matrix in FVM linear algebraic system
A_S	Surface area
$[b]$	Source vector in FVM linear system
b_i	Phase transformation kinetic parameter for phase i
c_p	Specific heat
$\boldsymbol{D}$	Displacement vector
$\boldsymbol{d}_f$	Vector between the center of control volume P and its neighbor N
E	Young's modulus of elasticity
$\boldsymbol{f}$	Body force vector
$\boldsymbol{g}$	Gravity vector
G	Growth rate
h	Convective heat transfer coefficient
H	Hardening modulus of linear isotropic hardening rule
$\mathbf{I}$	Identity tensor
k	Thermal conductivity
L_i	Latent heat of phase transformation for phase i
m	Mass of a slab
n_i	Phase transformation kinetic parameter for phase i
$\boldsymbol{n}$	Surface unit normal vector
N	Nucleation rate for isothermal pearlite formation
$\overline{Nu}_L$	Nusselt number
p	Pressure
Pr	Prandtl number
$P(T)$	Temperature dependent materials property

$\dot{Q}$	Latent heat release rate
$q"$	Heat flux
Ra_L	Rayleigh number
S	Scheil's sum
t	Time
Δt	Time step
T	Temperature
T_∞	Environmental temperature
T_{M_S}	Martensite starting temperature
X_i	Phase fraction of phase i
$X_F^{\max}$	Maximum fraction of ferrite that could form isothermally
X_F^{limit}	Maximum fraction of proeutectoid ferrite before pearlite transformation

Greek symbols

α	Thermal expansion coefficient
$\boldsymbol{\varepsilon}$	Strain tensor
$\boldsymbol{\varepsilon}^e$	Elastic strain tensor
$\boldsymbol{\varepsilon}^p$	Plastic strain tensor
$\boldsymbol{\varepsilon}^{th}$	Thermal strain tensor
$\boldsymbol{\varepsilon}^{ph}$	Phase transformation strain tensor
ε_p^{eq}	Effective plastic strain
ε	Emissivity
$\boldsymbol{\sigma}$	Cauchy stress tensor
$\boldsymbol{\sigma}^{dev}$	Deviatoric stress tensor
σ_Y	Yield strength
σ_f	Flow stress
σ	Stefan-Boltzmann constant
τ_0	Incubation time for diffusion-controlled phase transformation
Ω	Martensitic transformation constant
Ω_P	Cell volume

ν	Poisson's ratio
μ	Lamé constant
λ	Lamé constant
ρ	Density

Acronyms

CFD	Computational fluid dynamics
CV	Control volume
FVM	Finite volume method
FEM	Finite element method
GAMG	Generalized geometric-algebraic multi-grid solver
JMAK	Johnson-Mehl-Avrami-Kolmogorov kinetic equation

ABSTRACT

The automotive industry is using advanced high strength steels (AHSS) to improve the fuel efficiency of passenger vehicles by lightweighting strategy. The higher strength of AHSS allows vehicle manufacturers to implement thinner and lighter components while still meet the safety requirements. Press hardened steels (PHS) exhibit the highest tensile strength among AHSS and are widely used for manufacturing crash relevant automotive parts. Boron-containing steel with enhanced hardenability is the most commonly used grade of steel for press hardening. The addition of a small amount of boron, 0.002 – 0.005 wt.%, can effectively increase hardenability. However, the boron addition also causes problems in commercially production of steel slabs by continuous casting. Defects including transverse corner cracks, surface cracks, and internal halfway cracks are sometimes found in continuously-cast boron steel slabs during or after the final cooling process. These problems can arise during the post-casting cooling process because boron addition changes the phase transformation behavior of steel.

The cooling of slabs during and after continuous casting is a multiphysics process including coupled heat transfer, solidification, solid-solid phase transformations, and deformation. Numerical models are helpful for a better understanding of the cooling process and the interaction of different physical phenomena in it. In this work, a 3-D thermomechanical finite volume model (FVM) with coupled heat transfer, stress, and phase transformation calculations is developed to investigate the temperature history, phase evolution, and stress development during cooling.

The model is used to simulate the cooling process of continuous cast steel slabs at different post-casting stages. The effect of boron addition on stress development and phase evolution during cooling of a single slab is investigated via simulation of both boron-containing and non-boron steels. The results show the slab with boron consists of mostly bainite, in contrast to the non-boron grade which is mostly ferrite and pearlite after cooling. Higher tensile stresses, both peak and residual, and plastic strains, which could lead to cracking, are observed at the edge of slab in the boron-containing grade. The effect of slowing the cooling rate by using a radiation shield is studied for the boron-containing steel. The reduced thermal gradient and the increased ferrite formation reduce the stresses in the slab. The cooling process of a stack of multiple slabs is also simulated to study the influence of slabs stacking on cooling rate and slab deformation. A slower cooling rate can be achieved in stacked slabs and the compressive load provided by slabs above the slab can

prevent large deformation and flatten the slab during cooling. The combination of slab stacking and radiation shield is modeled to study the stress development under a slow cooling rate that is feasible in practice. Boron addition also affects the water quenching process of steel strips on the runout table after hot rolling. Simulations of strips with and without boron show different cooling curves, residual stress and phase distributions as austenite decomposition does not occur for boron-containing steel due to the fast cooling rate. Therefore, the cooling strategy on the runout table should be adjusted accordingly to control the coiling temperature and improve strip quality.

1. INTRODUCTION

1.1 Boron-containing advanced high strength steel

1.1.1 Press hardened steel

The automotive industry is facing the challenge of improving vehicles' safety and reducing the environmental impact caused by fuel emissions[1]. One effective way to achieve this goal is through vehicle lightweighting. By using advanced high strength steel (AHSS) to replace vehicle components made with conventional steels or cast iron, the fuel efficiency can be improved while requirements for safety are still met. There are a variety of steels with a range of mechanical properties that are developed and used in today's automotive industry for different applications as shown in Figure 1.1. Among all these grades of steels, martensitic steel (MS) and press hardened steel (PHS) exhibit the highest tensile strength which ranges up to 2000 MPa[1]. This high strength allows the use of PHS for thin wall designs in safety or structural components and hence can effectively reduce the weight of vehicles.

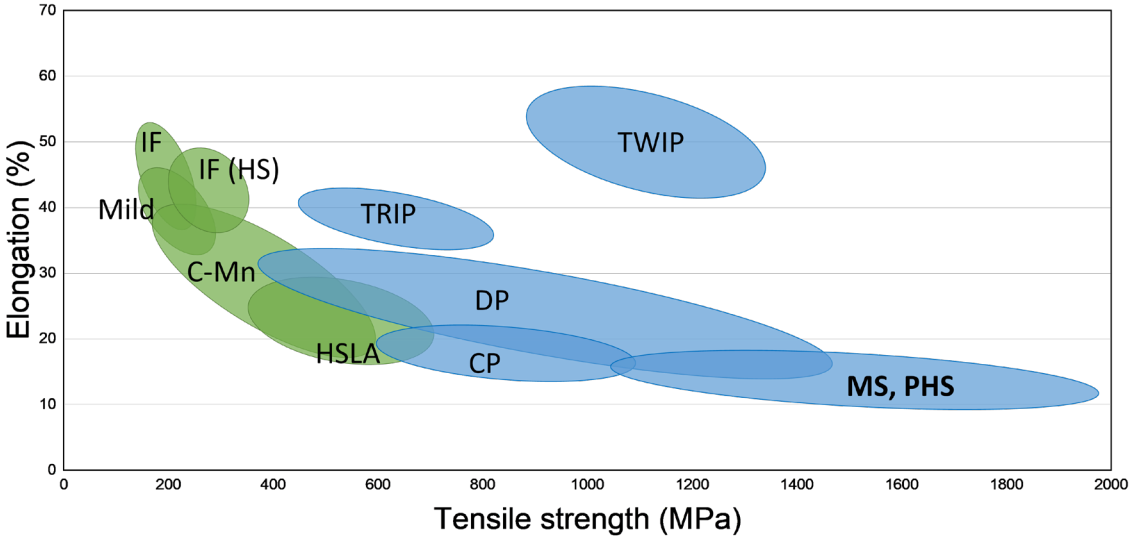

Figure 1.1. The steel strength versus ductility diagram illustrating the difference in mechanical properties among conventional steels and AHSS grades (after [1]).

Press hardened steel, also known as hot forming (HF) or hot stamping steel is a kind of quenchable micro-alloyed steel that is widely used for manufacturing crash relevant automotive

parts[2,3]. The schematic illustrating the press hardening process is shown in Figure 1.2. The as-received steel blank with a ferritic-pearlitic microstructure is heated up to above 900 ℃ and kept in furnace for at least 5 minutes to achieve fully austenitization. Afterwards, the austenitic blank at high temperature is transferred to the pressing die for forming and quenching. As the blank is in contact with the water-cooled die, it is formed and quenched simultaneously to achieve the final designed shape with a martensitic microstructure[4]. Comparing with traditional cold forming technologies, press hardening allows vehicle manufacturers to design and produce components with both high strength and complex geometry due to the martensitic microstructure and good formability at high temperatures.

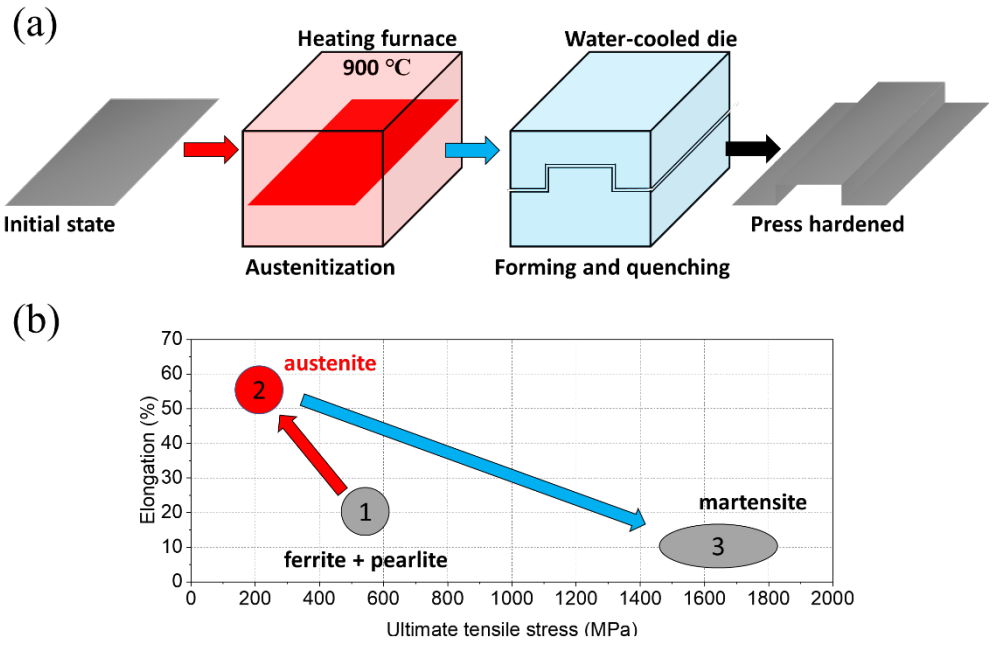

Figure 1.2. Summary of the press hardening process illustrating (a) the schematic processing procedure and (b) the evolution of microstructures and mechanical properties.

1.1.2 Boron-containing AHSS for press hardening

According to the procedure of press hardening, the key factor for a steel to be used in press hardening is its hardenability. Hardenability is defined as the capacity of a steel to suppress the diffusion-controlled phase transformations and transform from austenite to martensite during cooling[5]. Under the same cooling condition, a steel with good hardenability can transform to a higher fraction of martensite, producing a material with higher strength. Therefore, boron-

containing steel with enhanced hardenability, such as 22MnB5, 27MnCrB5, and 20MnB5, becomes the most commonly used grade of steel for press hardening[3]. For 22MnB5 steel, if the critical cooling condition of 27 K/s is exceeded, it will show a yield strength (YS) of 1000 MPa and an ultimate tensile strength (UTS) above 1400 MPa.

Boron acts as an excellent hardening agent in steel. The addition of a small amount of boron can effectively increase hardenability[6]. Luitjohan et al.[7] studied the effect of boron on microstructures of a ternary Fe-C-B alloy and found that the addition of less than 5 ppm of boron resulted in the formation of bainite instead of ferrite and pearlite. In contrast, other alloying elements used for improving hardenability such as Mo, Ni, and Mn will need more than 0.5% addition to show an equivalent increase[8]. Boron addition enhances hardenability by the segregation of boron to austenite grain boundaries, delaying the nucleation and growth of ferrite[5]. The effect of boron is most effective for low carbon steels as the major phase after austenite transformation is soft ferrite. The time-temperature-transformation (TTT) diagram shifts to the right (longer time) for a low carbon steel with boron addition as shown in Figure 1.3. Less than 0.003 wt.% of boron can result in this significant improvement in hardenability. With increasing carbon content, the effect of boron becomes less significant as there is less ferrite formation for boron-containing steel.

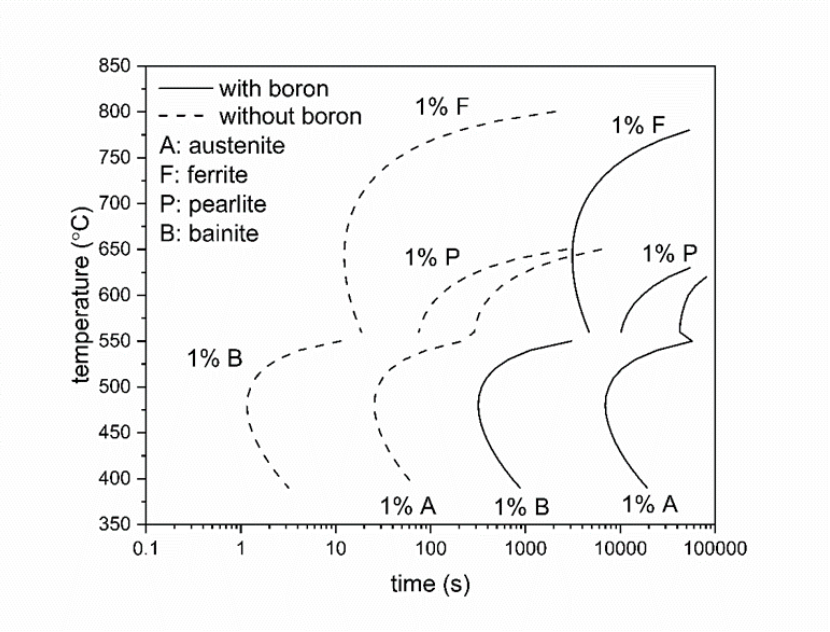

Figure 1.3. TTT diagram of a low carbon steel with 0.003 wt.% of boron and without boron addition predicted by JMatPro, showing that the boron addition effectively shifts the TTT diagram to right.

1.2 Continuously-cast boron steel slabs

Although the addition of boron does significantly improve hardenability of steel and makes it suitable for the press hardening process, it also causes problems in commercial production of steel slabs by continuous casting. Despite the small level of B addition, defects including transverse corner cracks, surface cracks, and internal halfway cracks are sometimes found in continuously-cast boron steel slabs during or after the final slab cooling process[9,10].

1.2.1 Continuous casting of steel slabs

The use of continuous casting for steelmaking dates back to the 1960s and it has grown into the most commonly used casting method for steel due to its advantages in steel quality and better yield. Nowadays, more than 95% of steel production over the world is by continuous casting[11]. As illustrated in Figure 1.4, the molten steel flows into the mold and forms a solidified shell at the metal/mold interface. At the exit of the mold, the shell grows thick enough to hold the liquid steel inside. Afterwards, the steel strand is cooled by spray water in the secondary cooling zone until the core is fully solidified and guided by the rollers to the caster exit. At the end of caster, the strand is cut off by torch and sent to slab yard for further cooling.

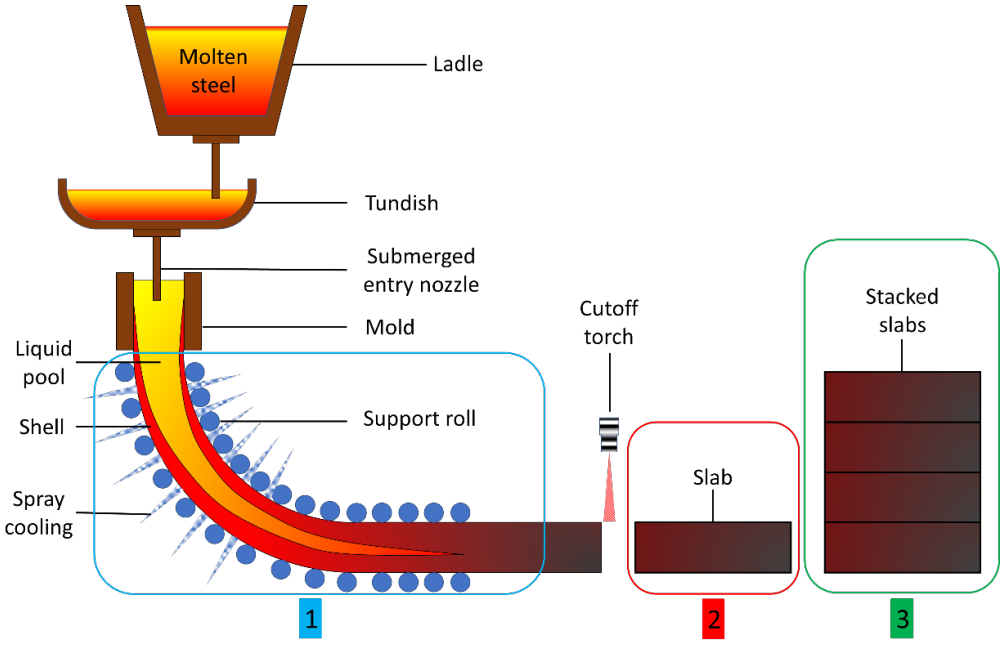

Figure 1.4. Schematic of continuous casting process. Section 1 is the secondary cooling zone. Section 2 and 3 is the cooling after casting for single slab and stacked slabs, respectively (after [12]).

1.2.2 Investigation of cracking in continuously-cast boron steel slabs

One of the most common casting defects in continuously-cast steel slabs is cracking. The slab is only "semi-finished" after casting and requires subsequent hot rolling, but even small cracks can propagate during rolling and severely affect the quality of rolling products. Brimacombe and Sorimachi [13] examined different types of cracks that can initiate during continuous casting. As shown in Figure 1.5, they can be found in many locations on the slab. For the slab surface, both transverse and longitudinal cracks are found in corners and midface. Inside of the slab, cracking can occur along the centerline or diagonal of the cross section.

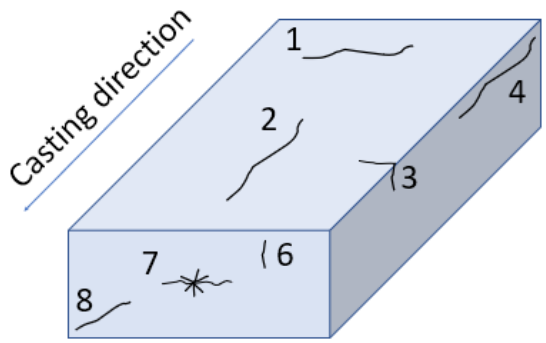

	Surface cracks
1	Transverse mid-face crack
2	Longitudinal mid-face crack
3	Transverse corner crack
4	Longitudinal corner crack
	Internal cracks
6	Midway crack
7	Centerline crack
8	Diagonal crack

Figure 1.5. Schematic of different types of cracks found in continuously-cast slabs (after[13]).

For boron-containing steel slabs, the effect of boron on crack formation has been studied with focuses on microstructures, high temperature mechanical properties, and phase transformation. Yin et al.[9,14] found that the cracking could stem from the remelting at the interdendrtic regions. The authors studied the phase diagrams provided by ThermoCalc for the Fe-B-C system and found a metatectic reaction induced by B addition, as shown in Figure 1.6. The metatectic reaction ($\delta \rightarrow \gamma + L$) can occur at T_R when B composition C_0 is between C_S and C_R. With B addition as low as 5 ppm, a low melting Fe-B phase could exist as a liquid phase at 1100 °C. This phase diagram prediction was supported by Luitjohan et al.[15] through their experimental investigation of Fe-B alloys with different B concentrations. They used confocal scanning laser microscopy to achieve in-situ observation of microstructure changes at high temperatures during

heating and cooling process. The evidence for metatectic reaction was observed as the liquid phase solidified ($\gamma + L \rightarrow \delta$) during heating and solid phase remelted ($\delta \rightarrow \gamma + L$) during cooling.

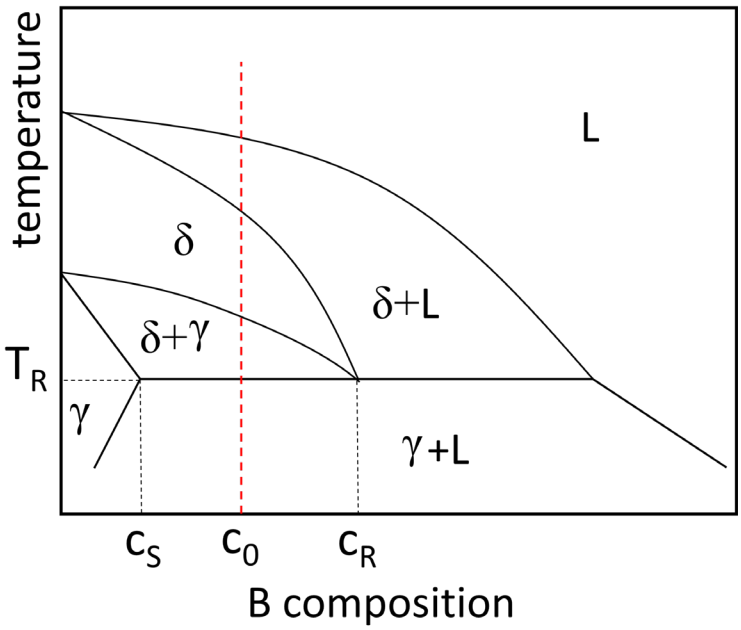

Figure 1.6. Partial binary equilibrium phase diagram for Fe-B alloy showing a typical metatectic reaction occurring at temperature T_R when B composition is C_R.

Crack formation at high temperatures during the continuous casting process is closely related to the hot ductility of steel. The role of boron addition on hot ductility is complicated as opposite effects has been reported, based on different mechanisms. On one hand, boron addition can improve the hot ductility of steel and be beneficial for the surface quality of slabs[16–19]. For low carbon steel without boron, a typical hot ductility trough can be observed from 700 ℃ to 1000 ℃ with the presence of filmlike pro-eutectoid ferrite forming along the austenite grain boundaries. With boron addition, the ferrite formation is delayed and thus the grain boundary cohesion is enhanced. López-Chipres et al. [18] conducted tensile tests at 700, 800, 900, and 1000 ℃ and the only hot ductility trough was found at 800 ℃. The authors found that with B addition from 29 ppm to 105 ppm, the hot ductility of a microalloyed steel was improved up to 25%.

On the other hand, boron-containing steel slabs are susceptible to cracking, especially at slab surface and corners[20–23]. Cho et al.[20] studied the behavior of boron precipitation under different cooling rates and their corresponding effects on hot ductility. For a steel with 27 ppm B

addition, with increasing cooling rates from 1 to 20 °C/s, the hot ductility decreased by 50% in regards of reduction of area for the tensile tests. The major cause of this ductility drop is the precipitation of boronitrides (BN). As cooling rate increases, BN precipitates become finer and more numerous along prior austenite grain boundaries. Under tensile stress, the interface between these precipitates and the grain are sites for microvoids generation which then leads to microvoid coalescence and intergranular cracking[22]. The effect of BN can be controlled by adding other alloying elements to tailor the distribution and morphology of precipitates. Cho et al.[21] found that BN precipitated preferentially inside the austenite grain instead of grain boundaries when small amount of Nb and Ti was added. The strain localization at grain boundaries were reduced and hence the hot ductility was improved.

Therefore, the role of boron addition in hot ductility and crack formation depends on where boron exists in the steel. If boron exists as a solute, it can help improve the hot ductility. However, if B precipitates as BN at austenite grain boundaries, it can be harmful and result in crack formation and propagation.

1.3 Thermomechanical modeling of cooling process for steel slabs

Having identified the effect of B addition on microstructures and hot ductility of continuously-cast boron steel slabs, focus is shifted to the study of stress development during continuous casting and the subsequent cooling process. As boron steel slabs become susceptible to cracking, certain levels of stress are critical for crack initiation and propagation. The cooling of slabs during and after continuous casting is a multiphysics process including coupled heat transfer, solidification, solid-solid phase transformations, and deformation. To help investigate this complicated problem, thermomechanical modeling has been utilized as a powerful tool for thermal-stress analysis. Beginning in the 1970s, Brimacombe and his coworkers [24,25]first introduced finite element models to study the stress distribution of the solidifying steel strand below the mold, where it is cooled by water spray in the secondary cooling zone. These early works mainly provided a qualitative understanding of stress distributions under different processing conditions[26]. This approach of using computational thermomechanical modeling for continuous casting has inspired other researchers to develop more sophisticated models to study multiple physics fields and their interactions.

The continuous cast steel slabs could undergo three different cooling processes before manufactured into final strip products: (1) cooling of the steel strand in the mold and secondary cooling zone at the caster exit; (2) subsequent air cooling in the slab yard; (3) cooling on the runout table after hot rolling process. All three stages could induce cracking in the slabs.

1.3.1 Cooling in the mold and secondary cooling zone

The cooling process in the mold and secondary cooling zone has been a focus for researchers investigating cracking problems in continuous cast slabs. Compared to subsequent cooling of slabs downstream of the caster, a relatively fast cooling rate is achieved in the water-cooled mold and the secondary cooling zone by the water spray cooling system. To prevent breakout of the liquid core, the cooling rate must be maintained at a certain level to ensure the solidifying shell thickness is sufficient to support the liquid core.

The liquid steel cools and solidifies to form the solid shell inside the copper mold. The schematic of heat transfer in the mold is shown in Figure 1.7[27]. It consists of two zones of cooling: (1) meniscus cooling with direct contact between mold and steel and (2) air gap cooling. The air gap forms because of the thermal shrinkage of the solidified shell and has a significant effect on the cooling condition. The typical surface heat transfer coefficient decreases from a peak value of 1500 to 2000 $Wm^{-2}K^{-1}$ at the meniscus to 600 to 800 $Wm^{-2}K^{-1}$ at the mold exit with the air gap.

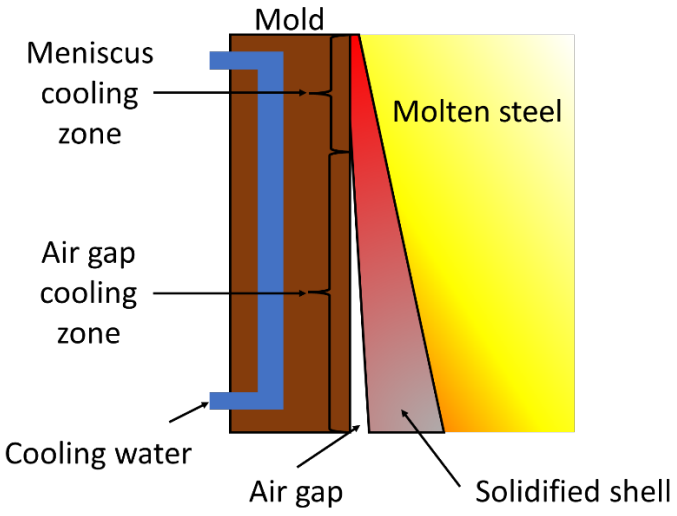

Figure 1.7. Schematic of cooling zones in the mold for continuous cooling (after [27]).

Thermomechanical models have been developed and applied to simulate the complex behaviors of steel shell during mold cooling. The majority of the numerical models are based on the finite element method (FEM) to compute heat transfer, solidification, and mechanical fields. Following the work of Brimacombe and his coworkers[24,25], Grill et al.[28] developed a 2D FEM model that treat the slab as a transverse slice passing through the mold, normal to the casting direction. By simplifying the problem to a 2D case, heat conduction in the casting direction was neglected and a plane stress condition was adopted for the stress calculation. Their model assumed the deformation of slab was elastoplastic and modeled the temperature dependent mechanical properties. The major advantage of the model is that it treated the heat transfer and deformation calculation as coupled phenomena. The heat transfer boundary conditions included the effect of the calculated shell deformation and gap size. The stress calculation was then computed from the updated temperature field.

Because the mold cooling of steel is a complicated process governed by multiple coupled phenomena including fluid flow, heat transfer, solidification and deformation, a multiphysics approach to simulate all these phenomena simultaneously is necessary for understanding the realistic problems[29]. Lee et al.[30] developed their model by iteratively coupling a 3D finite volume model (FVM) for fluid flow, heat transfer and solidification with a 2D FEM model for deformation behavior. The model was applied to stress development, gap formation and crack forming probability calculation for a continuous cast beam blank with complex geometry.

As the shell solidifies in the mold, it is withdrawn at the casting speed to the secondary cooling zone. The purpose of secondary cooling zone is to continue the solidification at the strand core. Figure 1.8 illustrates the four cooling mechanisms in the secondary cooling zone including roll contact conduction, spray water impinging, film boiling convection, radiation and air convection from the bare strand surface. As casting proceeds, the slabs undergo nonuniform cooling conditions at different cooling regions along the casting direction periodically. During cooling, the slabs are under both thermal and mechanical loads caused by thermal gradient and the bending/straightening operation by the rollers, respectively. Casting defects such as surface cracks and transverse corner cracks may occur during this stage. Thermomechanical models have been developed and applied to simulate the complex behaviors of steel strands during secondary cooling.

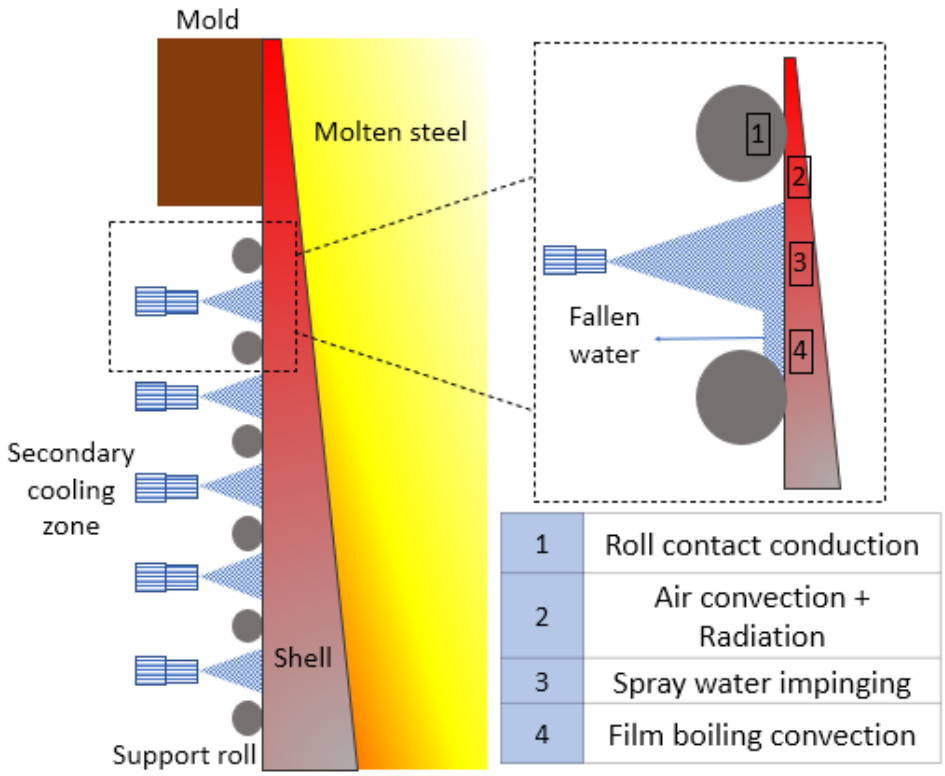

Figure 1.8. Schematic of cooling modes in the secondary cooling zone (after [27]).

Two dimensional models have been widely used for simplification and saving computational time. Both transverse section and longitudinal section models are developed for heat transfer and stress calculation. Chen et al.[31] applied a 2D transient thermal-elastoplastic FEM model to study the effect of process parameters in secondary cooling of a slice of a beam blank as it passed through the process. Janik et al.[32] used a 2D thermomechanical model to predict shell deformation with the liquid steel hydrostatic pressure taken into consideration. These works selected a transverse slice of the strand for simulation and ignored the deformation and stress along the casting direction. Bellet and Heinrich[33] developed a 2D model based on the longitudinal slice to study the temperature, deformation and stress along the whole continuous casting machine. The longitudinal slice method also has drawbacks as the difference in width direction is neglected. As the strand corner with large thermal gradient is susceptible to transverse corner cracks, the analysis of stress concentration there is important. Therefore, 3D models for mechanical field calculation are essential for stress development and crack formation studies, justifying their larger computation cost.

Yu et al.[34] established a combined 3D-2D model to investigate the effect of corner structure of steel strand on corner stress concentration. The model adopted a 2D heat transfer model for secondary cooling zone as the transverse slice moved along the casting direction. The temperature profile of slice at different locations are combined and transferred to a 3D thermomechanical model for stress calculation.

1.3.2 Air cooling in the slab yard

In addition to mold and secondary cooling, the subsequent air cooling process can also introduce cracking problems. Slabs exit the secondary cooling zone with surface temperatures at around 800 °C and are then transported by crane to a slab yard for further cooling. Depending on local practice, the slabs may cool down to ambient temperature before being reheated prior to rolling. Slab bowing, surface and corner cracks are observed often after cooling. Although the cooling rate of radiation and convection in air is relatively slow, austenite phase transformation to ferrite, pearlite and bainite phases occurs during this final cooling process. The temperature gradient across the slab and phase transformations can still cause stress and strain development. Therefore, a thermomechanical model can be used to simulate the thermomechanical and metallurgical behaviors of slabs during cooling.

The yard cooling of continuously-cast steel slabs is a multiphysics process including coupled heat transfer, phase transformations, and deformation. In order to simulate all the physical events simultaneously, the model should consider thermal, metallurgical, and mechanical phenomena occurring during the air cooling process. The interactions of heat transfer, phase evolution, and stress development are considered, as illustrated by Figure 1.9. The metallurgical field is calculated based on the temperature history from thermal field while it also affects heat transfer calculation by latent heat of transformation and phase dependent thermal properties. The mechanical field interacts with the metallurgical field by transformation strain and phase dependent mechanical properties.

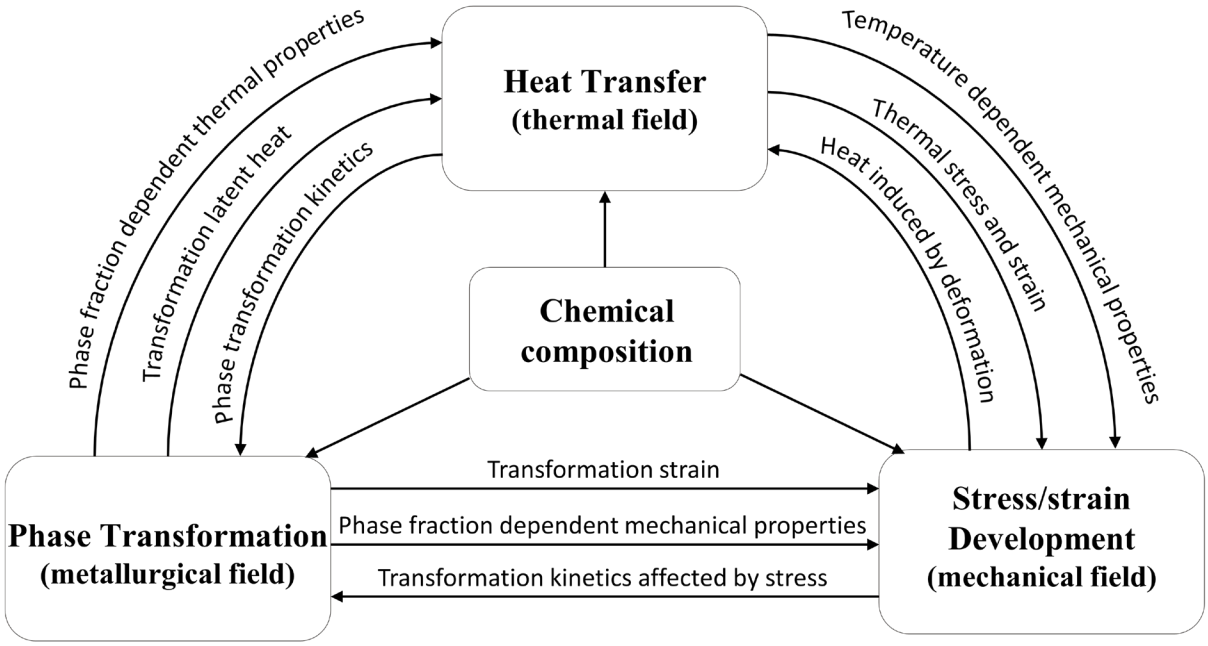

Figure 1.9. Physical fields and interactions occurring during cooling (after[35]).

There have been numerous research studies using numerical simulation to investigate the cooling process of steel with phase transformations. In 1975, Inoue and Tanaka[36] published an elastoplastic stress model with thermal strain and phase transformation based on finite element formulation to calculate residual stress after water quenching of steel. Denis et al.[37] reviewed the interactions between mechanical field and phase transformation. The effect of stress state on martensite transformation was taken into consideration and examined experimentally. Gür and Tekkaya[38,39] developed a FEM model to predict stress and strain field, phase evolution and temperature history during quenching of small steel components. Later, Şimşir and Gür[40] presented a 3D thermomechanical FEM model with phase transformations to simulate the quenching process of a plain carbon steel and the predicted residual stresses and phase distributions are proved to show good accuracy compared with experimental measurements. Allazadeh and Garcia[41] established a FEM technique to study the effect of cooling rate on the continuously cooling of a low carbon steel and concluded that the high stress developed during cooling has a direct relationship with fast cooling rate and phase transformation.

Thermomechanical modeling is widely used for steel in fast-cooling process such as quenching. The fast cooling rate can induce high thermal gradients and non-uniform phase distribution that cause distortion, residual stress, and cracking. For air cooling of large continuous cast steel slabs, a thermomechanical model with phase transformations is also a useful tool. To investigate the cooling process, experiments can show final solid phase distributions and residual stresses and strains in a slab, but the path to that final state is difficult or impossible to observe. Stress development simulation can be used to address peak stress concentration during cooling at any part of the slab. Wikström et al.[42] simulated the cooling process of slabs with a hood to slow the cooling rate and investigated the stress development. The simulation results showed that the stresses were high during phase transformation, but no cracking problems were predicted for the low carbon steel.

For continuous cast boron steel slabs, phase transformation is the key factor that affects the stress development during air cooling. As illustrated by the change in the TTT diagram in Figure 1.3, when boron is added to the steel, it changes the phase transformation behavior and thus the stress development. For slabs under the same cooling conditions, a boron-containing steel will exhibit phase transformation behaviors different than the non-boron steel.

1.3.3 Cooling on the runout table after hot rolling

Continuously-cast steel slabs are semi-finished and need to be hot rolled to produce flat products such as strips. A conventional hot rolling mill consists of a reheating furnace, roughing and finishing mills, a runout table, and a down coiler. Being sequentially rolled by the roughing and finishing mills, a slab becomes a strip with a thickness in a range from below 1 mm up to 25 mm. The strips exit the last finishing mill at temperatures ranging from 800 to 950 ℃ and is then transferred to the runout table for water quenching. The cooling system on runout table is controlled to cool the strips down to 450 to 750 ℃ before coiling[43]. Figure 1.10(a) shows a schematic of a runout table system. A typical runout table with a length of 50 to 100 m consists of a set of multiple rows of cooling jets above and below the strips, and an array of rollers for strip support and movement[44]. The controlled cooling on a runout table has a significant influence on the microstructures, mechanical properties, flatness, and residual stress of as-coiled strip products[45–47]. The understanding of the cooling mechanisms on runout table is fundamental to precise temperature control and quality improvement.

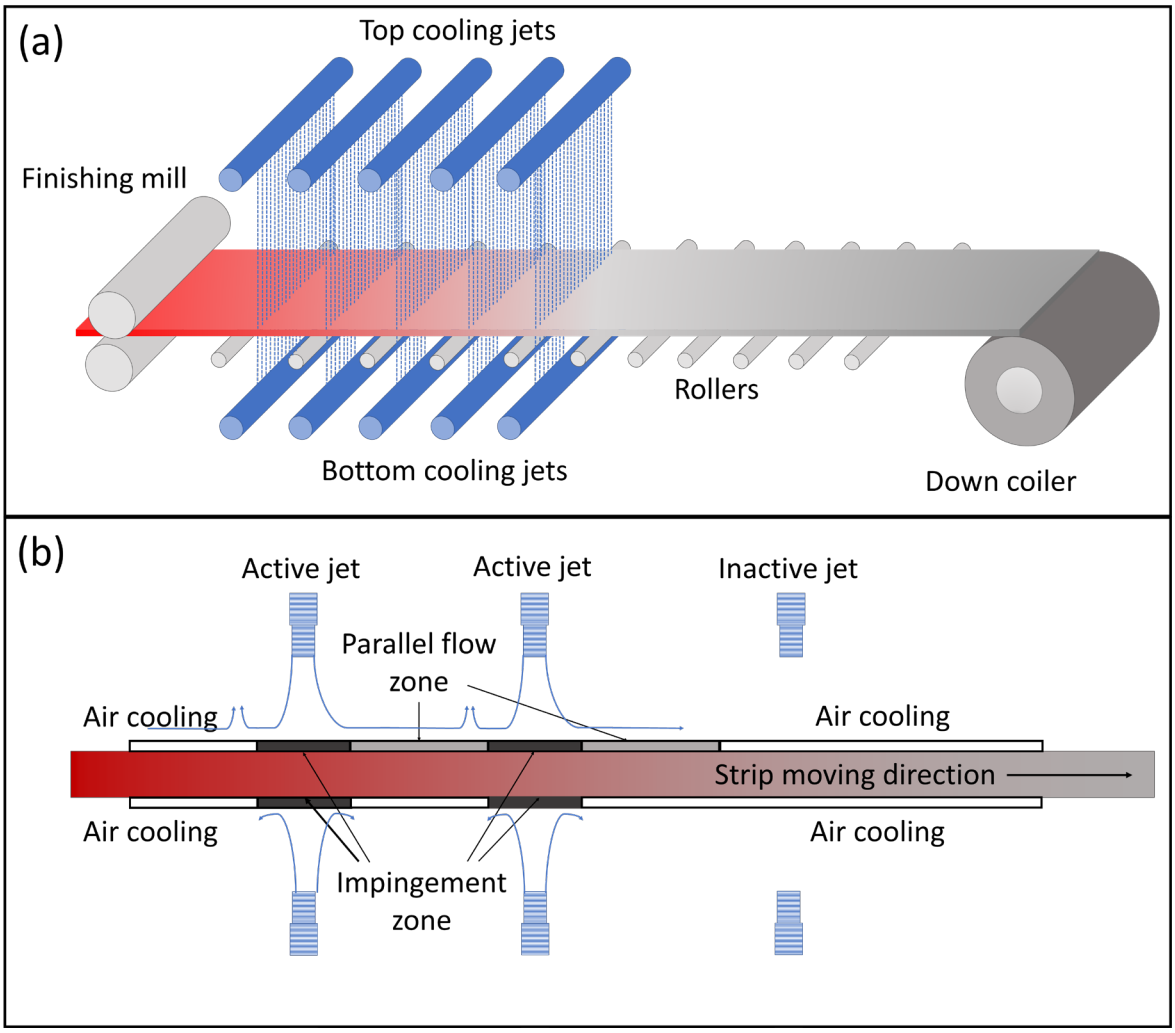

Figure 1.10. Schematic of (a) a runout table system with top and bottom cooling jets; (b) cooling zones on the runout table.

Figure 1.10(b) shows how the strip moves through different cooling zones on the runout table[48]. Right under active jets, there are the impingement zones for both top and bottom jets. On the top surface of strip, there are the parallel flow zones following the impingement zones in the moving direction, while they do not exist on the bottom surface due to gravity. Individual rows of jets may be active or inactive, as needed to tailor cooling for a particular steel grade and strip thickness. For regions under inactive jets, strips are in an air cooling regime, where the heat is extracted by forced air convection and radiation. The heat transfer coefficient of convection depends on the moving velocity of strips but is often neglected as it is quite small compared with radiation at typical steel process temperature[49]. The heat transfer modes for wetted zones are

dominated by flow boiling mechanisms because of the high surface temperature. A typical boiling curve for water at atmosphere is shown in Figure 1.11[50]. The boiling phenomena, including nucleate, transition, and film boiling, can occur when strips are water cooled on the runout table. In the parallel flow zone, film boiling with a stable vapor layer separating water from the strip surface is the dominant heat transfer mode. As for the impingement zone under water jet, although the surface temperature is still higher than temperature at the Leidenfrost point, the momentum of impinging and high degree of subcooling prevent the formation of a stable vapor layer and results in a single phase forced convection heat transfer mode[51]. It is worth noting that although there is heat transfer by conduction between strips and supporting rollers, it is often ignored as it only accounts for less than 0.5% heat extraction for an 8 mm thick strip, based on the study from Filipovic et al.[52].

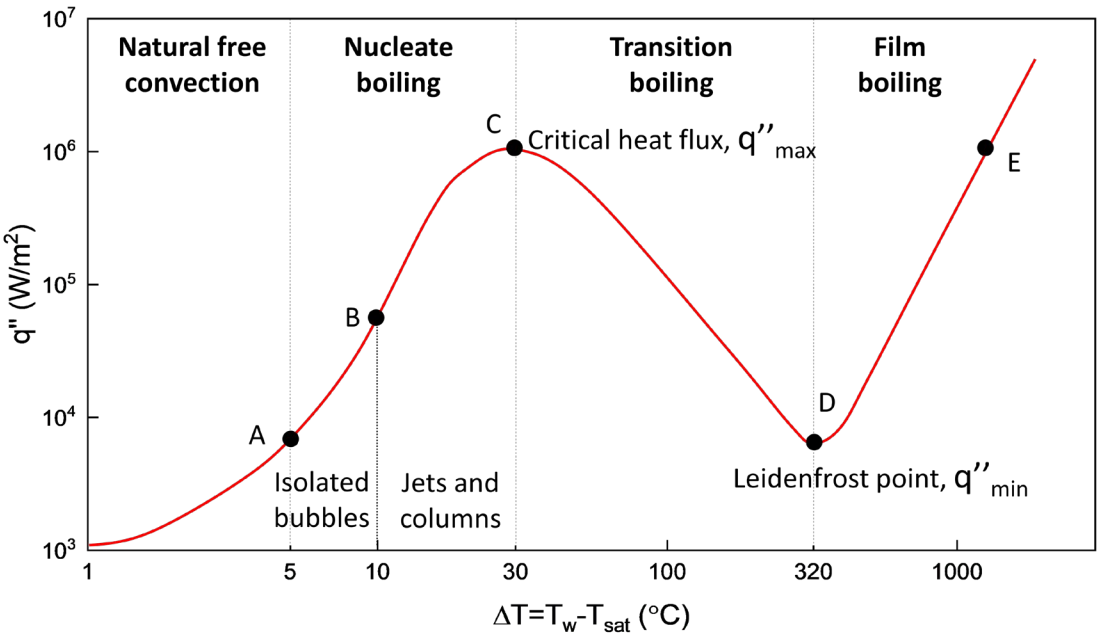

Figure 1.11. Typical boiling curve for saturated water at atmosphere: surface heat flux as a function of excess temperature (after [53]).

The heat transfer for runout table cooling has been studied both experimentally and numerically for decades. The heat transfer coefficient in water cooling zones depends on process parameters such as cooling water temperature, water flow rate, arrangement of water jets, and strip speed[54]. A universal heat transfer coefficient equation has not been established and used for

temperature calculation of runout table cooling. Measured cooling curves from hot rolling mills have been analyzed through statistical methods to develop empirical correlations between heat transfer coefficients and process parameters. Several empirical correlations from literature are summarized in Table 1.1. A universal heat transfer coefficient h_w is applied for the whole water cooling zone in a few cases. For other cases, different coefficients h_{imp} and h_{para} are used for impingement and parallel flow zones respectively.

Table 1.1. Summary of empirical correlations for heat transfer coefficients (in $Wm^{-2}°C^{-1}$) of runout table cooling.

Reference	Empirical correlation	Notes
Gadala and Xu[55]	$h_{imp} = 2.292\times10^{-4}T^{2.5}\cdot v^{-0.4}$ $h_{para} = 5.467\times10^{-5}T^{2.5}\cdot v^{-0.4}$	T is surface temperature in $°C$. v is strip velocity in m/s.
Ning et al.[56]	$h_{imp} = 150W^{0.6}$ $h_{para} = 0.4h_{imp}$	W is flow density in $Lmin^{-1}m^{-2}$.
Han et al.[57,58] Sun et al.[45] Karimi et al.[59]	$h_{imp,top} = 2186.7\alpha\cdot\left(\frac{T}{1000}\right)^{2.5}\cdot\left(\frac{v}{20}\right)^{-0.4}$ $h_{imp,bottom} = 0.35h_{imp,top}$ $h_{para} = \frac{157750}{(T-95)^{0.8}}\left(\frac{N_{nozzle}}{12}\right)^{0.3}$	α is edge masking factor. N_{nozzle} is the number of nozzles in a water bank.
Zheng et al.[60]	$h_{imp,top} = 2186.7\alpha\cdot\left(\frac{T}{1000}\right)^{1.62}\cdot\left(\frac{v}{20}\right)^{-0.4}\cdot\left(\frac{W}{W_0}\right)^{1.41}$	W_0 is reference flow density.
Guo[61]	$h_w = c_1\left(\frac{v}{v_0}\right)^{0.8}\left(\frac{T}{T_0}\right)^{1.4}\left(\frac{W}{W_0}\right)\left(\frac{t}{t_0}\right)^{c_2}$	t is strip thickness in m. v_0, t_0, T_0 are reference values for strip velocity, thickness and temperature. c_1, c_2 are curve fitted constant.

According to the cooling strategies on runout table, non-uniform cooling exists in both thickness and width direction of strips. As strips cool down, the temperature difference causes inhomogeneous phase transformation and thus results in non-flatness and residual stress[62].

Large residual stress is detrimental for strip quality especially when laser cutting or slitting is applied to strips[63]. Stress development during strip cooling stems from thermal and phase transformation strain. More, thermomechanical modeling with phase transformation has been used to combine the heat transfer and metallurgical phenomena to predict deformation and residual stress for runout table cooling. Yoshida[62] simulated the cooling of steel strips under different cooling conditions in transverse direction to study the effect of non-uniform cooling. A uniform transverse temperature distribution and higher coil temperature were proved to be beneficial for eliminating non-flatness defects such as edge wave. Taking advantage of the thin thickness of the strips, a 2D FEM model with a plane stress condition was established by Zhou et al.[64] to investigate residual stress distribution for a strip with non-uniform initial temperature across its width. The authors found that the temperature drop at the edge of strip caused compressive longitudinal stress at strip center and led to center wave defects. Control strategies have been proposed to help improve strip flatness after cooling. Cho et al.[65] investigated the influence of edge masking on edge wave by a 3D FEM model. Edge masking is proved to be effective on controlling transverse temperature profile and preventing temperature drop at edge by blocking the cooling water. With careful adjustment of the width of edge masking, residual stress and edge wave can be successfully reduced. Wang et al.[66] adopted a shape compensation control method of slight central wave rolling based on experimental measurements and simulation results. The strips were rolled with a slight center buckle after finishing mill to compensate the shape change during cooling. Strip flatness quality was improved for all strips with center buckles.

1.4 Research objectives

Boron addition causes post-casting problems like cracking defects in continuously-cast steel slabs. Although the effect of boron on microstructures, high temperature mechanical properties, and solidification has been studied for many years, its influence on stress development and crack formation still needs further investigation. Because boron changes the phase transformation behaviors of steel, stress development during cooling is also affected. Monitoring the interactions among conduction heat transfer, phase transformations, and stress development during the cooling process is difficult if not impossible. So, numerical modelling studies are helpful for a better understanding of the process and the role of boron in it. A 3D thermomechanical finite volume

model with coupled heat transfer, stress, and phase transformation calculations was developed to investigate the temperature history, phase evolution, and stress development during cooling with a focus on the effect of boron addition.

The development of the model presented in Chapter 2 couples three distinct sets of physical phenomena (thermal, metallurgical and mechanical) formulated from their governing equations. The numerical models are validated against analytical solutions and compared with results from literatures.

The model is used to simulate the cooling process of continuous cast steel slabs at different post-casting stages. The cooling process of a single slab in the slab yard after casting for both boron-containing and non-boron steels is investigated in Chapter 3, with a focus on the effect of boron on stress development and phase evolution during cooling. Multiple slabs can be stacked on top of each other as they cool in the slab yard to achieve a slower cooling rate and inhibit slab bowing. The effectiveness of slab stacking is investigated in Chapter 4. Boron addition also affects the water quenching process of steel strips on the runout table after hot rolling. The model is used to study the temperature history, phase transformation and stress development of strips with and without boron in Chapter 5. The influence of cooling strategies is studied for each steel grade to find an appropriate cooling conditions to improve strip quality after cooling.

2. MATHEMATICAL MODEL

This chapter is dedicated to developing a thermomechanical model coupled with phase transformation calculation to describe the cooling process of steel. In this model, a staggered approach is adopted, in which each physical field is calculated independently according to its governing equations, initial and boundary conditions and the couplings interactions between fields. Figure 2.1 illustrates the physical fields and interactions included in the current model for steel slab cooling.

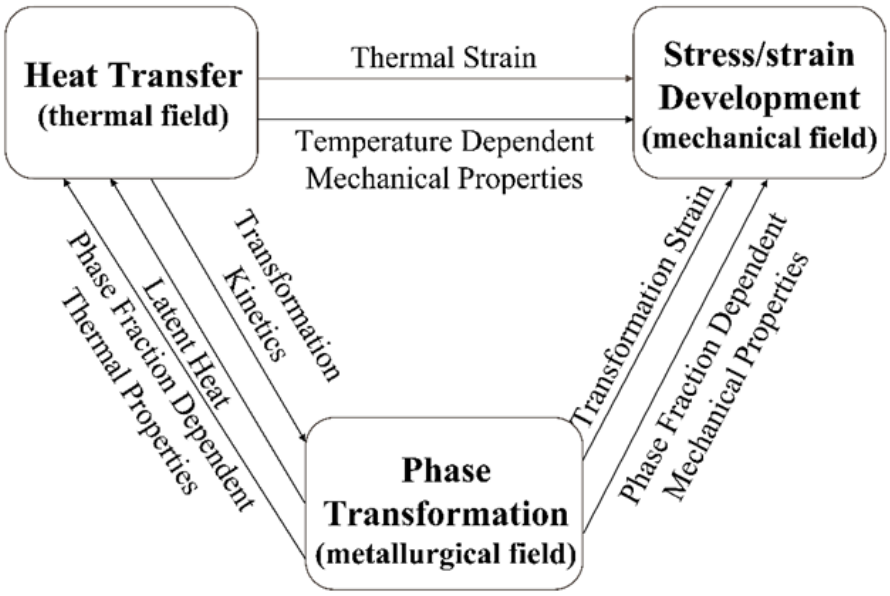

Figure 2.1. Physical fields and interactions included in the model.

2.1 Heat transfer model

During slab cooling process, heat transfer is the driving physical phenomenon for both phase transformation and stress development. All heat transfer modes, i.e., conduction, convection and radiation, could happen as cooling proceeds. The heat extraction occurs at the surface of slab via convection, radiation, and conduction in cases where contact between slabs is considered. The internal temperature field is determined by heat conduction due to thermal gradients.

2.1.1 Governing equations

The thermal field is calculated by the heat conduction equation that describes the transient heat flow and depletion within the material. Considering the latent heat from phase transformation, the equation can be expressed as

$$\frac{\partial(\rho c_p T)}{\partial t} = \nabla \cdot k\nabla \mathrm{T} + \dot{Q} \tag{2.1}$$

where $\boldsymbol{\rho}$, $\boldsymbol{c_p}$, $\boldsymbol{k}$, $\boldsymbol{T}$, and $\dot{\boldsymbol{Q}}$ are density, specific heat, thermal conductivity, temperature, and latent heat release rate, respectively. The heat generation term $\dot{\boldsymbol{Q}}$ due to the latent heat released by all phase transformations is given by

$$\dot{Q} = \sum \rho L_i \frac{dX_i}{dt} \tag{2.2}$$

where $\boldsymbol{X_i}$ is the volume fraction and $\boldsymbol{L_i}$ is the latent heat of phase transformation of phase/microconstituent $\boldsymbol{i}$. The possible phases/microconstituents are ferrite, pearlite, bainite, and martensite.

The heat generation term does not include the heat induced by plastic deformation in the current model as it is normally neglected for cooling process due to the small deformation. It was estimated to contribute to less than 1% for heat generation term[67].

The coupling of phase fraction dependent thermal properties for phase mixture $P(T)$ is defined by a linear rule of mixture expressed as

$$P(T) = \sum X_i P_i(T) \tag{2.3}$$

where $\boldsymbol{P_i}(\boldsymbol{T})$ is a thermal property of phase/microconstituent $\boldsymbol{i}$.

2.1.2 Boundary conditions

The thermal boundary conditions are set for heat transfer by convection and radiation at the slab surface,

$$q'' = \varepsilon\sigma\left(T_s^4 - T_\infty^4\right) + h\left(T_s - T_\infty\right) \tag{2.4}$$

where $\boldsymbol{\varepsilon}$ is the emissivity of the slab surface, $\boldsymbol{\sigma}$ the Stefan-Boltzmann constant, $\boldsymbol{T_s}$ the surface temperature, $\boldsymbol{T_\infty}$ the environmental temperature, and $\boldsymbol{h}$ the convective heat transfer coefficient.

For air cooling of slabs, the value for $\boldsymbol{h}$ is estimated by empirical correlations of external free convection flow[53] for a horizontal surface as

$$\overline{Nu}_L = 0.15 Ra_L^{1/3} \tag{2.5}$$

and for vertical surface as

$$\overline{Nu}_L = \left\{ 0.825 + \frac{0.387 Ra_L^{1/6}}{\left[1 + (0.492/Pr)^{9/16}\right]^{4/9}} \right\} \tag{2.6}$$

$$h = \frac{\overline{Nu}_L k}{L} \tag{2.7}$$

where $\overline{\boldsymbol{Nu}}_{\boldsymbol{L}}$ is the Nusselt number and $\boldsymbol{Ra}_{\boldsymbol{L}}$ is the Rayleigh number. The characteristic lengths for these quantities are $\boldsymbol{L = A_s/P}$ for the horizontal surface and $\boldsymbol{L = H}$ for the vertical where $\boldsymbol{A_s}$, $\boldsymbol{P}$, and $\boldsymbol{H}$ are horizontal surface area, perimeter, and slab thickness, respectively. All thermophysical properties, including the Prandtl number ($\boldsymbol{Pr}$) and thermal conductivity ($\boldsymbol{k}$), are for the air. For strips cooling on the runout table, the heat transfer coefficient $\boldsymbol{h}$ depends on the setup of the water cooling system and a series of process parameters and will be discussed in detail in Chapter 5.

2.2 Phase transformation model

Phase transformation is an important phenomenon during cooling of steel as it strongly affects the thermal and mechanical fields. The calculation of phase fraction depends on the temperature history and the phase transformation properties of steel. For most steels, the phase transformation from the initial austenite state at high temperature can be categorized in two types based on their mechanisms: the diffusion-controlled transformation to ferrite, pearlite, and bainite, and the displacive transformation to martensite.

2.2.1 Diffusion-controlled phase transformation

The diffusion-controlled phase transformations require the partitioning of carbon and other solutes via diffusion to accomplish the transformation from austenite to ferrite and cementite. Johnson and Mehl [68] developed the following equation for isothermal pearlite formation as a function of time:

$$X(t) = 1 - \exp(-\pi N G^3 t^4 / 3) \tag{2.8}$$

where $X(t)$ is the volume fraction of transformed pearlite at time t, N is the nucleation rate, and, G is the growth rate. This equation provides mathematical method to describe the isothermal transformation kinetics for phase nucleation and growth. Avrami[69] proposed an empirical equation with a simple form known as the Johnson-Mehl-Avrami-Kolmogorov (JMAK) kinetic equation:

$$X(t) = 1 - \exp(-b_i t^{n_i}) \tag{2.9}$$

where b_i and n_i are the temperature dependent kinetic parameters for phase/microconstituent i. The parameters can be calculated from the TTT diagrams. For diffusion-controlled transformation, the initial transformation rate is quite low, and the transformation does not start until a stable nuclei is developed. Therefore, an incubation time before transformation occurs should be considered for phase fraction calculation. A modified form of Eq. (2.9) becomes

$$X_i = X_i^{max}\{1 - exp[-b_i(t-\tau_0)^{n_i}]\} \tag{2.10}$$

where X_i^{max} represents the maximum possible transformed fraction of phase/microconstituent i and τ_0 is the incubation time[70].

Since the JMAK equation is used for describing the isothermal transformation behavior, it cannot be directly used for non-isothermal cooling process. Fernandes et al.[71] proposed a method to treat the non-isothermal process as multiple isothermal stages with a short time duration and then summed these stages up according to Scheil's additivity rule. This method is applied for calculating incubation time during cooling as illustrated in Figure 2.2. The incubation time under non-isothermal condition is calculated as follows,

$$S = \sum_{j=1}^{n} \frac{\Delta t^j}{\tau_0(T_j)} = 1 \tag{2.11}$$

where Δt^j is the time step at step j and $\tau_0(T_j)$ is the incubation time at step j and temperature T_j. When the Scheil's sum (S) equals to 1, the incubation time is considered as completed and the final incubation time can be calculated using $\tau_0 = \sum_{j=1}^{n} \Delta t^j$.

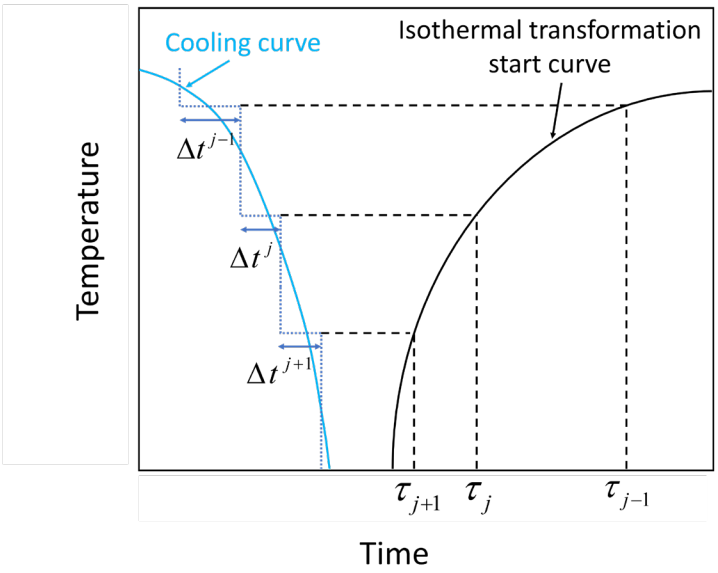

Figure 2.2. Calculation of non-isothermal incubation time from cooling curve and TTT diagram according to the Scheil's additivity rule.

Scheil's additivity rule is also applied for phase fraction calculation by JMAK equation. As illustrated in Figure 2.3, a fictitious time τ^j at time step j is calculated based on the transformed fraction at previous time step $j-1$ as follows,

$$\tau^j = \left[-\frac{ln(1-X_i^{j-1})}{b_i^j} \right]^{1/n_i^j} \tag{2.12}$$

where X_i^{j-1} represents the fraction of phase/microconstituent i at previous time step $j-1$, b_i^j and n_i^j are the kinetic parameters for phase i at step j. The phase fraction X_i^j at current step j is obtained using τ_j:

$$X_i^j = X_i^{max}\{1-exp[-b_i^j(\tau^j+\Delta t^j)^{n_i^j}]\} \tag{2.13}$$

where Δt^j is the time step size at step j. For pearlite and bainite transformation, X_i^{max} simply represents the amount of austenite at the beginning of transformation.

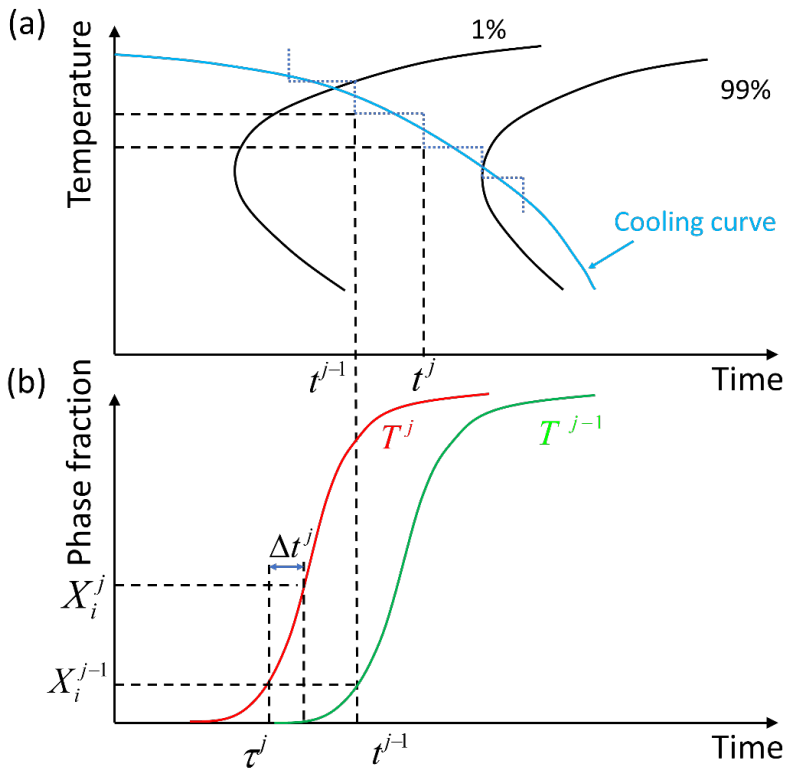

Figure 2.3. Calculation of phase fraction for non-isothermal cooling according to JMAK equation and Scheil's additivity rule.

As for ferrite transformation, X_i^{max} changes with decreasing temperature according to the phase diagram of Fe-C. The ferrite phase transformation during cooling process of a hypoeutectoid steel is shown in Figure 2.4 as an equilibrium phase diagram of Fe-C with extrapolated phase boundaries. When temperature drops between A_3 and A_1 temperatures, proeutectoid ferrite with low carbon solubility forms and the austenite is enriched with carbon. The maximum fraction of ferrite that could form isothermally is calculated by lever rule as $X_F^{max} = \frac{a_1 b_1}{e_1 b_1}$. For non-isothermal cooling, when steel is rapidly cooled to point a_2 which is below A_1 temperature but still above line CF, ferrite forms at the austenite grain boundary first without the formation of cementite. If the steel is held isothermally to keep the ferrite formation, the maximum ferrite fraction could reach $X_F^{max} = \frac{a_2 b_2}{e_2 b_2}$. However, the carbon concentration in austenite keeps increasing with ferrite growth. When it reaches point b, pearlite formation occurs before the maximum ferrite fraction is reached. Therefore, there is a limit for fraction of proeutectoid ferrite formation before pearlite

transformation at a certain temperature and it can be calculated as $X_F^{limit} = \frac{a_2 b}{e_2 b}$. The phase fraction of proeutectoid ferrite is calculated with a modified Eq.(2.13):

$$X_F^j = \begin{cases} X_F^{max}\{1 - exp[-b_F^j(\tau^j + \Delta t^j)^{n_F^j}]\} & \text{if } X_F^j \le X_F^{\text{limit}} \\ X_F^{\text{limit}} & \text{if } X_F^j > X_F^{\text{limit}} \end{cases} \tag{2.14}$$

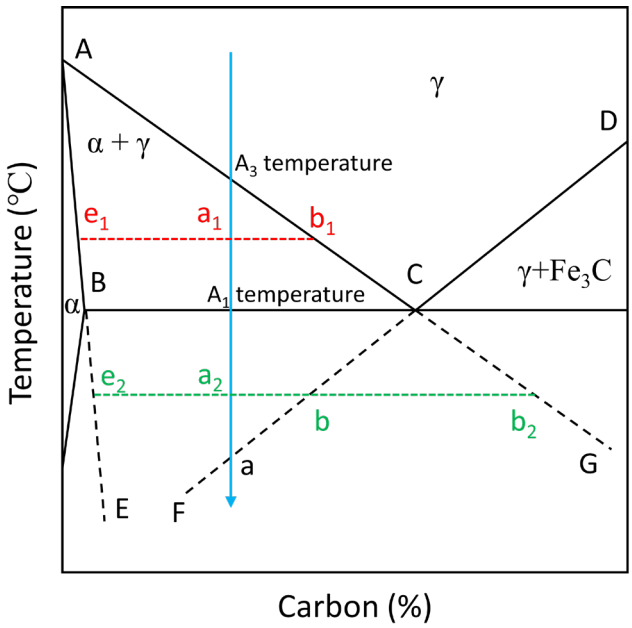

Figure 2.4. Eutectoid equilibrium diagram of Fe-C with extrapolated phase boundaries for ferrite and cementite.

The calculation of proeutectoid ferrite and pearlite can be carried out with different approaches. Hawbolt et al.[70] decided to treat proeutectoid ferrite and pearlite formation as two independent transformations and used two JMAK equations for phase fraction calculations. A schematic of the isothermal transformation curve for the two-equation approach is shown in Figure 2.5(a). However, according to the analysis of the maximum fraction of proeutectoid ferrite above, the pearlite formation is closely related to the amount of proeutectoid ferrite precipitation and when pearlite transformation occurs, the proeutectoid ferrite formation is still in progress. Therefore, Pan et al.[72] proposed an approach to use one combined JMAK equation to calculate the total amount of proeutectoid ferrite and pearlite as illustrated in Figure 2.5(b). The ferrite fraction is calculated using X_F^{max} instead of X_F^{limit}. But the growth rate of pearlite could be overestimated at the beginning of transformation according to this approach. Therefore, a modified

two-equation approach is adopted in the current model by combining the two approaches. The equations used in each approach is summarized in Table 2.1.

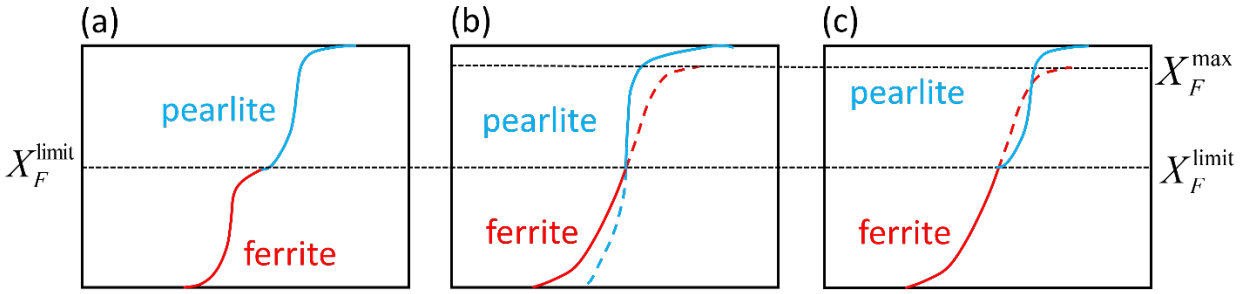

Figure 2.5. Schematics of isothermal transformation of proeutectoid ferrite and pearlite: (a) two-equation approach; (b) one-equation approach; (c) modified two-equation approach.

Table 2.1. Summarized equations used for proeutectoid ferrite and pearlite calculation.

Calculation approach	**Equation**	
Two-equation	$X_F = X_F^{limit}\{1-exp[-b_F(t-\tau_0)^{n_F}]\}$	(2.15)
	$X_P = (1-X_F^{limit})\{1-exp[-b_P(t-\tau_0)^{n_P}]\}$	(2.16)
One-equation	if $X_F + X_P \le X_F^{limit}$, then $\begin{cases} X_F = X_F^{max}\{1-exp[-b_F(t-\tau_0)^{n_F}]\} \\ X_P = 0 \end{cases}$	(2.17)
	if $X_F + X_P > X_F^{limit}$, then $\begin{cases} X_F = X_F^{limit} \\ X_P = \{1-exp[-b_P(t-\tau_0)^{n_P}]\} - X_F^{limit} \end{cases}$	(2.18)
Modified two-equation	if $X_F + X_P \le X_F^{limit}$, then $\begin{cases} X_F = X_F^{max}\{1-exp[-b_F(t-\tau_0)^{n_F}]\} \\ X_P = 0 \end{cases}$	(2.19)
	if $X_F + X_P > X_F^{limit}$, then $\begin{cases} X_F = X_F^{limit} \\ X_P = (1-X_F^{limit})\{1-exp[-b_P(t-\tau_0)^{n_P}]\} \end{cases}$	(2.20)

To test the modified approach applied in the current model, the TTT diagram of 3310 steel shown in Figure 2.6(a) was used as an input for phase transformation kinetic parameters. The model calculated phase fractions during continuous cooling process at different cooling rates to produce a continuous-cooling-transformation (CCT) diagram of 3310 steel. As demonstrated in Figure 2.6(b), the CCT diagram reconstructed from simulation results of continuous cooling cases shows a good match compared to the CCT data from JMatPro[73]. The results demonstrated the feasibility of the current model utilizing Scheil's additivity rule and the modified JMAK equations.

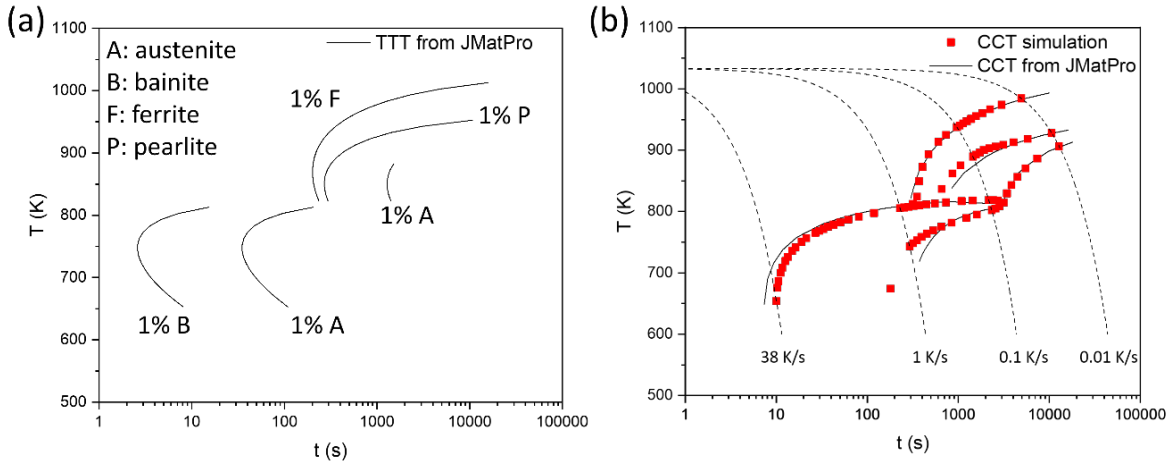

Figure 2.6. (a) TTT diagram of 3310 steel; (2) comparison of CCT diagram of 3310 steel with calculated CCT diagram based on simulation results[73].

2.2.2 Displacive phase transformation

The displacive phase transformation from austenite to martensite is time independent as no diffusion is needed. Since it is referred as athermal transformation, it occurs without thermal activation. Unlike diffusion-controlled transformations, it is not a function of time. The formation of martensite is accomplished as soon as a temperature below the T_{M_S} temperature is reached. Therefore, the JMAK equation is not suitable for describing the kinetics of martensitic transformation. The growth of martensite is modeled by the Koistinen-Marburger relationship[74] as a function of temperature:

$$X_m = X_\gamma \{1 - exp[-\Omega(T_{M_s} - T)]\} \tag{2.21}$$

where X_m is the fraction of martensite, X_γ is the fraction of austenite at the start of martensite formation, T_{M_S} is the martensite starting temperature and Ω is a constant representing the transformation rate. For low carbon steels, the value of Ω is approximately 0.011.

2.3 Mechanical field analysis

The mechanical field analysis describes the mechanical response of materials in the form of stress and strain. During steel slab cooling process, the thermal gradient causes thermal strain, and the dilatation of phase transformation causes transformation strain. The combination of both strain

results in stress development which could lead to problems such as distortion and cracking. When the stress at certain position of slab exceeds the local yield strength, plastic deformation occurs and causes plastic strain. After cooling process, the nonuniform phase distribution and plastic deformation results in a residual stress state.

2.3.1 Linear elastic model

For mechanical field analysis, the governing equation used for calculation is given by the conservation of linear momentum in its differential form as follows[75],

$$\frac{\partial^2(\rho \boldsymbol{D})}{\partial t^2} = \nabla \bullet \boldsymbol{\sigma} + \rho \boldsymbol{f} \tag{2.22}$$

where $\boldsymbol{D}$ is the displacement vector, $\boldsymbol{\sigma}$ is the Cauchy stress tensor, and $\boldsymbol{f}$ is the body force per unit mass. In case of small strain, the strain tensor $\boldsymbol{\varepsilon}$ is defined in terms of displacement $\boldsymbol{D}$ as:

$$\boldsymbol{\varepsilon} = \frac{1}{2}[\nabla \boldsymbol{D} + (\nabla \boldsymbol{D})^T] \tag{2.23}$$

In order to solve the momentum balance equation, a constitutive relation is needed as it relates the stress and strain of material. For a linear elastic material, the simplest model considering the isotropic Hook's law is adopted:

$$\boldsymbol{\sigma} = 2\mu\boldsymbol{\varepsilon} + \lambda tr(\boldsymbol{\varepsilon})\mathbf{I} \tag{2.24}$$

where μ and λ are the Lamé constants, and $\mathbf{I}$ is the identity tensor. The Lamé constants are material properties related to mechanical properties including Young's modulus of elasticity E and Poisson's ratio ν as

$$\mu = \frac{E}{2(1+\nu)} \tag{2.25}$$

and

$$\lambda = \begin{cases} \dfrac{\nu E}{(1+\nu)(1-\nu)} & \text{(plane stress)} \\ \dfrac{\nu E}{(1+\nu)(1-2\nu)} & \text{(plane strain and 3D)} \end{cases} \tag{2.26}$$

Combining equations above, the governing equation of momentum balance is rearranged as follows with displacement $\boldsymbol{D}$ as the variable:

$$\frac{\partial^2(\rho \boldsymbol{D})}{\partial t^2} = \nabla \cdot [\mu \nabla \boldsymbol{D} + \mu (\nabla \boldsymbol{D})^T + \lambda \mathbf{I} tr(\nabla \boldsymbol{D})] + \rho \boldsymbol{f} \tag{2.27}$$

2.3.2 Elastoplastic model

Plastic deformation plays an important role in the residual stress development during cooling. Since the plastic behavior depends on the deformation history of material, the stress-strain relations in plastic deformed regions cannot be calculated based on the total accumulated strain. Therefore, the governing equation Eq. (2.22) should be rewritten in the incremental form for elastoplastic model:

$$\frac{\partial^2(\rho d\boldsymbol{D})}{\partial t^2} = \nabla \bullet d\boldsymbol{\sigma} + \rho d\boldsymbol{f} \tag{2.28}$$

where $d\boldsymbol{D}$, $d\boldsymbol{\sigma}$, and $d\boldsymbol{f}$ are the increment in displacement, stress, and body force, respectively. Elastoplastic material is assumed to have linear elastic behavior in the elastic regime so that Hook's law is still applied to the elastic strain as follow,

$$d\boldsymbol{\sigma} = 2\mu d\boldsymbol{\varepsilon}^e + \lambda tr(d\boldsymbol{\varepsilon}^e)\mathbf{I} \tag{2.29}$$

The total strain increment $d\boldsymbol{\varepsilon}$ is given by the displacement increment as,

$$d\boldsymbol{\varepsilon} = \frac{1}{2}[\nabla d\boldsymbol{D} + (\nabla d\boldsymbol{D})^T] \tag{2.30}$$

It can be decomposed to individual strain from elastic and plastic deformation as,

$$d\boldsymbol{\varepsilon} = d\boldsymbol{\varepsilon}^e + d\boldsymbol{\varepsilon}^p \tag{2.31}$$

where $d\boldsymbol{\varepsilon}^p$ represents the plastic strain increment. The plastic behavior of a material depends on its yield criterion, flow rule and hardening rule. The yield criterion is used to determine when the plastic deformation occurs and the flow rule to determine the amount of plastic deformation. Von Mises yield criterion, associated Prandtl-Reuss flow rule and isotropic hardening rule are adopted in the model to describe the plastic behavior of steels. A yield function f is defined by Eq. (2.32) and the plastic strain increment $d\boldsymbol{\varepsilon}^p$ is expressed as shown in Eq. (2.33). A linear isotropic hardening rule with a constant hardening modulus H is applied to describe the strain hardening effect using Eq. (2.34).

$$f\left(\boldsymbol{\sigma}, \varepsilon_p^{eq}\right) = \sqrt{\frac{3}{2}\boldsymbol{\sigma}^{dev} : \boldsymbol{\sigma}^{dev}} - \sigma_f(\varepsilon_p^{eq}) \tag{2.32}$$

$$d\boldsymbol{\varepsilon}^{p} = \dot{\gamma}\sqrt{\frac{3}{2}}\frac{\boldsymbol{\sigma}^{dev}}{\sqrt{\boldsymbol{\sigma}^{dev} : \boldsymbol{\sigma}^{dev}}} \tag{2.33}$$

$$\sigma_f\left(\varepsilon_p^{eq}\right) = \sigma_Y + H\varepsilon_p^{eq} \tag{2.34}$$

In these equations, $\boldsymbol{\sigma}^{dev}$, σ_f, ε_p^{eq}, $\dot{\gamma}$ and σ_Y represents the deviatoric stress, flow stress, effective plastic strain, plastic multiplier, and yield strength, respectively.

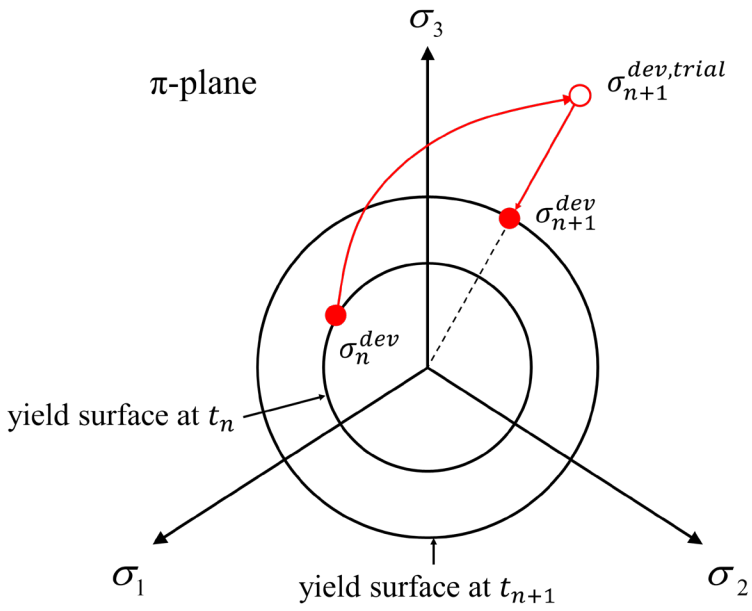

Figure 2.7. Schematic of the radial return method for the von Mises model showing stress state at the deviatoric plane.

For the current model, the radial return method[76] is used to determine the plastic strain increment $d\boldsymbol{\varepsilon}^{p}$ and calculate the corresponding stress increment $d\sigma$. The schematic of the radial return method for model using von Mises yield criterion is illustrated in Figure 2.7. A trial stress for step $n+1$ is calculated assuming all the strain increment $d\boldsymbol{\varepsilon}$ is entirely elastic. If the trial stress state is on the outside of yield surface, the stress will be projected on to the closest point of yield surface. When isotropic hardening is considered, the yield surface expands as the effective plastic strain increases. For general cases where hardening curves show non-linear behavior, iterative solution using the Newton-Raphson method is applied for calculation of the updated stress and strain. For materials with linear hardening curves, the effective plastic strain increment is directly calculated as

$$\Delta\gamma = \frac{\sigma_{n+1}^{eq,trial} - \sigma_Y - H\varepsilon_p^{eq}}{3\mu + H} \tag{2.35}$$

The procedures using radial return method for von Mises plasticity model with linear isotropic hardening rule is summarized in Table 2.2.

Table 2.2. Solution algorithm for elastoplastic model using radial return method.

Initial input: $\boldsymbol{\sigma}_n$ (previous stress at step n), ε_p^{eq} (previous effective plastic strain), $d\boldsymbol{\varepsilon}$ (total strain increment)
1) Assuming elastic response and calculate the trial stress state
$d\boldsymbol{\varepsilon}^e = d\boldsymbol{\varepsilon}$ (2.36)
$\boldsymbol{\sigma}_{n+1}^{trial} = \boldsymbol{\sigma}_n + [2\mu d\boldsymbol{\varepsilon}^e + \lambda tr(d\boldsymbol{\varepsilon}^e)\mathbf{I}]$ (2.37)
2) Check trial stress state for plastic deformation
If $\boldsymbol{\sigma}_{n+1}^{eq,trial} \le \sigma_Y + H\varepsilon_p^{eq}$, elastic deformation and exit with $\boldsymbol{\sigma}_{n+1} = \boldsymbol{\sigma}_{n+1}^{trial}$ If $\boldsymbol{\sigma}_{n+1}^{eq,trial} > \sigma_Y + H\varepsilon_p^{eq}$, plastic deformation
3) Calculate effective plastic strain increment and update stress state
$\Delta\gamma = \frac{\sigma_{n+1}^{eq,trial} - \sigma_Y - H\varepsilon_p^{eq}}{3\mu + H}$ (2.35)
$\boldsymbol{\sigma}_{n+1} = \frac{1}{3} tr(\boldsymbol{\sigma}_{n+1}^{trial})\mathbf{I} + \boldsymbol{\sigma}_{n+1}^{dev,trial} \frac{\sigma_Y + H(\varepsilon_p^{eq} + \Delta\gamma)}{\boldsymbol{\sigma}_{n+1}^{eq,trial}}$ (2.38)
4) Calculate plastic strain increment and update effective plastic strain
$d\boldsymbol{\varepsilon}^p = \Delta\gamma \sqrt{\frac{3}{2}} \frac{\boldsymbol{\sigma}_{n+1}^{dev}}{\sqrt{\boldsymbol{\sigma}_{n+1}^{dev} : \boldsymbol{\sigma}_{n+1}^{dev}}}$ (2.39)
$\varepsilon_p^{eq} = \varepsilon_p^{eq} + \Delta\gamma$ (2.40)

2.3.3 Formulation of thermal strain and transformation strain

To couple the strain from thermal field and metallurgical field to the model for thermomechanical analysis with phase transformation, the total strain increment $d\boldsymbol{\varepsilon}$ can be decomposed as follows,

$$d\boldsymbol{\varepsilon} = d\boldsymbol{\varepsilon}^{e} + d\boldsymbol{\varepsilon}^{p} + d\boldsymbol{\varepsilon}^{th} + d\boldsymbol{\varepsilon}^{ph} \tag{2.41}$$

where $d\boldsymbol{\varepsilon}^{th}$ and $d\boldsymbol{\varepsilon}^{ph}$ represent thermal and phase transformation strain, respectively.

The thermal strain increment is caused by the volumetric thermal expansion and defined as

$$d\boldsymbol{\varepsilon}^{th} = \alpha dT\mathbf{I} \tag{2.42}$$

where α is the thermal expansion coefficient and dT is the temperature change. The phase transformation strain increment due to structural dilatation from austenite decomposition can be represented by

$$d\boldsymbol{\varepsilon}^{ph} = \sum_{i=1}^{n} \frac{1}{3} \Delta_i dX_i \mathbf{I} \tag{2.43}$$

where Δ_i is the structural dilatation due to austenite decomposition and dX_i is the change in fraction of phase/microconstituent i. The mechanical field is also affected by the temperature and phase fraction dependent mechanical properties. The mechanical properties including Young's modulus, Poisson's ratio, thermal expansion coefficient, yield strength are updated based on temperature field and phase distribution for each time step by applying a linear rule of mixture.

2.4 Numerical implementation

Numerical methods are necessary for solving the equations in the model developed in the previous sections. The finite volume method (FVM) is used to solve the governing differential equations for both heat transfer model and mechanical analysis. In the field of structural analysis for solid mechanics, finite element method (FEM) has been the dominant method for decades. Although the FV method is mainly used for computational fluid dynamics (CFD), it has been successfully applied to solve solid mechanics problems. The earliest work from Demirdžić et al.[77] on linear elasticity provides a fundamental knowledge of FVM for stress analysis. Following work has extended the use of FVM in a large variety of solid stress analysis and multiphysics phenomena including elastoplasticity[78,79], fracture mechanics[80,81], contact mechanics[82,83], and fluid-solid interactions[84,85]. A detailed review of FVM on solid mechanics is provided by Cardiff

and Demirdžić[86]. The numerical implementation of the model based on FVM is done by utilizing OpenFOAM which is an open-source CFD software platform. The implementation consists of the finite volume discretization and solution algorithm for the algebraic linearized equations.

2.4.1 Finite volume discretization

The implicit cell-centered finite volume method is used for discretizing the governing equations developed in the mathematical models[75,77]. The discretization procedure includes discretization of time interval, space, and governing equations from mathematical model. For transient simulations, the total simulation time is split into multiple short time increments, Δt, known as time step size. For steady state simulation, time step can be set as infinity. As for discretization of space, the spatial domain is divided into a finite number of convex polyhedral control volumes (CV). The CVs do not overlap and entirely fill the compotation domain. A typical hexahedral CV is shown in Figure 2.8 with point P located at the cell center and a cell volume as Ω_P. Point N is the cell center of a neighboring control volume. The two CVs share face *f* and vector $\boldsymbol{d}_f$ joining P to N is also the normal vector for hexahedral CV. For FV spatial discretization, cells with different shapes can be mixed.

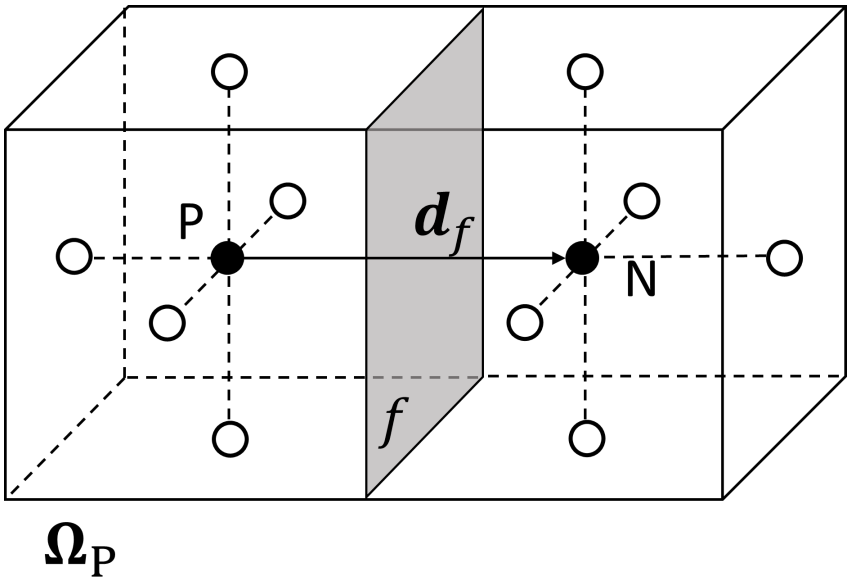

Figure 2.8. A typical hexahedral control volume with P as the cell center. It shares face *f* with a neighboring cell with N as its cell center.

For the simplest linear elastic model assuming a uniform density field, the momentum balance equation (2.27) is written in the integral form as follows:

$$\underbrace{\int_{\Omega_P} \rho \frac{\partial^2 \boldsymbol{D}}{\partial t^2} d\Omega}_{\text{Inertia}} = \underbrace{\oint_{\Gamma} \boldsymbol{n} \cdot [\mu \nabla \boldsymbol{D} + \mu (\nabla \boldsymbol{D})^T + \lambda tr(\nabla \boldsymbol{D}) \mathbf{I}] d\Gamma}_{\text{Surface forces}} + \underbrace{\int_{\Omega_P} \rho \boldsymbol{f} \, d\Omega}_{\text{Body forces}} \tag{2.44}$$

where $\boldsymbol{n}$ is the surface unit normal vector. The three terms in Eq. (2.44) need to be discretized based on FV method.

For the inertia term, it can be approximated assuming a linear variation of displacement $\boldsymbol{D}$ over the CV. Therefore, the variation of $\boldsymbol{D}$ is expressed as

$$\boldsymbol{D}(\boldsymbol{x}) = \boldsymbol{D}_P + (\boldsymbol{x} - \boldsymbol{x}_P) \cdot (\nabla \boldsymbol{D})_P \tag{2.45}$$

$\boldsymbol{D}(\boldsymbol{x})$ represents displacement at any point in the CV and it can be calculated based on the cell center displacement $\boldsymbol{D}_P$ and the constant gradient of displacement $(\nabla \boldsymbol{D})_P$. The volume integral of Ω_P is calculated using Eq.(2.45) and the mid-point rule:

$$\int_{\Omega_P} \rho \frac{\partial^2 \boldsymbol{D}}{\partial t^2} d\Omega \approx (\frac{\partial^2 \boldsymbol{D}}{\partial t^2})_P \cdot \Omega_P \tag{2.46}$$

The time derivative of displacement $\boldsymbol{D}$ at cell center P and at time m is calculated using a first-order backward Euler method as

$$(\frac{\partial^2 \boldsymbol{D}}{\partial t^2})_P \approx \frac{\boldsymbol{D}_P^{[m]} - 2\boldsymbol{D}_P^{[m-1]} + \boldsymbol{D}_P^{[m-2]}}{\Delta t^2} \tag{2.47}$$

where $\boldsymbol{D}_P^{[m]}$, $\boldsymbol{D}_P^{[m-1]}$, and $\boldsymbol{D}_P^{[m-2]}$ represent the displacement at P for the current time m, and two old time $m-1$ and $m-2$, respectively.

After spatial and temporal discretization, the final form of the inertia term is given by:

$$\int_{\Omega_P} \rho \frac{\partial^2 \boldsymbol{D}}{\partial t^2} d\Omega \approx \rho (\frac{\boldsymbol{D}_P^{[m]} - 2\boldsymbol{D}_P^{[m-1]} + \boldsymbol{D}_P^{[m-2]}}{\Delta t^2}) \Omega_P \tag{2.48}$$

The same method of spatial discretization is also applied for the body force term in Eq.(2.44) and the discretized body force term is expressed as:

$$\int_{\Omega_P} \rho \boldsymbol{f} \, d\Omega \approx \rho \boldsymbol{f}_P \cdot \Omega_P \tag{2.49}$$

Before the discretization of the surface force term, the integral over the entire closed surface Γ is split into a sum of individual integrals for each face of the CV as F is the number of faces for the CV:

$$\oint_{\Gamma} \boldsymbol{n} \cdot [\mu \nabla \boldsymbol{D} + \mu (\nabla \boldsymbol{D})^T + \lambda tr(\nabla \boldsymbol{D}) \mathbf{I}] d\Gamma = \sum_{f=1}^{F} \int_{\Gamma_f} \boldsymbol{n} \cdot [\mu \nabla \boldsymbol{D} + \mu (\nabla \boldsymbol{D})^T + \lambda tr(\nabla \boldsymbol{D}) \mathbf{I}] d\Gamma_f \quad (2.50)$$

According to the force balance of the surface forces, this term is discretized using the assumption of the variation of $\boldsymbol{D}$ from Eq. (2.45) as follows:

$$\begin{aligned} &\sum_{f=1}^{F} \int_{\Gamma_f} \boldsymbol{n} \cdot [\mu \nabla \boldsymbol{D} + \mu (\nabla \boldsymbol{D})^T + \lambda tr(\nabla \boldsymbol{D}) \mathbf{I}] d\Gamma_f \approx \\ &\qquad \sum_{f=1}^{F} \boldsymbol{n}_f \cdot [\mu (\nabla \boldsymbol{D})_f + \mu (\nabla \boldsymbol{D})_f^T + \lambda tr(\nabla \boldsymbol{D})_f \mathbf{I}] \left| \Gamma_f \right| \end{aligned} \quad (2.51)$$

where $(\nabla \boldsymbol{D})_f$ represents the gradient of $\boldsymbol{D}$ at face center on face f. The determination of $(\nabla \boldsymbol{D})_f$ at face center depends on the displacement gradient at the two adjacent cell centers. $(\nabla \boldsymbol{D})_f$ is approximated using:

$$(\nabla \boldsymbol{D})_f \approx \gamma_f (\nabla \boldsymbol{D})_P + (1 - \gamma_f)(\nabla \boldsymbol{D})_{N_f} \quad (2.52)$$

where $(\nabla \boldsymbol{D})_{N_f}$ is the gradient of displacement at the neighbor cell center for face f. The parameter γ_f is related to the distance from cell center to face center and is calculated by:

$$\gamma_f = \frac{\left| \boldsymbol{x}_{N_f} - \boldsymbol{x}_f \right|}{\left| (\boldsymbol{x}_f - \boldsymbol{x}_P) + (\boldsymbol{x}_{N_f} - \boldsymbol{x}_{N_f}) \right|} \quad (2.53)$$

With all three terms in the momentum balance equation discretized, the discretized form of the governing equation is given as:

$$\rho \left(\frac{\boldsymbol{D}_P^{[m]} - 2\boldsymbol{D}_P^{[m-1]} + \boldsymbol{D}_P^{[m-2]}}{\Delta t^2} \right) \Omega_P = \sum_{f=1}^{F} \boldsymbol{n}_f \cdot [\mu (\nabla \boldsymbol{D})_f + \mu (\nabla \boldsymbol{D})_f^T + \lambda tr(\nabla \boldsymbol{D})_f \mathbf{I}] \left| \Gamma_f \right| + \rho \boldsymbol{f}_P \cdot \Omega_P \quad (2.54)$$

2.4.2 Solution algorithm for linear algebraic systems

The discretization rearrangement of the governing equations, a linear algebraic equation is created for each CV in the form of the following equation.

$$a_P \boldsymbol{D}_P + \sum_N a_N \boldsymbol{D}_N = b_P \tag{2.55}$$

The value of $\boldsymbol{D}_P$ for a certain CV cannot be calculated directly from the discretized equation as it depends on the values $\boldsymbol{D}$ from neighboring CVs. Therefore, the linear algebraic equation for each CV in the computational domain is combined to create a system of equations. The matrix form of the system is written as

$$[A][x] = [b] \tag{2.56}$$

For a domain with M cells, $[A]$ is a $M \times M$ sparse matrix with a_P as the diagonal coefficients and a_N as off-diagonal coefficients. $[x]$ is the vector of $\boldsymbol{D}$ for all CVs and $[b]$ is the source vector. The linear system is normally solved by iterative methods. For the current model, the equations are solved by a segregated solution procedure where each component of displacement $\boldsymbol{D}$ is solved separately. Outer iterations are necessary to account for the inter-component coupling between equations. The GAMG (generalized geometric-algebraic multi-grid) solver is used for displacement calculation. The basic principle of GAMG solver is that it starts with a coarse mesh for a quick solution. The quick solution is then used as an initial guess to solve for a more accurate solution for a finer mesh.

2.4.3 Numerical test cases

The thermomechanical model with elastoplasticity and phase transformation is developed and implemented on the OpenFOAM platform. Numerical test cases are performed to verify the successful implementation of the model. Test case results are compared with analytical solution or data from literature.

Test case – internally pressurized spherical shell

The plastic deformation simulation based on the radial return method is developed in the model for plastic strain calculation and residual stress prediction. The plasticity model is verified against an axisymmetric analysis of an internally pressurized spherical shell. The geometry of test case is shown in Figure 2.9(a) as the outer and inner radius are 200 mm and 100 mm respectively. Due to symmetry condition, 1/8 of the shell has been meshed with 67500 hexahedral cells shown in Figure 2.9(b).

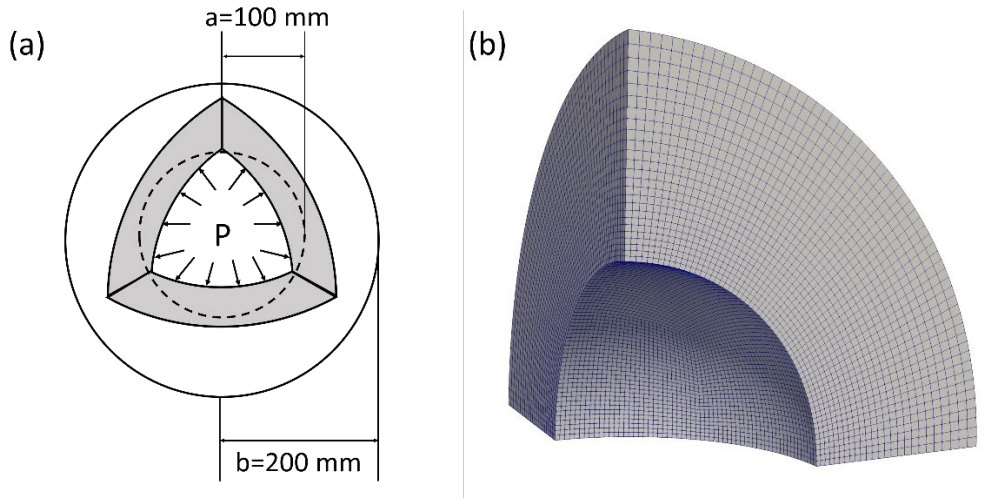

Figure 2.9. Test case geometry and the mesh for simulation. A gradient mesh is adopted as the inner surface show finer mesh.

Von Mises yield criterion and perfect plasticity are adopted with constant mechanical properties ($E = 210$ GPa , $\nu = 0.3$, $\sigma_Y = 0.24$ GPa). The inner surface is under a gradually increasing internal pressure and the outer surface is set as free surface. As the internal pressure increases, plastic deformation starts to occur at the inner surface. The plastic front keeps moving outwards with increasing pressure. For a perfect plasticity case without considering hardening effect, Once the plastic front reaches the outer surface, the simulation collapse as the shell can expand indefinitely under perfect plasticity assumption. The stress distributions along radius direction at two different load conditions are plotted in Figure 2.10 for both (a) hoop stress and (b) radial stress. The hoop stress distribution shows a peak stress right at the plastic front as it moves outwards. The simulation results are virtually identical to the analytical solution from Hill[86,87] indicating a good implementation of the plasticity model.

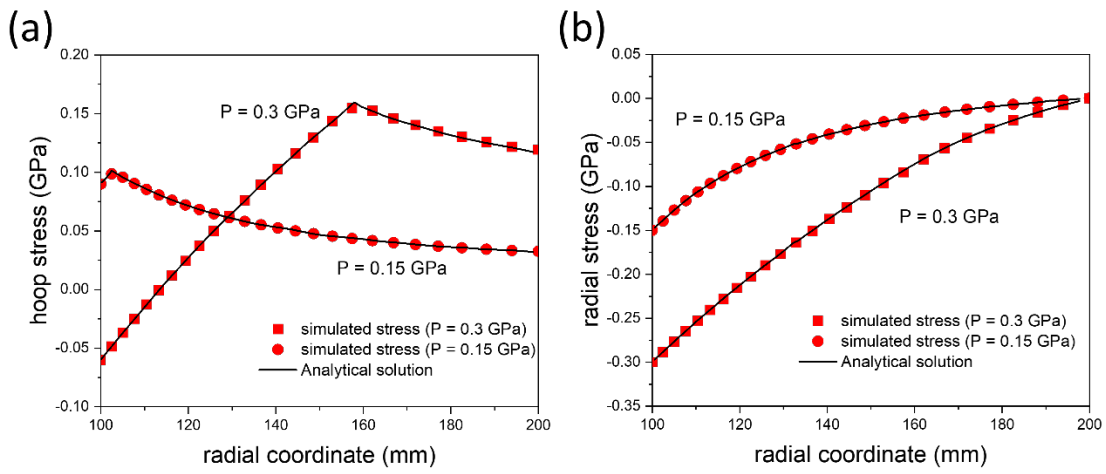

Figure 2.10. (a) Hoop and (b) radial stress distribution along radial direction of the internally pressurized spherical shell under different applied pressure. The simulation results show close agreement with analytical solution.

With plastic deformation calculated under loading, the residual stress can be investigated as the internal pressure is completely unloaded. A test case where unloading occurs at $P = 0.28$ GPa is carried out and the residual stress after unloading in shown in Figure 2.11(a). Again, excellent agreement is found between simulation and analytical results. The unloading process is purely elastic without the occurrence of reverse plastic flow as indicated in Figure 2.11(b).

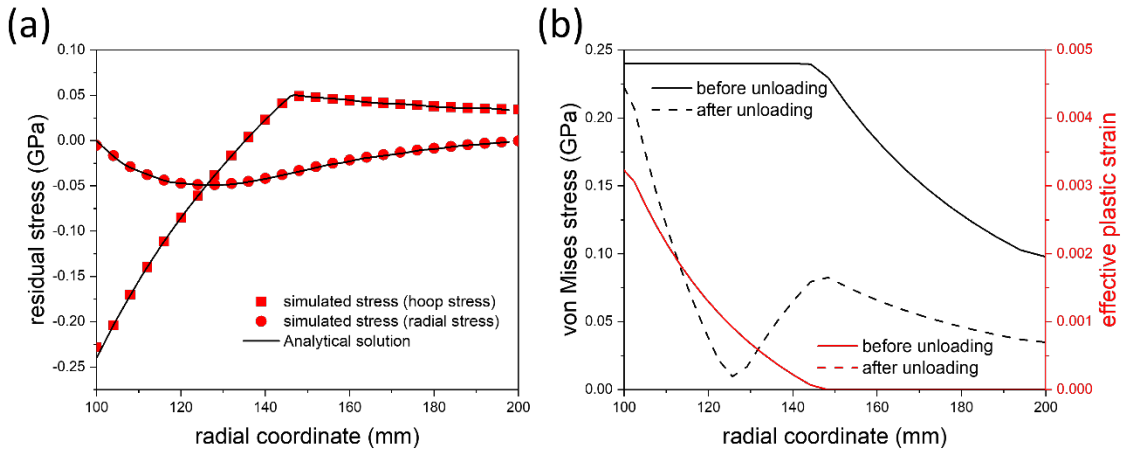

Figure 2.11. (a) Residual stress distribution along radial direction after unloading at $P = 0.28$ GPa ; (b) von Mises stress and effective plastic strain distribution before and after unloading.

Test case – heated internally pressurized spherical shell

The heat transfer model and the formulation of thermal strain is verified against a transient thermomechanical analysis of a heated spherical pressurized shell considering thermoelasticity. The geometry, boundary conditions and material properties are shown in Figure 2.12. One eighth of the spherical shell with a structured hexahedral mesh with 576000 cells is used for calculation.

(a)

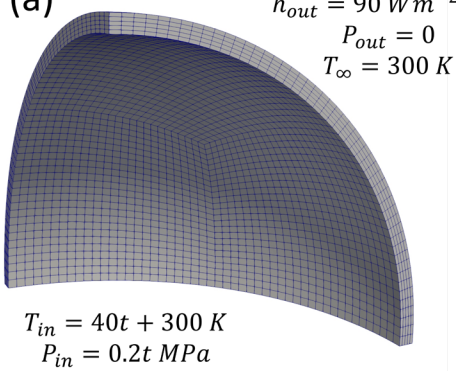

(b)

Young' modulus	$190\ GPa$
Poisson's ratio	0.305
Density	$7750\ kg/m^3$
Thermal expansion coefficient	$9.7 \times 10^{-6}\ K^{-1}$
Specific heat	$486\ J/K$
Thermal conductivity	$20\ W/mK$

Figure 2.12. The geometry, boundary conditions, and material properties of the heated spherical pressurized shell test case.

The shell is heated and pressurized at the inner surface with gradually increasing temperature and pressure. The outer surface is set as free surface without traction and is cooled by convective heat transfer. The initial temperature is 300 K and the shell is assumed to be stress free at the initial state. With a constant time step of 1 s, a total of 5 steps were simulated. The temperature and von Mises stress distribution along the radial direction across the shell thickness at 5 s is shown in Figure 2.13. The results from Afkar et al.[88] using FEM and Cardiff et al.[89] using FVM are plotted for reference. The heat transfer model is verified by the temperature distribution as little difference can be seen compared to reference results. For stress distribution, all results exhibit a similar trend and almost the same value at the outer surface of the shell. The simulation result shows good agreement across shell thickness with the FVM predictions from Cardiff et al. The difference prediction from Afkar et al. could result from the relatively coarse mesh. There were only 8 elements across the shell thickness in their study while a fine mesh with 30 cells were selected in the test case and the study from Cardiff et al.

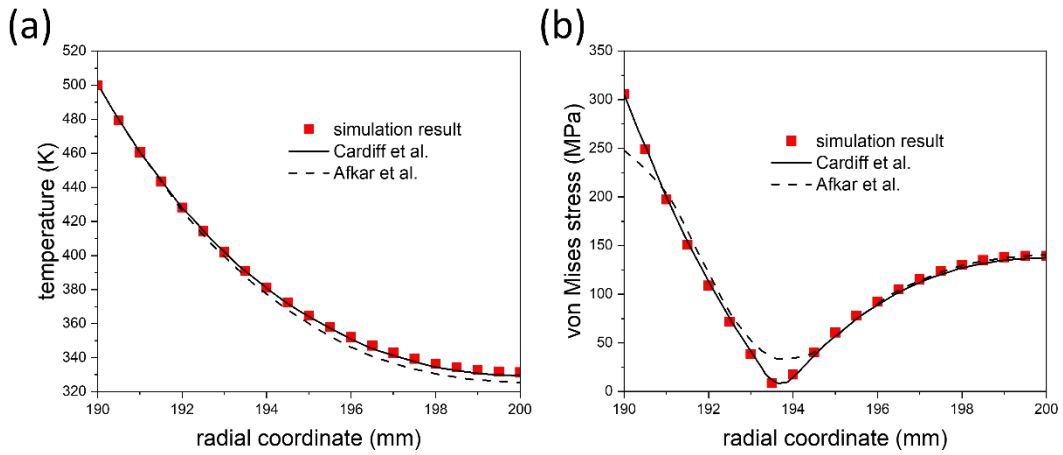

Figure 2.13. (a) Temperature and (b) von Mises stress distribution along radial direction across the shell thickness at 5 s. The results are compared with simulation data given from Afkar et al. and Cardiff et al.

As the stress results can be sensitive to the numerical grid, a grid dependence study is performed on this test case. Five different grids listed in Table 2.3 were evaluated for temperature and stress calculation.

Table 2.3. Five grids with different cell numbers for the spherical shell.

Mesh #	Cell numbers	Cell numbers in thickness direction
1	9375	5
2	27000	10
3	150000	20
4	576000	30
5	4800000	40

The predicted temperature and von Mises stress distribution across shell thickness at 5 s are shown in Figure 2.14. There is basically no difference between the predictions for different meshes in temperature distribution. Even the coarsest mesh should be sufficient for heat transfer calculation. However, for stress distribution, all predictions show a similar trend but the results are sensitive to the numerical grid. As the grid density is increased by refining the mesh, the stress calculation becomes mesh independent, and a grid convergence is reached.

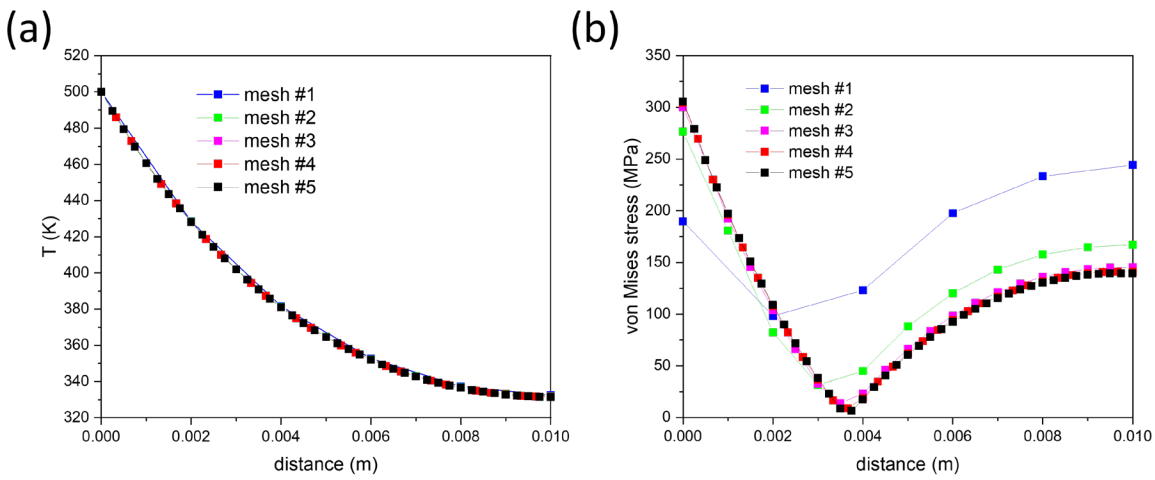

Figure 2.14. Comparison of the grid dependence of the (a) temperature and (b) von Mises stress distribution along radial direction across the shell thickness at 5 s.

3. STRESS DEVELOPMENT DURING COOLING OF CONTINUOUSLY-CAST BORON-CONTAINING STEEL SLABS

In this chapter, the thermomechanical model developed in Chapter 2 is applied to simulate the cooling process of a single continuously-cast steel slab. The effect of boron on stress development and phase evolution during cooling is investigated by simulating the air-cooling process in slabs of two similar steel grades, one with and the other without boron. Temperature history, phase transformation, and stress development during cooling are predicted in boron-containing and non-boron steel slabs. The effects of boron addition and different cooling rates on stress development are analyzed. As a method to control the cooling rate and lower the tensile stress level during cooling, the effect of slowing the cooling rate by using a radiation shield is also studied for the boron-containing steel.

3.1 Simulation setup and experimental method

The model is used to simulate the cooling of a large single steel slab due to heat loss from its surface as it is stored in the slab yard and is cooled in air. To investigate the effect of boron addition on the development of stress, strain, and microstructure, two test cases with the same geometry, initial condition, cooling condition but different chemical composition are analyzed.

3.1.1 Geometry and meshing of test cases

The geometry of the slab is shown in Figure 3.1, with a 4 m length, 1 m width, and 0.3 m thickness. Although typical slab length is around 8 to 12 m, 4-m length was chosen in this study to cut down the calculation time. Based on geometry study of slabs with different length, a longer slab length makes little difference in phase transformation and stress results at the region of interest labelled in Figure 3.1. Taking advantage of symmetry, only one-eighth of the slab volume is modeled to save computational time. A total of 48,000 hexahedral cells are used, with a uniform cell size of $2.5 \times 1.7 \times 0.75\ cm$.

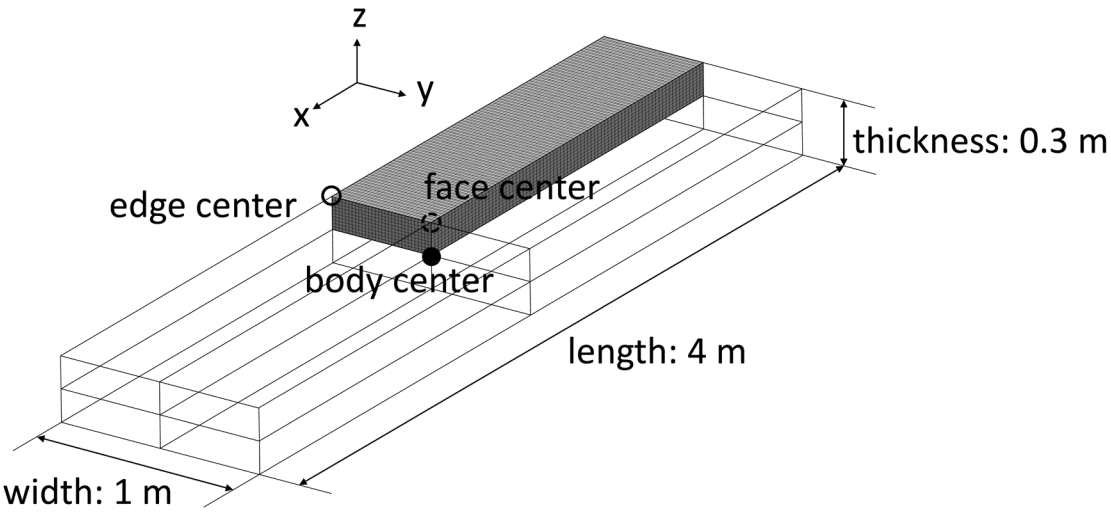

Figure 3.1. Geometry and mesh of the slab used for simulation. The numerical domain is only one-eighth of the slab, taking advantage of symmetry in geometry and boundary conditions

3.1.2 Initial and boundary conditions

The initial temperature of the slab is assumed to be uniform and is set as 830 °C which is higher than the A_3 temperature of the steel. The initial microstructure is assumed to be homogeneous and consists of 100% austenite. The uniform temperature profile assumption is adopted for simplicity. In reality, the temperature at slab core is higher than slab surface and corner. Since the steel shows a good ductility in the high temperature austenite region, the stress caused by this thermal gradient across the slab is expected to be small.

The thermal boundary condition for the slab surface includes radiation and natural convection by air. Some scale is assumed to be present, so the emissivity of the slab surface is set to 0.7[90]. The environmental temperature is assumed to be constant at 20 °C. For the mechanical boundary condition, the slab surface is assumed to be a free surface.

3.1.3 Material properties

The TTT diagrams of both non-boron steel and boron-containing steel used for phase transformation model are obtained from JMatPro (v.10.2)[73] prediction as shown in Figure 1.3. Temperature dependent phase transformation kinetics parameters are calculated based on these

diagrams and then curve-fitted to determine the temperature dependencies. The chemical compositions of steels used for simulation are listed in Table 3.1.

Table 3.1. Chemical composition of steels used for simulation (% in weight).

Steel type	C	B	Mn	Si
Boron-containing	0.09	0.0022	2.48	0.45
Non-boron	0.09	0	2.48	0.45

Temperature-dependent thermal and mechanical properties of the different phases in the two steels studied are also calculated by JMatPro and are shown in Figure 3.2. Because the only difference in composition between the two types of steel is the addition of less than 0.003 wt.% B, the difference in material properties is small, and therefore only properties for boron-containing steel is presented.

3.1.4 Experimental method

Steel samples for boron-containing steel (0.09 wt.% C, 0.45 wt.% Si, 2.48 wt.% Mn, 0.0022 wt.% B) and non-boron steel with no B and 0.06 wt.% C were prepared for microstructure study. The samples were cut from the surface of as-cast steel slabs. Prior to optical microscopy, the samples were polished and etched with 2% nital solution. For quantitative microstructure image analysis, ImageJ was utilized.

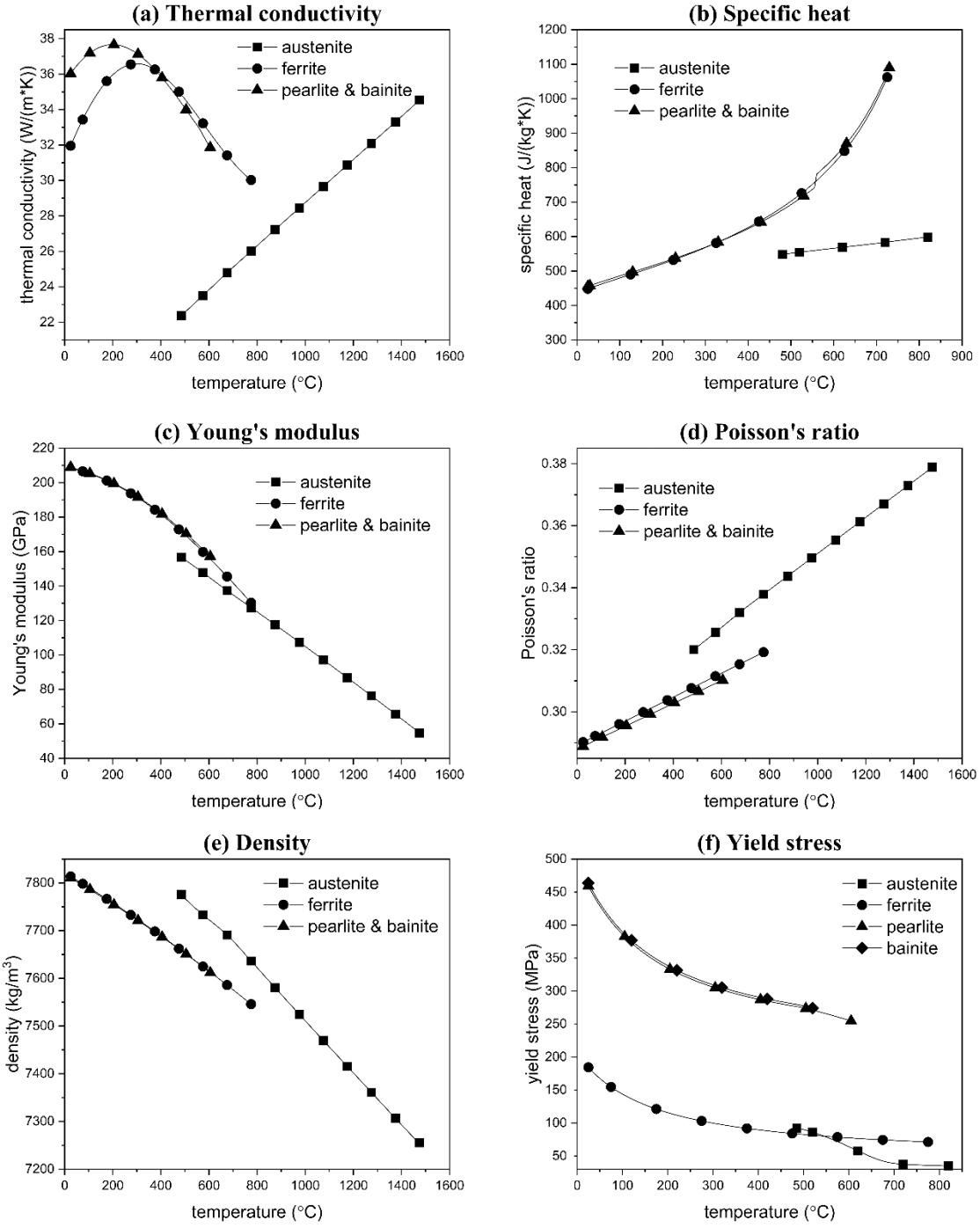

Figure 3.2. Temperature-dependent thermal and mechanical properties for the boron-containing steel calculated from JMatPro

3.2 Results and discussion

3.2.1 Effect of boron on phase evolution and stress development

The air cooling of non-boron and boron-containing steel slabs is simulated by the model. The comparisons of temperature history and phase evolution at center and edge of the slabs are presented in Figure 3.3. Although both slabs have the same initial state and thermal boundary conditions, the difference in phase transformation behaviors caused by boron addition significantly changes the phase evolution and the final phase distribution after cooling. Figure 3.3(a) shows that the non-boron steel consists of ferrite and pearlite with a variation in phase distribution between the center and edge of the slab. The center has more ferrite due to the slow cooling rate compared with the edge where 30% pearlite is predicted. Because boron addition delays the nucleation and growth of ferrite, as seen in the TTT diagrams in Figure 1.3, the steel with B evolves mostly bainite across the slab during cooling, Figure 3.3(b). Corresponding optical images, taken from the surface of the as-cast slabs, Figure 3.3(c) for steel without B and Figure 3.3(d) for steel with B, are in qualitative agreement with these predictions. The non-boron steel shows polygonal ferrite matrix with pearlite, while the boron-containing steel exhibits lath-like bainitic ferrite. In the microstructures of the real steel sample, the observed pearlite fraction at the surface of the as-cast non-boron steel slab is 6%, determined by the area fraction obtained using quantitative microstructure image analysis. Compared with the 30% pearlite calculated by simulation, the pearlite fraction is overpredicted for the steel slab without B. This results from the difference in chemical composition between the steel used in simulation and the actual as-cast steel slab. In order to study the effect of boron, the simulation assumes the non-boron steel has the same C fraction as the steel with B, which is 0.09 wt.%, while the actual non-boron steel slab only contains 0.06 wt.% of C. Lower carbon fraction can lead to less pearlite formation.

Besides the difference in phase evolution, the temperature histories are also different for steel with and without B due to the latent heat release. At the initial stage of cooling, the steel with B cools faster because no phase transformation occurs until 2000 s. For the steel without B, ferrite formation starts at around 60 s and the heat release from this phase transformation slows the cooling rate. As the cooling proceeds, bainite transformation occurs in the steel with B and the latent heat can even cause a plateau in temperature history at the center of the slab as shown in Figure 3.3(b) when t is around 10000 s.

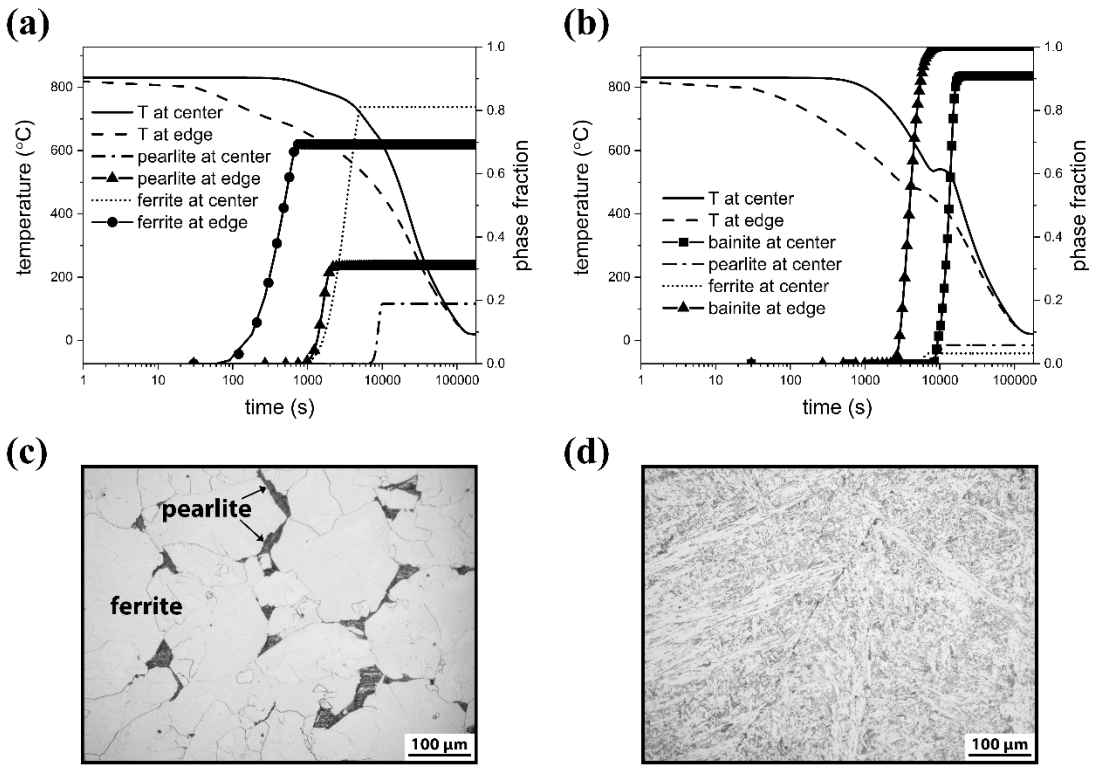

Figure 3.3. Predicted temperature history and phase evolution at center and edge of slab during cooling with corresponding optical images of (a), (c) non-boron steel and (b), (d) boron-containing steel.

The stress development during cooling is caused by the thermal and transformation strains. As the addition of boron significantly alters the phase transformation history, the internal stress evolution is also affected. Because the slab edges see a fast cooling rate and so are more susceptible to casting defects such as transverse corner cracks, the stress development at the edge is analyzed. Figure 3.4 shows the evolution of longitudinal stress at the edge of both steel slabs (where the metal cools faster), along with phase transformations during cooling. Due to the free surface mechanical boundary condition, the stress is 1-dimensional at the edge of slab and only σ_{xx} is presented while σ_{yy} and σ_{zz} stay at zero. At the beginning of cooling, high thermal gradient is developed at the edges and surface because of the fast cooling rate. As the surface contracts faster than the core, both cases show similar trends of a slowly growing tensile stress while the temperature gradient is the only cause of strain. Before phase transformations start, the entire slab

has a fully austenitic microstructure, with a low yield strength (<50 MPa) at high temperature (>600 °C).

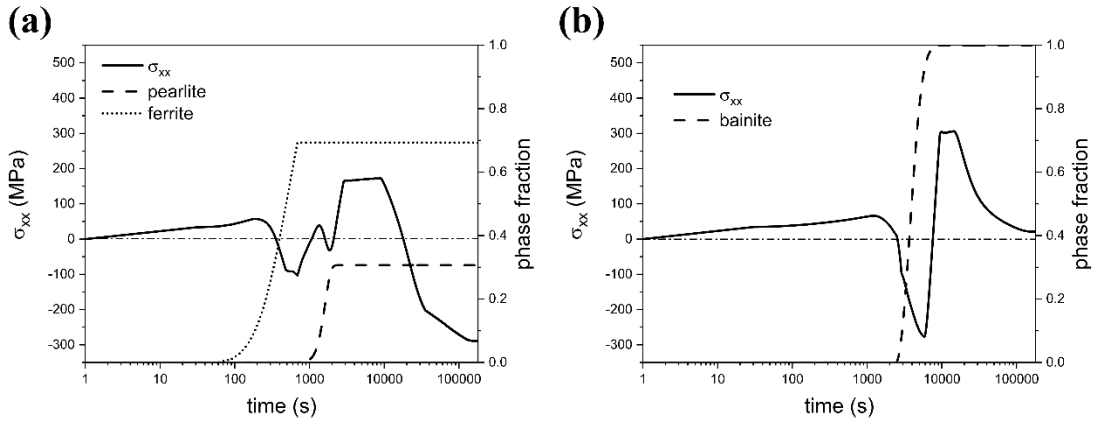

Figure 3.4. Development of 1-dimensional longitudinal stress in casting direction at the edge of slab with corresponding phase evolution of (a) non-boron steel and (b) boron-containing steel. Stress inversion is observed when phase transformation takes place.

For the non-boron steel shown in Figure 3.4(a), phase transformation from austenite to ferrite at the edge occurs after about 60 s of cooling. The magnitude of the existing tensile stress decreases with the formation of ferrite and the stress state changes to compression. This stress change results from the structural dilatation because ferrite has a lower density compared with austenite. As cooling proceeds, the compressive stress reaches peak value when ferrite transformation is finished. The magnitude of compressive stress then decreases and the stress state briefly becomes tensile again due to the continuing fast cooling at the edge. This pattern of stress inversion is repeated as the phase transformation from austenite to pearlite occurs. When the austenite is gone at the edge, a compressive stress state is predicted with a microstructure of ferrite and pearlite. At this stage, the temperature difference between the edge and the center of slab is larger than 200 °C and there is still phase transformation occurring inside of the slab. Therefore, another stress inversion from compression to tension is predicted at the edge. The tensile stress reaches a plateau as plastic deformation takes place and the peak stress is 172 MPa. At around 10,000 s, all phase transformations are done for the entire slab but there is still a nonuniform temperature distribution across the slab, with the center having a higher temperature. Therefore, with further cooling, the tensile stress at the edge decreases because of the thermal contraction at the center of slab. For non-boron steel, the final residual stress at the edge is in compression.

Stress development for the steel with B is shown in Figure 3.4(b). Because the phase transformation from austenite to bainite has the similar structural dilatation effect as austenite to ferrite and pearlite in the case of non-boron steel, the stress history has the same pattern of stress inversion. The peak compressive stress is predicted when bainite transformation is finished at the edge and the stress then becomes tensile as cooling continues. However, it has a peak tensile stress value of 305 MPa, which is 77% higher than the value predicted in the non-boron steel case. The higher peak value results from the high yield strength of bainite formed due to B addition instead of the soft ferrite phase.

The mean stress and effective plastic strain at the edge during cooling is shown in Figure 3.5. The mean stress follows a similar trend as the longitudinal stress in Figure 3.4(a), with the boron-containing steel slab exhibits a higher tensile stress than the non-boron steel. As fracture and cracking occurs more readily in a triaxial tensile stress state, the addition of boron will increase the likelihood for fracture near the edge of slab. During cooling, plastic deformation occurs due to the high thermal and phase transformation loads and relatively low yield strength of austenite at high temperature. The peak effective plastic strain for the boron-containing steel is predicted to be 1.3% compared with 0.3% for the non-boron steel. The results also indicate that plastic deformation occurs primarily in the early stage of cooling while the cooling rate is fast and as the phase transformation takes place. For the boron-containing steel, because of the delayed phase transformation, higher tensile stress and larger strain develop at the early stage of cooling and the soft austenite phase undergoes considerable plastic deformation.

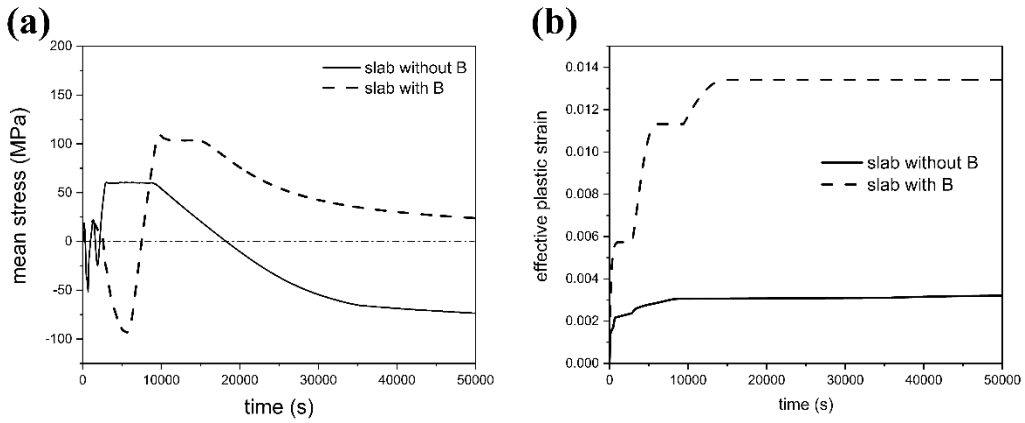

Figure 3.5. Development of (a) mean stress and (b) effective plastic strain at the edge of slab. The boron-containing steel exhibits higher tensile stress and larger plastic strain compared to the non-boron steel.

In addition to transverse corner cracks that occur at the slab edge, other defects such as surface cracks can also affect the quality of slabs. Accordingly, the stress development at the top surface center and body center of slab are investigated. As shown in Figure 3.6(a) and (b), for the stress at top surface of slab, σ_{xx} and σ_{yy} exhibit a similar trend while σ_{zz} remains zero. Comparing with the stress development at the edge in Figure 3.4, the same stress inversion pattern is observed for both non-boron and boron-containing steel as the cooling rate at the surface is also fast. The boron-containing steel exhibits a higher peak tensile stress and final tensile residual stress which may lead to surface cracking. For the boron-containing steel in Figure 3.6(b), the peak value of σ_{yy} reaches 330 MPa while σ_{xx} is around 200 MPa. This could favor the growth and propagation of longitudinal surface cracks.

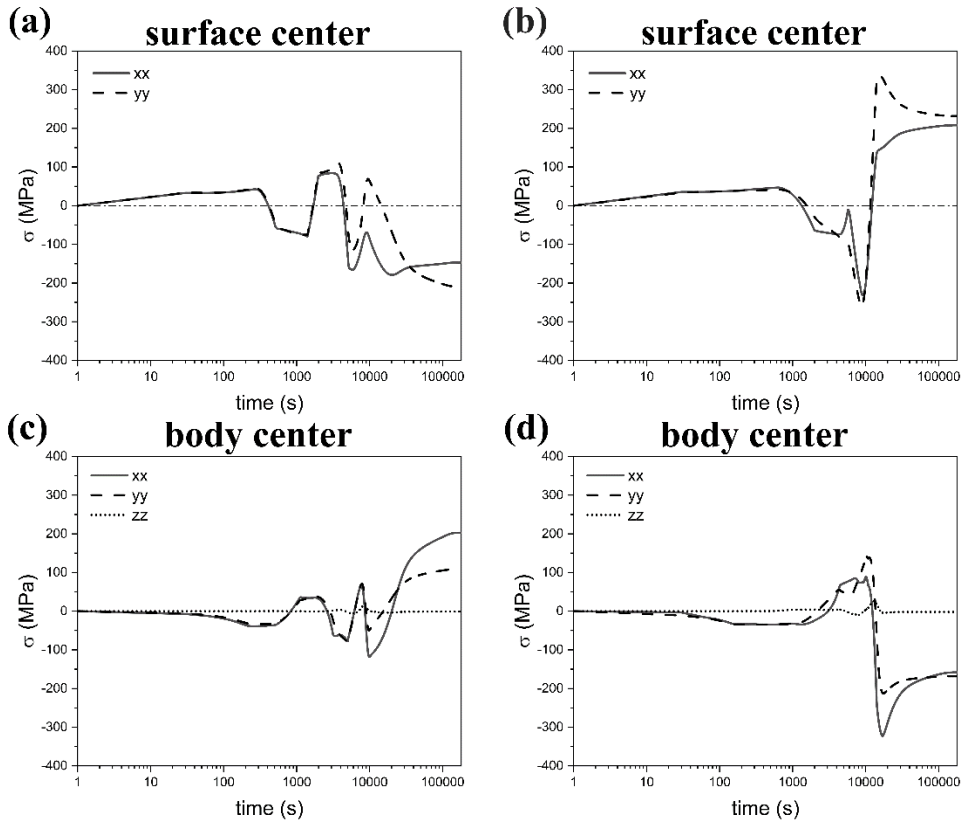

Figure 3.6. Development of 2-dimensional stress at the surface of slab and 3-dimensional stress at the center of slab for (a), (c) non-boron steel and (b), (d) boron-containing steel. The stress at surface shows a similar trend comparing with the stress at edge while the center shows the opposite sign of stress.

Figure 3.6(c) and (d) illustrate the 3-dimensional stress development at the body center of slab. Because of the slab geometry where thickness (z direction) is much smaller than length and width, the magnitude of σ_{zz} is always smaller than σ_{xx} and σ_{yy}. The stress inversion pattern at body center is opposite to that at the edge and surface of slab. This results from the high thermal gradient from slab surface to center. For instance, at the beginning of cooling, high thermal gradient is established at the surface. The constraint of the slow cooling core stays at high temperature and causes tension for the surface while the core is loaded in compression to balance the stress. After cooling, a tensile residual stress is observed for the non-boron steel while the boron-containing steel shows a compressive residual stress.

Comparison of the phase evolution and stress development between the two types of steel shows that the boron-containing steel with bainite microstructure exhibits higher stress and plastic strain during cooling. This difference may cause transverse corner cracks and surface cracks which can be detrimental for subsequent hot rolling process of slabs. Because the two slabs cool under the same cooling condition, the difference in stress development stems from phase evolution. Compared with the softer ferrite, the higher yield strength bainite could cause a higher stress concentration at where phase transformations take place. Therefore, to reduce the residual stress, a ferrite microstructure is preferred.

In addition, although the observation of stress and phase development is difficult to observe for the large continuously-cast slabs, the temperature measurement can be achieved. A combination of temperature history, final phase distribution, and residual stress measurement can be used for experimental validation of the simulation results in future work.

3.2.2 Effect of slow cooling rate

As more ferrite formation is favorable for developing less stress during cooling, measures to increase ferrite formation are considered. Because boron addition improves the hardenability of steel, a slower cooling rate is proposed to lower the stress level and reduce crack susceptibility for boron-containing steel slab. As indicated by the TTT diagrams, slower cooling will result in softer ferrite formation and a phase distribution more like the non-boron steel. The cooling rate is slowed in steel industry [42] by stacking multiple slabs or by covering the slab with thermal shield or hood. The use of the latter method to reduce heat loss has been studied as part of a hot rolling mill[91].

To investigate the stress and phase evolution of boron-containing slabs with cooling rates slower than the results shown above in Figure 3.3, several test cases are simulated. Mansouri et al.[91] studied the effect of a thermal shield on steel strips in a hot rolling mill and found that a reduction of 45% in heat loss can be obtained. Using those results as a guide, slow cooling processes were achieved in our model by setting the heat loss as 50%, 25%, and 10% of those calculated in the original test case (the "normal cooling" condition).

The temperature histories and ferrite phase evolution at the slab edge in the slow cooling cases are shown in Figure 3.7. The slower cooling rates increase ferrite formation in the boron-containing slab. For the case with the slowest cooling rate, 23% of the volume is predicted to form ferrite at the edge of slab, but that is still much less than the 70% ferrite formed for the non-boron steel at the normal cooling rate.

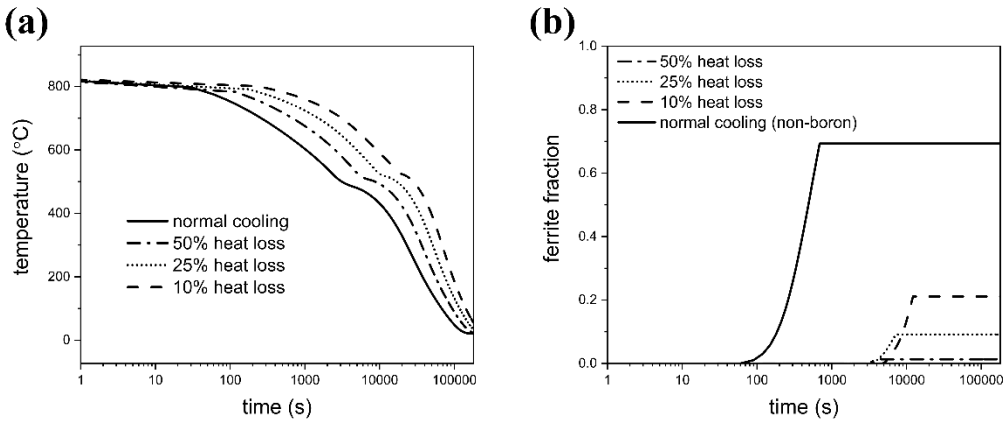

Figure 3.7. (a) Temperature history and (b) ferrite phase evolution at the edge of slab for slow cooling cases of boron-containing steel. The ferrite evolution in the normal cooling case of the non-boron steel is plotted in (b) as the solid line.

Figure 3.8 illustrates the effect of slow cooling on stress development and plastic deformation for the boron-containing steel. As shown in Figure 3.8(a), the peak value of the tensile longitudinal stress at the edge decreases with decreasing cooling rate. Because only a very small amount of ferrite is formed in the 50% case, there is little reduction in the peak stress. Although the change in peak stress is small, the residual stress for 50% heat loss case actually increases. Note that the tensile stress decreases from peak value due to the thermal strain after phase transformation is finished. For the 50% heat loss case, although the effect of changing phase

evolution is not significant, a smaller thermal gradient is achieved and hence the decrease from the peak stress is also smaller, causing a higher tensile residual stress. To effectively lower the peak stress, the cooling rate must be slower. The 10% heat loss case shows that the peak tensile stress can be reduced to only 250 MPa. The corresponding effective plastic strain is also predicted to decrease for slower cooling cases, Figure 3.8 (b). The effective plastic strain in the 10% heat loss case can be reduced to a level similar to the non-boron steel, due to the lower temperature gradient throughout the process and higher ferrite formation.

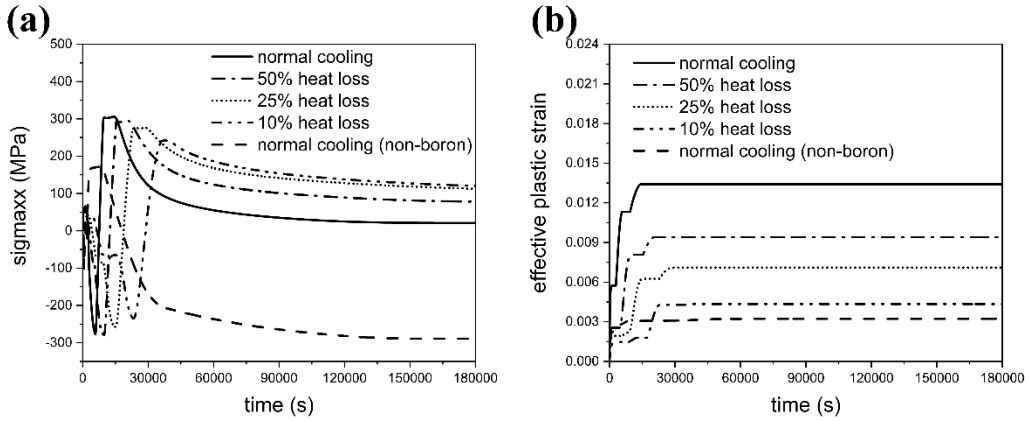

Figure 3.8. Development of (a) longitudinal stress and (b) effective plastic strain at the edge of slab for slow cooling cases of boron-containing steel. The dashed line represents the normal cooling case of non-boron steel.

According to the simulation results of the reduced cooling rate cases, the lower cooling rates effectively reduces stress levels and plastic deformation below a critical cooling rate. The 50% heat loss case, which may be done in practice by applying a thermal shield on top of a single slab[91], is not sufficient to effect a practical change in the residual stress. To achieve a slower cooling rate, both controlled cooling and stacking of multiple slabs might be adopted, although the 10% case, a 90% reduction in the heat loss rate, would still be very difficult to achieve in practice. The effect of stacking slabs on cooling rate, microstructure and residual stress and strain is discussed in Chapter 4.

3.2.3 Slab geometry study

The geometry of slab also affects the cooling process. Because the slab cools by heat extraction from surface, different slab sizes could result in different thermal gradient across the

slab. Therefore, a geometry study on the effect of the size of slab is performed for the single slab cooling process. The original geometry shown in Figure 3.1 has a length of 4 m, width of 1 m, and thickness of 0.3 m. The width and thickness of slab is determined by the width and thickness of the mold respectively. The width usually ranges from 0.9 m to 3 m and the thickness from 0.2 m to 0.3 mm for conventional slab casters[92]. The length of slab is controlled by the time interval of the torch cutting process after casting and can range up to 12 m. Three test cases for boron-containing steel with different length, width, and thickness are studied and the results are compared with the original test case. The dimension of slabs for these test cases are listed in Table 3.2.

Table 3.2. Dimension of slabs used in geometry study (in m).

Case number	Length (L)	Width (W)	Thickness (T)
1	4	1	0.3
2	8	1	0.3
3	4	2	0.3
4	4	1	0.2

The comparison of temperature history at the edge (solid line) and center (dashed line) of slab is presented in Figure 3.9(a). Because the temperature at the edge is mainly affected by convection and radiation cooling, the effect of slab dimension is less significant and only case 4 with a smaller thickness shows a minor increase in cooling rate. Cooling is achieved by heat conduction at the slab center and the dimension of slab determines the distance that the heat must travel. Comparing with width and length of slab, the thickness is much smaller and therefore cooling is dominated by heat conduction in thickness direction. Doubling the length and width of slab shows little difference in cooling curves while decreasing thickness leads to a much faster cooling rate. The effect of slab dimension on stress is demonstrated in Figure 3.9(b) and (c) as the development of σ_{xx} at the edge of slab and the final residual stress distribution at transverse section of slab are plotted. A similar trend with a peak tensile stress as around 300 MPa is observed for all cases. Case 2 with 8-m length shows almost identical stress curve as case 1 with 4-m length indicating that increasing slab length does not affect the stress development at the longitudinal edge of slab. However, doubling the width of slab results in a compressive residual stress state (-100 MPa) at the slab edge after cooling due to the increased thermal gradient in width direction. For the influence of slab thickness, the stress curve is slightly shifted to the left because of the faster cooling rate resulted from shorter thickness.

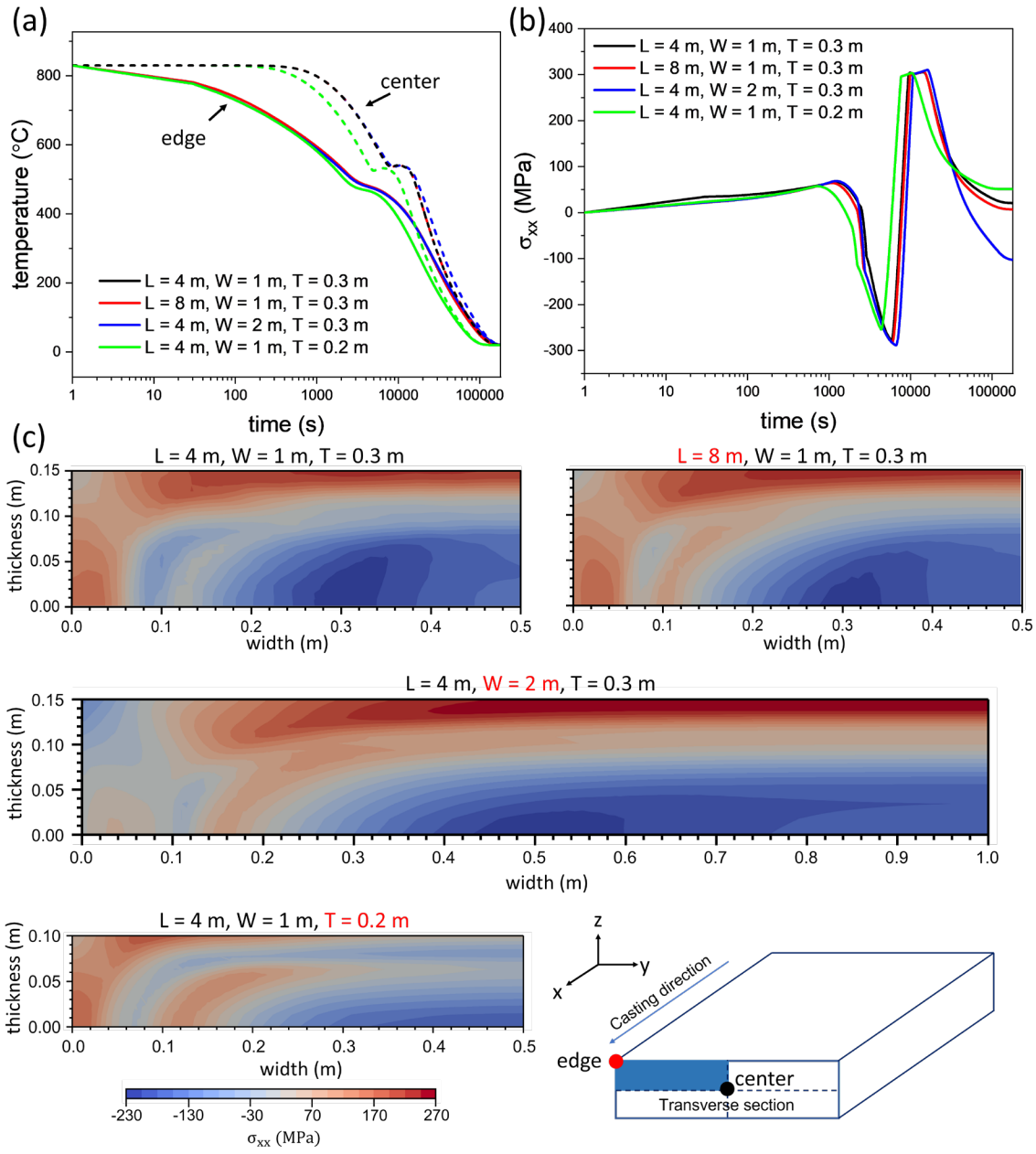

Figure 3.9. Comparison of (a) temperature history and (b) stress development, (c) final residual stress distribution of σ_{xx} across the transverse section for slabs with different dimensions. The schematic indicates the position of slab edge, center, and the cross section.

3.2.4 Effect of asymmetric cooling

Symmetric cooling conditions have been applied in previous test cases for the single slab cooling process. In reality, the cooling conditions are usually asymmetric especially for the top and bottom surface of slab. This could lead to asymmetric temperature, phase, and stress distribution. Moreover, the flatness defects such as slab bowing also result from asymmetric cooling. To investigate the effect of asymmetric cooling condition, a test case for single slab cooling of boron-containing steel is performed. The top surface of the slab is set as the slow-cooling surface with a heat loss as 50% of the bottom surface. Due to the asymmetry in thickness direction, one-fourth of the slab volume is modeled as shown in Figure 3.10.

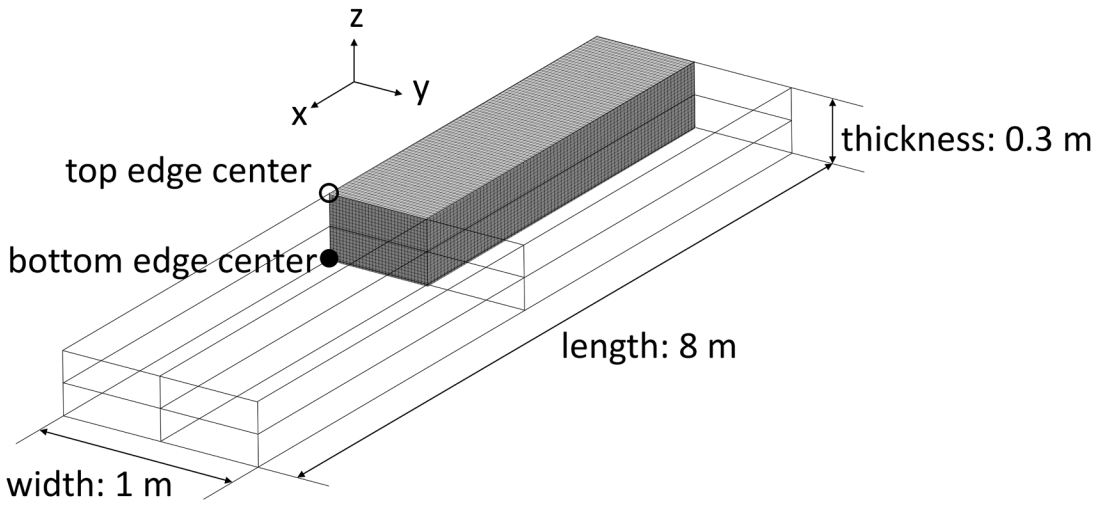

Figure 3.10. Geometry and mesh of the slab used for simulation of asymmetric cooling. The numerical domain is one-fourth of the slab. The top surface of slab is the slow-cooling surface.

The stress development at the top and bottom edge center of slab is shown in Figure 3.11(a) for the asymmetric cooling case. Compared with the symmetric cooling case, a slight delay of stress inversion caused by bainite formation is observed because of the slower cooling rate on the top surface. The stress development still follows the same trend in asymmetric cooling case as bainite transformation is still the dominate phase transformation during cooling, especially at the surface of slab. Figure 3.11(c) shows the deformation of slab at different stage of cooling. Bowing of slab in thickness direction (z-direction) occurs because of the asymmetric cooling from top and bottom surface. At 2400 s when phase transformation has not started, the faster cooling rate at the

bottom surface of slab leads to more thermal contraction and the slab bend downwards. The maximum displacement in z-direction can reach 4.8 cm. Since the bottom surface cools faster, bainite formation first occurs at bottom surface and the phase transformation strain from volume expansion of bainite starts to bend the slab upwards as shown in Figure 3.11(c) at 9000 s. Therefore, the deformation of slab is closely related to the cooling conditions and significant difference at top and bottom surfaces during cooling should be avoided to prevent large deformation. This can be achieved by multiple slabs stacking as it helps control cooling conditions and also applies additional force on top of the slab. Discussion of the strategy for slab stacking to prevent slab bowing is included in Chapter 4.

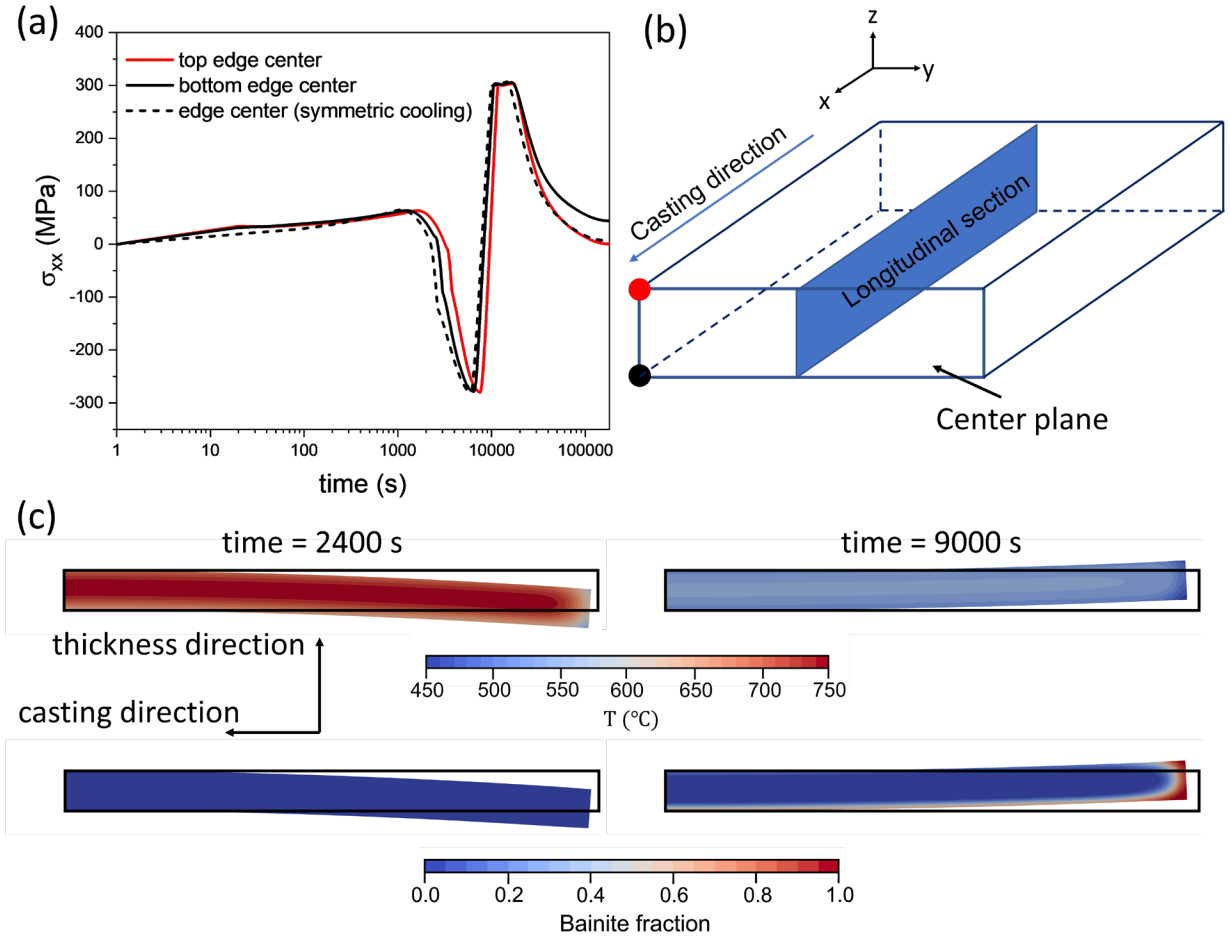

Figure 3.11. (a) Stress development at top and bottom edge center of slab compared with the stress curve at the edge center for symmetric cooling case (dashed line); (b) schematic of half of a slab showing the edge centers and the longitudinal section; (c) deformation of slab viewing from the width direction. The black outline indicates the original shape of the slab before cooling. The deformation is scaled up with a factor of 3.

3.3 Summary

A finite volume method based model, coupling conduction heat transfer, elastic and plastic deformation, and steel phase transformation calculations, was developed in the OpenFOAM platform. The model was used to simulate the cooling process of continuously-cast steel slabs. The following conclusions can be drawn from the comparison of simulation results for boron-containing steel and non-boron steel:

1. Under the same cooling condition, due to the change in phase transformation behaviors by boron addition, the boron-containing steel slab consists of mostly bainite with little ferrite and pearlite at the center of slab, while the non-boron slab consists of ferrite and pearlite with more than 80% ferrite at the center after cooling.
2. Higher tensile stress and plastic strain are predicted for the boron-containing steel at the edge of slab. The high stress concentrated at edge may lead to post-casting defects such as transverse corner cracks. For steel with less than 5 ppm boron addition to improve hardenability, this effect should be considered in the cooling of as-cast slabs.
3. Slow cooling rates will affect the stress development by changing the temperature gradient and phase evolution during cooling. Lower stresses and smaller plastic strains can be achieved below a certain critical cooling rate of continuously-cast steel slabs, but those cooling rates may be difficult to produce in practice.
4. The geometry of steel slab and asymmetric cooling conditions have little influence on stress development at the surface of slab during cooling. However, for a slab with a large difference between cooling conditions at the top and bottom surfaces, slab bowing with large deformation can be observed.

Therefore, to reduce the tensile stress developed at the edge of slab during cooling of boron-containing slab and prevent slab bowing, multiple slabs stacking might be helpful, and its effect will be discussed in Chapter 4.

4. INVESTIGATION OF COOLING PROCESS OF MULTIPLE STEEL SLABS STACK

In this chapter, numerical simulations of cooling process are performed to investigate the role of steel slabs stacking on cooling rate, phase evolution, stress development and slab deformation for a stack of multiple steel slabs. Continuously-cast steel slabs are usually stored in the slab yard of a steel plant as stacks built up by stacking multiple slabs on top of each other. As the stacking strategy is adopted to save the limited space in the slab yard, it also affects the cooling process of steel slabs. When multiple slabs are stacked together, the total area of slab surface where heat is extracted by convection and radiation through the air is reduced and thus a slower cooling rate compared to individual slab cooling can be achieved. As discussed in Chapter 3, slow cooling rate can lower stress developed during cooling of boron-containing steel slabs and result in more ferrite formation. In addition to cooling rate, the stacking of slabs is also used to avoid the slab bowing defect due to asymmetric cooling for the top and bottom surface of slab. The compressive mechanical load provided by top slabs above the slab can prevent large deformation and flatten the slab during cooling.

The objective of this chapter is to investigate the stacking strategy of steel slabs and its influence on the cooling process based on numerical simulations. The temperature history during cooling of a 9-slab stack is predicted and compared with experimental measurements. The cooling of a 5-slab stack is simulated to study the effect of the number of slabs in a stack. The phase evolution and stress development are examined for each case. Because slabs at different position of a stack are under different cooling conditions, the results at different locations of a stack are inspected. Finally, a case with the combination of slab stacking and radiation shield is modeled to study the stress development under a slow cooling rate that is feasible in practice.

4.1 Model setup for multiple steel slabs stack

4.1.1 Contact interface

In addition to the standard thermomechanical model described and used in the preceding sections, model modification is required for the simulation of multiple steel slabs stack as the contact interface between slabs need to be considered for both mechanical and thermal calculation.

The treatment of contact interface as contact boundary condition is complicated because the boundary condition depends on the solution and need to be updated iteratively[82].

At the beginning of cooling process, all slabs are assumed to be flat and in perfect contact condition where there is no gap between slabs. Therefore, the contact area A_c between two slabs equals to the area of the top/bottom surface of a slab. For mechanical load on one of the slab, uniform compressive pressure P_{top} and P_{bottom} are applied as boundary condition to the top and bottom surface respectively by Eq. (4.1).

$$P_{top} = \frac{nmg}{A_c}$$
$$P_{bottom} = \frac{(n+1)mg}{A_c} \tag{4.1}$$

where n is the number of slabs on top of the slab, m is the weight of a slab, and g is the magnitude of gravity. As cooling proceeds, deformation of the slab causes displacement in thickness direction (D_z) for top and bottom surface of the slab and a gap forms between slabs. During the iterative solution, the displacement D_z is checked for the entire surface to determine the contact area. For the region of contact, the compressive pressure is applied using Eq. (4.1) and the updated contact area. A traction-free boundary condition is applied for the region outside of contact. For simplicity consideration, only one of the multiple slabs in the stack is taken for stress calculation and other slabs are treated as rigid body. The assumption is made based on the previous study of the single slab cooling case. Firstly, the deformation is small during cooling of slab. According to the study of asymmetric cooling conditions in Chapter 3, the gap size during cooling is less than 5 cm for a slab with a length of 8 m. Secondly, the stress induced by the compressive pressure at contact region is insignificant compared to stress caused by thermal and phase transformation strain during cooling.

For thermal calculation, all slabs in the stack are considered. At the region of contact, the thermal boundary condition is set as thermal conduction across the interface. Outside of the contact region, heat transfer is due to radiation and conduction through air in the gap. Because of the small temperature difference between the two surfaces of the gap and the low thermal conductivity of air, the heat flow at regions outside of contact is neglected and the thermal boundary condition is assumed to be adiabatic.

4.1.2 Geometry and test case setup

The geometry of the test case for a 9-slab stack is shown in Figure 4.1. To better represent the heat transfer between stacked slabs and ground, a section of the ground beneath the slabs is added to model with the dimension indicated in Figure 4.1(a). The 9 slabs are stacked on top of each other with a dimension of 8 m length, 1 m width, and 0.3 m thickness for each slab as shown in Figure 4.1(b). Taking advantage of the symmetry condition, only one-fourth of the slabs and ground is modeled. A total of 500,000 hexahedral cells are used for the test case.

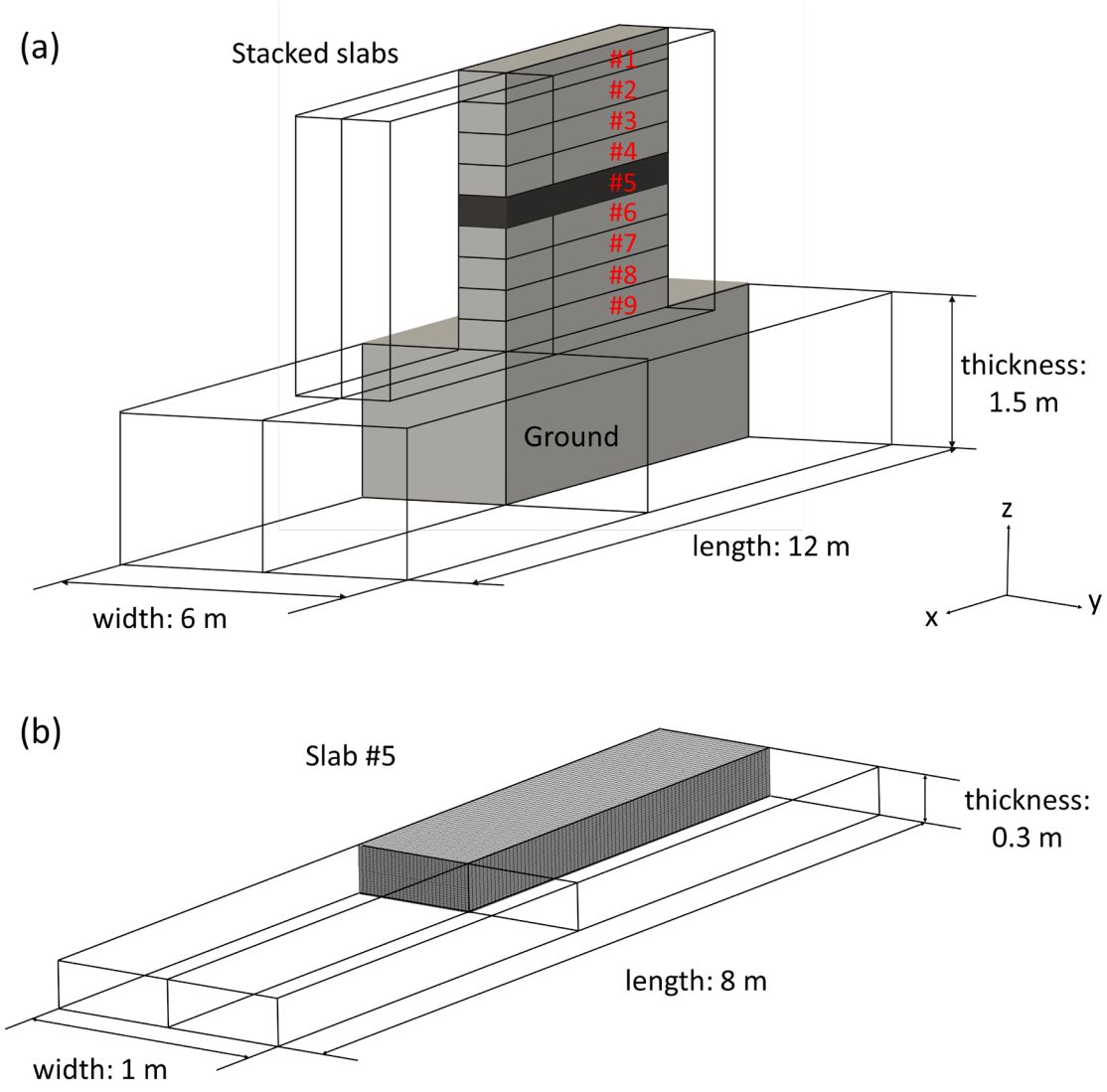

Figure 4.1. Geometry and mesh of the 9-slab stack test case. (a) dimension for the whole test case including the ground section; (b) geometry and mesh of slab #5. The numerical domain is one-fourth of the slabs and ground due to symmetry condition.

The initial temperatures and microstructures of the slabs in the 9-slab stack are listed in Table 4.1. For each slab, the temperature and microstructure are assumed to be uniform. In practice, dummy slabs are placed on top of the stack of hot slabs to avoid slab bowing. Therefore, the two slabs at the top of the stack and the slab at the bottom of the stack are set at ambient temperature (20 °C). Since it takes time to complete the stacking operation, there is a temperature difference for the 6 hot slabs (#3 - #8). The initial microstructure is assumed to be homogeneous and consists of 100% austenite for the hot slabs. Since the cold slabs at top and bottom of the stack do not undergo phase transformation, the initial microstructure is assumed to be 100% bainite. The initial temperature for the ground is assumed to be uniform at ambient temperature.

Table 4.1. Initial temperatures and phase distributions of slabs in the 9-slab stack.

Slab number	**#1**	**#2**	**#3**	**#4**	**#5**	**#6**	**#7**	**#8**	**#9**
Temperature (°C)	20	20	830	810	790	770	750	730	20
Phase distribution	100% B	100% B	100% A	100% A	100% A	100% A	100% A	100% A	100% B

Note: A = austenite, B = bainite.

The thermal boundary condition for the outer surface of slabs includes natural convection by air and radiation. The contact interfaces between slabs are implemented as thermal conduction and insulation respectively as described in previous section. For the ground section, the top surface is also cooled by natural convection and radiation. The bottom and side surfaces are set as a fixed temperature condition at ambient temperature. For the mechanical boundary condition, the top and bottom surfaces of the slab #5 are set using the contact interface condition. The side surfaces of the slab are assumed to be free surfaces.

To investigate the effect of the number of slabs in a stack, another test case for a 5-slab stack is modeled with the initial conditions listed in Table 4.2 where slab #i is the top slab and slab #v is the bottom slab. The dimension of slab and boundary conditions are set as the same as used for the 9-slab case. The stress calculation is performed for slab #iii at the middle position of the stack.

Table 4.2. Initial temperatures and phase distributions of slabs in the 5-slab stack.

Slab number	**#i**	**#ii**	**#iii**	**#iv**	**#v**
Temperature (°C)	20	830	810	790	20
Phase distribution	100% B	100% A	100% A	100% A	100% B

Note: A = austenite, B = bainite.

The materials properties for the slabs are the same as the properties used for the boron-containing steel in Chapter 3. To complete the thermal conduction calculation for the ground section, the thermal properties of ground are set according to the properties of soil investigated by Selker and Or[93]. Although the thermal properties of soil vary with soil contents, the relatively low thermal diffusivity compared with steel has insignificant influence on the temperature calculation of the slabs. Therefore, the thermal properties are assumed to be constant and uniform as the thermal conductivity $k = 1.5\ Wm^{-1}K^{-1}$, the specific heat capacity $c_p = 1500\ Jkg^{-1}K^{-1}$, and the density $\rho = 2000\ kgm^{-3}$.

4.2 Results and discussion

4.2.1 Cooling process of a stack with multiple slabs

The air cooling processes of the 9-slab stack and 5-slab stack of boron-containing steel are simulated by the model. The temperature histories and phase evolutions at the center of the top surface of slab #5 in the 9-slab stack and slab #iii in the 5-slab stack are presented in Figure 4.2. The results are compared to the experimental measurement of a 9-slab stack air cooled in the slab yard and the predicted result for air cooling of a single slab from Chapter 3. Although the air cooling condition is the same, the stacked slabs show different cooling curves as they cools much slower than the single slab as shown in Figure 4.2(a). It takes around 48 hours for the single slab to cool down to ambient temperature while the cooling time for the slab in the 9-slab stack is more than 100 hours. Compared to the experimental measured cooling curve, the simulated result shows a faster cooling rate. This difference could result from the heat conduction calculation at the interfaces between slabs in the model. For the two surfaces in contact, heat conduction is calculated assuming the temperature are the same for both surfaces with thermal contact resistance neglected. In reality, due to the surface roughness effect, there could be temperature drop across the interface and thus the heat flow is reduced.

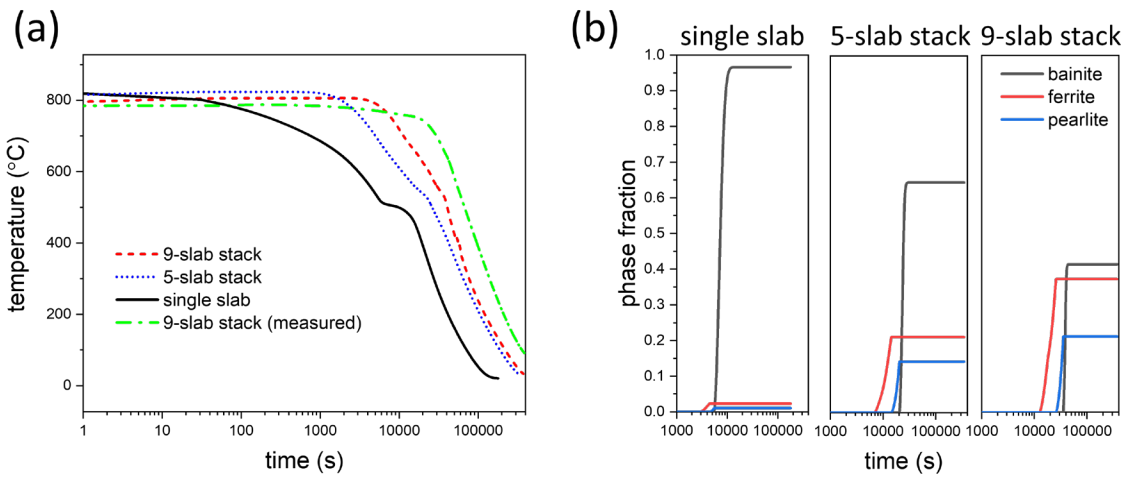

Figure 4.2. Predicted (a) temperature histories and (b) phase evolutions at the center of top surface of the slab #5 in the 9-slab stack and slab #iii in the 5-slab stack. The results are compared to experimental measurement and simulation results for the cooling of a single slab.

The slower cooling rates of the stacked slabs has significant influence on the phase evolution as illustrated in Figure 4.2(b). During the cooling of single slab, austenite transforms to mostly bainite across the slab. The final phase distribution after cooling shows more than 95% of bainite at the top surface of the slab. For the stacked slabs, the slower cooling rates result in ferrite formation even at the surface of the slabs. For the slab in the 5-slab stack, the bainite fraction is reduced to 64%. Furthermore, in the 9-slab stack, the final phase distribution of the slab shows 37% of ferrite, 21% of pearlite, and 42% of bainite.

The change in cooling rate caused by slabs stacking also affects the stress development during cooling by thermal and phase transformation strain. The stress development at the edge of the slab during cooling is analyzed for the stacked slabs as shown in Figure 4.3(a). Compared to the single slab cooling case, a similar trend of stress history is found in the stacked slabs. Two major differences can be observed in stress development at the edge of slab. Firstly, the stress curves are shifted to right for the stacked slabs due to the slower cooling rates. Phase transformation from austenite to ferrite does not occur until 3000s for the slab #5 in the 9-slab stack. For the single slab case, bainite transformation starts before 2000s and no ferrite forms at the edge of slab. Secondly, a much lower peak tensile stress, 180 MPa, is predicted for 9-slab stack case, which is 41% lower than the value predicted in the single slab case. However, the cooling rate for the slab in the 5-slab stack is not slow enough to reduce the peak tensile stress.

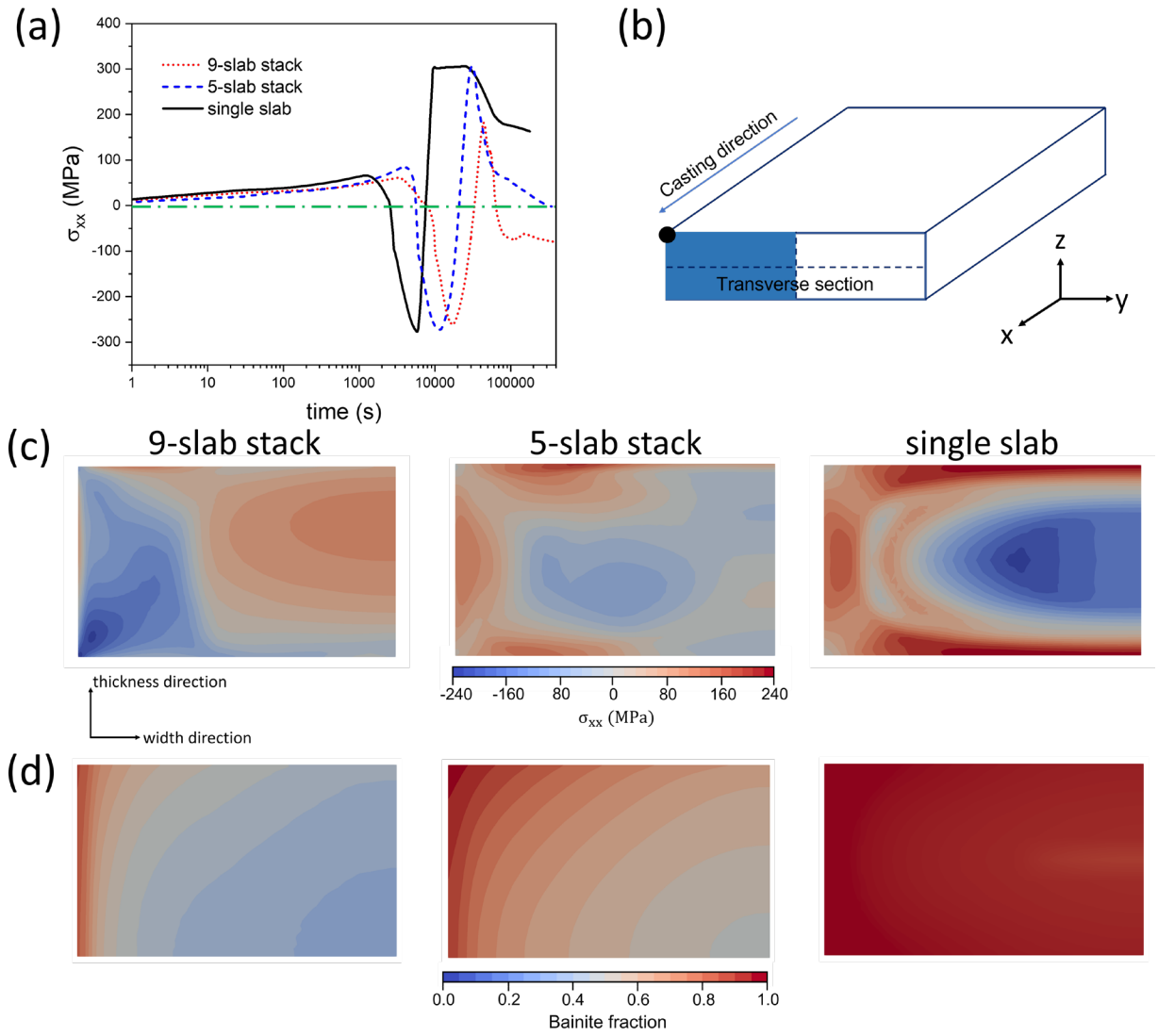

Figure 4.3. (a) Development of longitudinal stress σ_{xx} in casting direction at the top edge center of slab;(b) schematic of half of a slab indicating the location of top edge center and transverse section; (c) distribution of residual stress σ_{xx} and (d) bainite distribution at the transverse section for slab #5 in the 9-slab stack, slab #iii in the 5-slab stack, and single slab, respectively.

The residual stress distribution at the transverse section after cooling for all cases are plotted in Figure 4.3(c). In agreement with the stress development curves at the edge, the distribution shows a lower tensile residual stress at the surface for the stacked slabs. For the single slab case, according to the bainite distribution shown in Figure 4.3(d), the final microstructure is almost uniform with more than 95% bainite across the slab. Therefore, the residual stress is only related to the plastic deformation history. The surface of slab with a faster cooling rate exhibits tensile

residual stress while the core of slab is in compression for stress balance as indicated in Figure 4.3(c). On the contrary, a compressive residual stress is predicted at the surface of the slab in the 9-slab stack, For the stacked slabs, the side surfaces that are exposed to air cool much faster than the core and this leads to a nonuniform microstructure after cooling. As illustrated in Figure 4.3(d), the side surface shows phase distribution with 85% of bainite while the core of slab only has 30% of bainite for the slab in the 9-slab stack. Thus, a difference in yield strength across the width direction of the slab is predicted where $\sigma_Y = 420\ MPa$ at the surface and $\sigma_Y = 320\ MPa$ at the center. The higher yield strength at the surface prevents plastic deformation at the surface during cooling. This explains why the stress development curve at the edge does not show a plateau after the peak tensile stress.

Comparison of the stress development and phase evolution between the stacked slabs case and the single slab case shows that the stacking of slab can slow the cooling rate during air cooling of steel slabs. Depending on the stacking condition, the stacked slabs could exhibit lower tensile stress at the edge of slab and even show compressive residual stress at the outer surface if the cooling rate is sufficiently slow. One approach to achieve a slower cooling rate is by increasing the number of slabs in a stack. The change in stress development is beneficial for inhibiting crack initiation and propagation at the surface of slab during cooling. It is worth noting that the non-uniform phase distribution for the stacked slabs does not cause quality issues because these slabs require subsequent hot rolling in which the non-uniform phases will be fully austenitized by reheating.

4.2.2 Effect of slab position in a stack

Simulation results of the 9-slab stack demonstrates the influence of slabs stacking on the cooling process of boron-containing steel slabs. The stress development results obtained are for the slab #5 in the 9-slab stack where there are 4 slabs both above and below the slab. According to the case setup, slabs at different positions of the stack have different initial temperatures and cooling conditions. In addition, the compressive load provided by slabs above also varies with slab position. Therefore, the effect of slab position is investigated to better understand the stacking strategy. The stress calculation is performed for slab #4 and slab #6 in the stack shown in Figure 4.1(a) with 3 and 5 slabs above the slab respectively.

The cooling curves and phase evolutions at the center of the top surface of slab #4, #5, and #6 are presented in Figure 4.4. According to Figure 4.4(a), slab #4 at higher position shows the fastest cooling rate while slab #6 at lower position shows the slowest cooling rate. The difference in cooling rates is only caused by the heat conduction at top and bottom surfaces of the slabs as the cooling conditions are the same at the side surface with radiation and natural convection in air. For the bottom slab in contact with ground, the heat is extracted by the conduction through the ground. Compared to the top slab that are exposed in air, the bottom slab cools with a slower rate due to the low thermal diffusivity of ground (5×10^{-7} m^2/s). Correspondingly, the phase evolutions shown in Figure 4.4(b) exhibit that slab #4 consists of 76% of bainite, 12% of ferrite, and 12% of pearlite after cooling while 36% of bainite, 46% of ferrite, and 18% of pearlite is predicted for slab #6. The results indicate that effect of slabs stacking on slow cooling rate and ferrite formation is more significant for slabs at lower levels in a stack of multiple slabs.

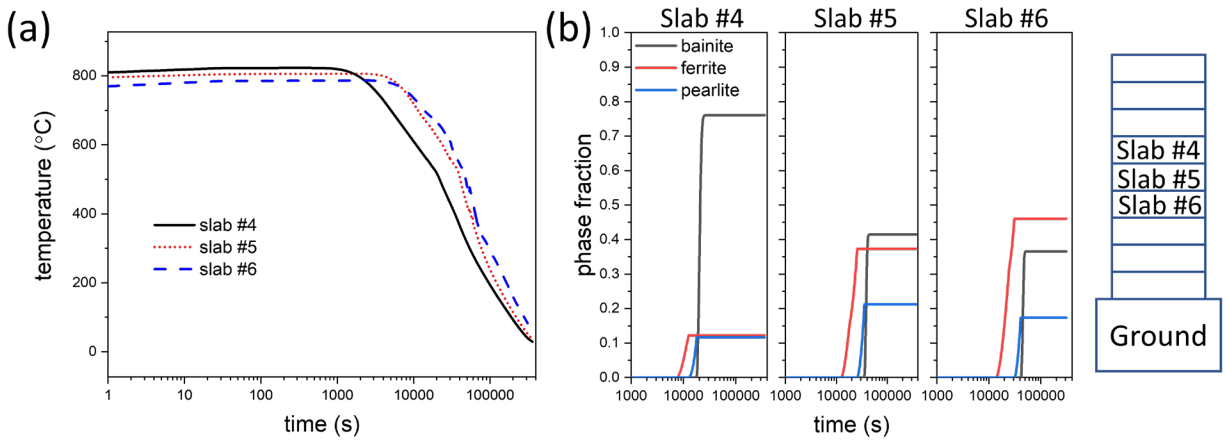

Figure 4.4. Predicted (a) temperature histories and (b) phase evolutions at the center of top surface of the three slabs (slab #4, #5, #6) at different positions of the 9-slab stack as indicated by the schematic.

Effect of slab position on stress development during cooling is illustrated in Figure 4.5(a) by comparing the predicted stress development at the top edge center of the three slabs. Slab #6 at lower position shows the lowest peak value of longitudinal stress σ_{xx} at the edge because of the slowest cooling rate. The peak stress is reduced from 262 MPa in slab #4 to 74 MPa in slab #6. For all three slabs, the residual stresses at the top edge center are compressive and the largest value of -256 MPa is obtained for slab #6.

The slab position of a slab directly affects the bowing deformation during slab cooling by changing the number of slabs above the slab. The final deformation after cooling of the three slabs is shown in Figure 4.5(c). The bowing of slab decreases with the increasing number of slabs above it. For slab #4 with 3 slabs above it, a gap size of 6.9 cm is predicted at the center of slab. The gap size is reduced to 3.7 cm for slab #5 and 0.3 cm for slab #6. Therefore, during cooling of the 9-slab stack, a reduced tensile stress and a good flatness can be achieved in the slab with 5 slabs above it. For slab at higher position, cooling rate and tensile stress increases and bowing of slab could occur.

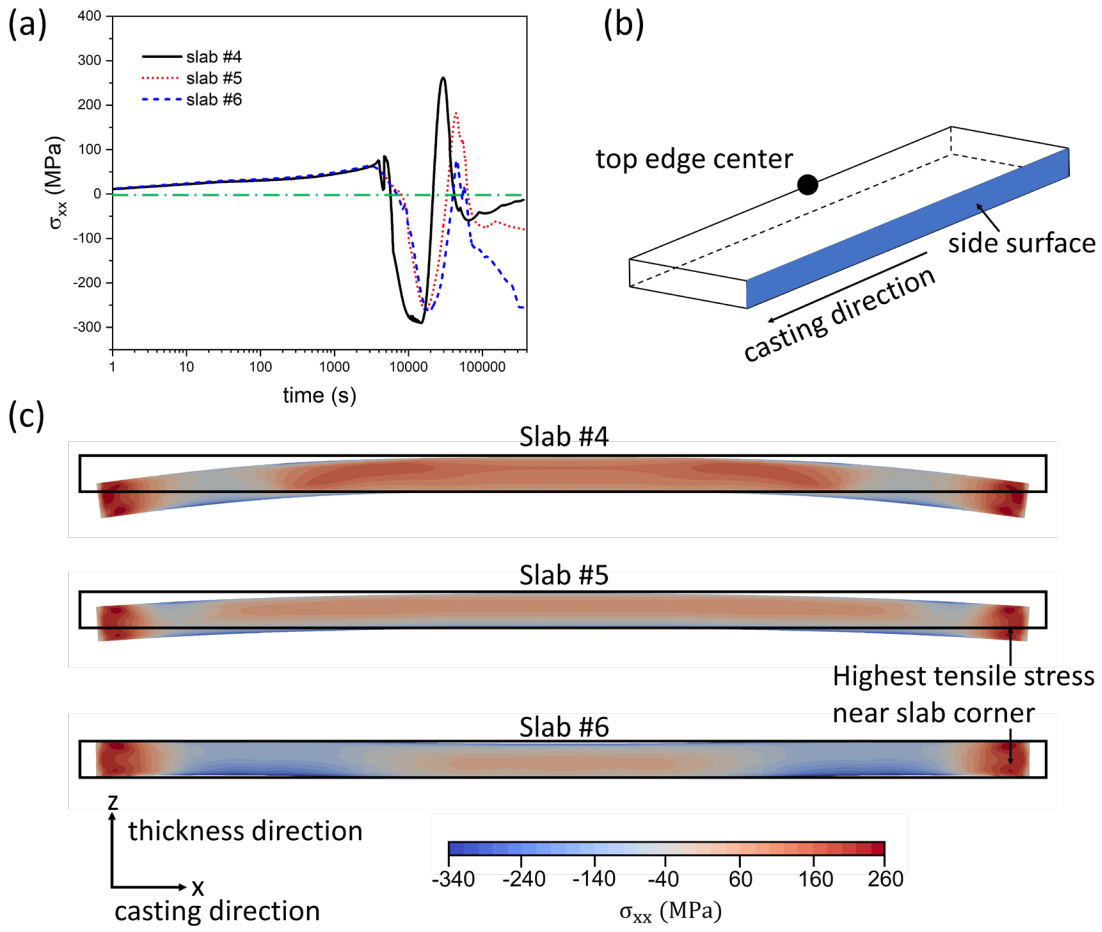

Figure 4.5. (a) Development of longitudinal stress σ_{xx} at the top edge center of the three slabs (slab #4, #5, #6) at different positions of the 9-slab stack; (b) schematic of a slab showing the location of top edge center and the side surface; (c) deformation of slabs after cooling viewing from the width direction at the side surface. The black outline indicates the original shape of the slab before cooling. The deformation is scaled up with a factor of 3. The contour plots show the distribution of residual stress σ_{xx} at the side surface for each slab.

4.2.3 Slow cooling of stacked slabs

The effect of slow cooling rate achieved by covering the slab with thermal shield or hood is discussed in Chapter 3 for the cooling of a single slab. In practice, a reduction of 50% heat loss can be obtained by applying a thermal shield. However, it appears that the cooling rate resulted from 50% heat loss is not sufficient to change the stress development. According to the results for the cooling of a 9-slab stack, slab stacking can effectively slow the cooling rate and reduce the tensile stress developed during cooling. Therefore, by combining the thermal shield method with slab stacking, a slower cooling rate that is feasible in practice can be achieved. A test case for a 9-slab stack is modeled setting the heat loss at the slab surface as 50% of those calculated in the original case to represent the effect of a thermal shield.

The cooling curves and phase evolutions at the center of the top surface of slab are shown in Figure 4.6. A slower cooling rate is observed for the test case with thermal shield applied. The phase evolutions shown that the slower cooling rate effectively reduced the amount of bainite but the increment in ferrite formation is quite small. This is because the amount of ferrite formed here is already close to the maximum amount of proeutectoid that could form during cooling. Therefore, with slower cooling rate, more austenite transforms to pearlite instead of bainite.

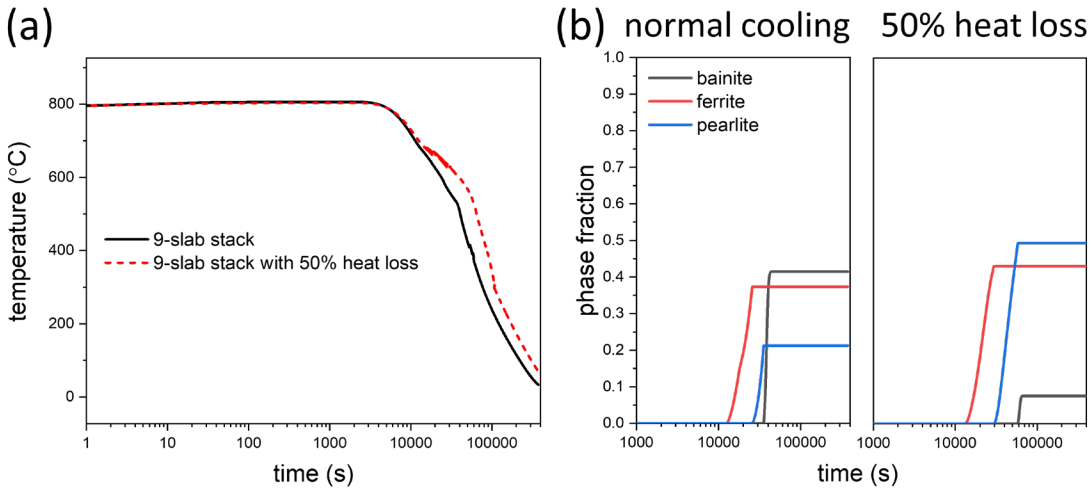

Figure 4.6. (a) Temperature histories and (b) phase evolutions at the top surface of slab for the slow cooling test case of the 9-slab stack with 50% heat loss. The results are compared to the normal cooling case of the 9-slab stack.

The slow cooling rate achieved by the combination of slab stacking and thermal shield shows significant effect on the stress development during cooling. As illustrated in Figure 4.7(a), the stress development of the stacked slab cooled with 50% heat loss shows much lower tensile stress and even compressive stress during cooling. During the initial stage of cooling, the peak tensile stress is 50 MPa due to the thermal strain with no phase transformation. The longitudinal stress σ_{xx} at the edge of slab stays in the compressive state and finally leads to a compressive residual stress of -320 MPa after cooling.

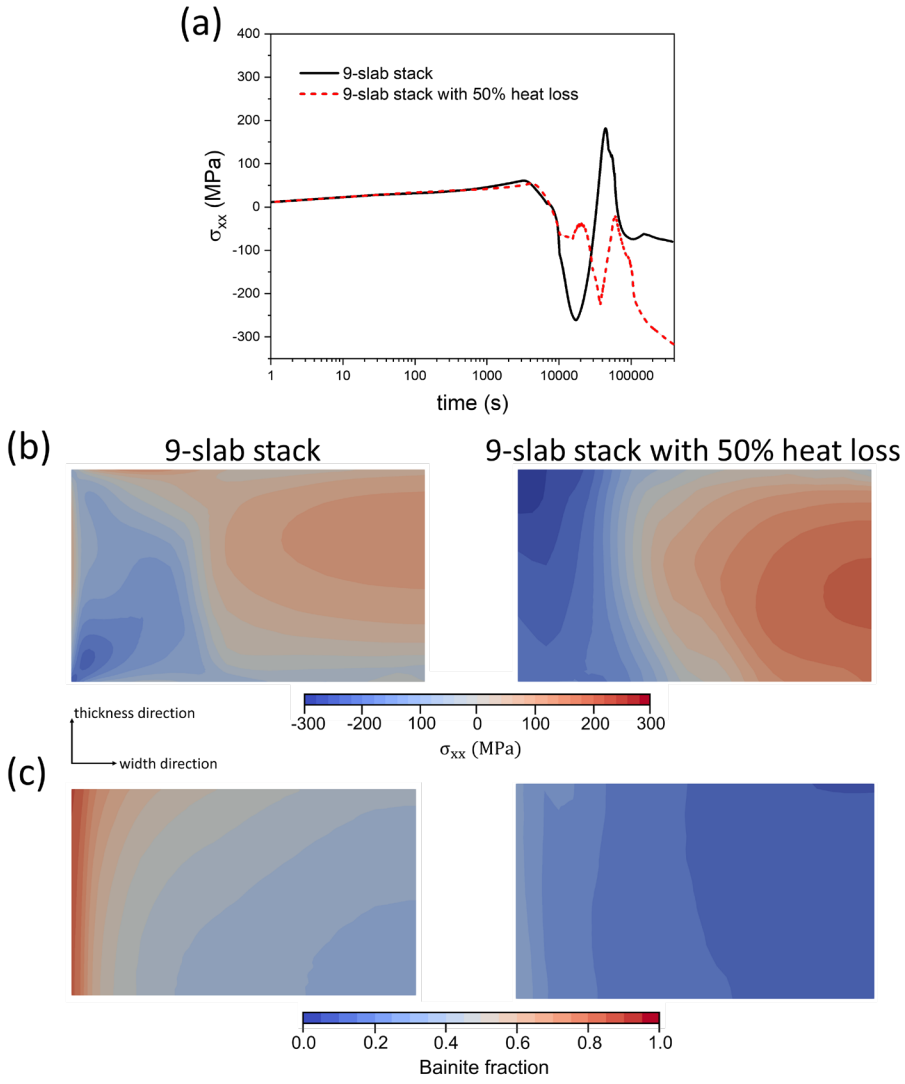

Figure 4.7. (a) Development of longitudinal stress σ_{xx} in casting direction at the top edge center of slab; (b) distribution of residual stress σ_{xx} and (c) bainite distribution at the transverse section for the 9-slab stack cooled under normal cooling condition and with 50% heat loss.

4.3 Summary

The cooling process of stacks with multiple slabs are investigated using the thermomechanical model with modified boundary conditions for contact interfaces. The effect of slabs stacking on the cooling process of boron-containing steel slabs can be summarized as follows:

1. Slabs stacking results in slower cooling rates compared to single slab air cooling as the total surface area exposed in air is reduced. More ferrite and less bainite formation are obtained after cooling of stacked slabs. The slow cooling rate leads to lower tensile stress during cooling and compressive residual stress at the edge of slab. Increasing the number of slabs in a stack helps slow the cooling rate and lower the tensile stress.
2. Slabs at different positions in a stack show different cooling behaviors. The slab at the lower level of the stack tends to have a slower cooling rate and a reduced peak tensile stress at slab edge during cooling. The slab bowing defect can also be avoided by cooling the slab with 5 slabs above it in 9-slab stack.
3. By combining slab stacking with thermal shield, cooling rate of a slab can be further reduced to affect the stress development during cooling. Applying a thermal shield on a 9-slab stack can produce a cooling rate that is sufficiently slow to lower the stress and also feasible in practice.

5. INVESTIGATION OF THE RUNOUT TABLE COOLING FOR HOT ROLLED STEEL STRIPS

Continuously-cast steel slabs are hot rolled to produce strip products. After reheating to fully austenite microstructure and a series of rolling, the strips are transported on the runout table to the down coiler and subjected to water quenching from multiple rows of water jets. The final qualities of strip products, including the mechanical and metallurgical properties, the flatness, and the residual stress state are directly associated with the cooling process. In this chapter, numerical studies are performed for the runout table cooling process of hot rolled steel strips. Compared to the air cooling of steel slabs, the thermomechanical model is applied to a similar but different process. As described in Chapter 3, boron addition in steel affects the stress development during the air cooling of slabs in the slab yard because it affects the austenite decomposition by delaying the formation of ferrite and resulting in more bainite formation. For the runout table cooling, the influence of boron addition is also affected by the fast cooling rate from water quenching and the relatively short duration of cooling. Different cooling conditions should be applied for steel strips with and without boron addition regarding the difference in phase transformation. The objective of this chapter is to investigate cooling strategies influencing temperature history, phase transformation, and stress development of boron-containing and non-boron steel strips. Numerical simulations with the same cooling conditions are first performed for both steel grades. The cooling curve, stress development and phase evolution are examined for each case. Parametric studies are performed to study the importance of different cooling parameters and find appropriate cooling strategies.

5.1 Model setup for the runout table cooling of strips

5.1.1 Geometry and initial conditions

The length of a typical runout table ranges from 50 to 100 m. A model covering the full length will be inefficient and cost a long computational time. Therefore, a segment of the strip is chosen for simulation. As the strip is transported on the runout table, the chosen segment passes through the water quenching zone with multiple rows of cooling jets. The geometry and mesh of the strip segment is shown in Figure 5.1 with a dimension of 2 m in length, 1.5 m in width, and 5

mm in thickness. Due to the symmetry condition across the width of strip, half of the strip volume is modeled. The mesh contains a total of 25,000 hexahedral cells with a uniform cell size of $2\times3\times0.05$ cm.

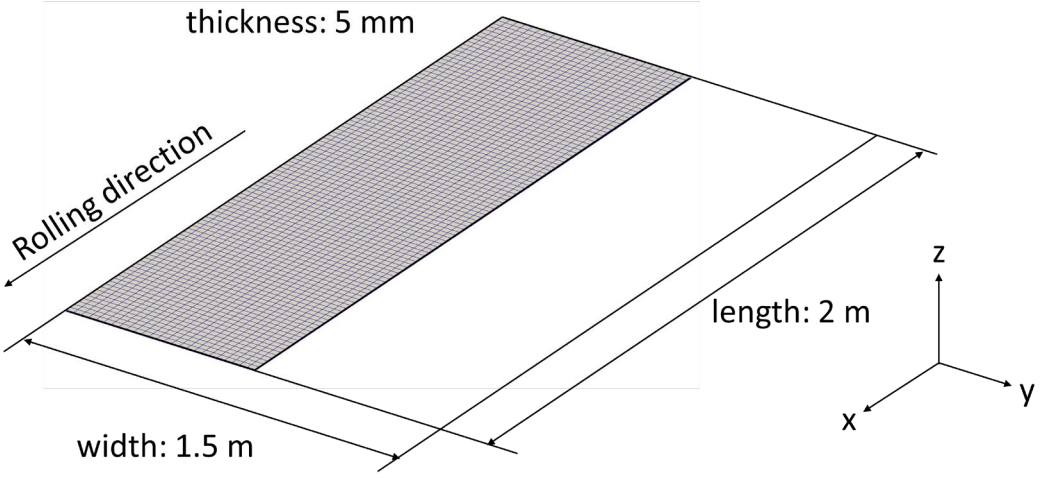

Figure 5.1. Geometry and mesh of the strip segment used for the runout table cooling simulation. The numerical domain is half of the segment due to symmetry condition.

In conventional hot rolling mill, steel strips leave the last stand finishing mill with a temperature ranging from 800 to 950 ℃. The initial temperature of the strip at the beginning of runout table is assumed to be uniform at 830 ℃. A fully austenitic microstructure is assumed across the entire strip segment.

5.1.2 Boundary conditions

During the runout table cooling process, the strip is moving with a constant velocity passing through the stationary water quenching zone. The typical strip speed ranges from 2 to 20 m/s[94]. To implement the cooling process in the model, the strip is assumed to be static, and time dependent thermal boundary conditions are applied to represent the strip movement. The structure of the runout table used for the test cases is shown in Figure 5.2. The total length between the finishing mill and the down coiler is 110 m. The strip speed is set as 5 m/s. After exiting the finishing mill, the strip first passes through the entry air cooling zone with a length of $L_1 = 10$ m. It then enters the water quenching zone with multiple rows of top and bottom cooling jets with a length of $L_2 = 90$ m. There are a total of 50 rows of jets on both sides of the strip with a distance

of $\Delta l = 1.8$ m between each row. Finally, it leaves the water quenching zone and goes through the exit air cooling zone with a length of $L_3 = 10$ m before coiling. For the air cooling zones, the thermal boundary condition is set as radiation with the emissivity as 0.7 and ambient temperature as 20 ℃. Because the typical strip temperature for steel during runout table cooling is higher than 500 ℃, the heat extraction from forced air convection is ignored here due to its small value compared to radiation[49].

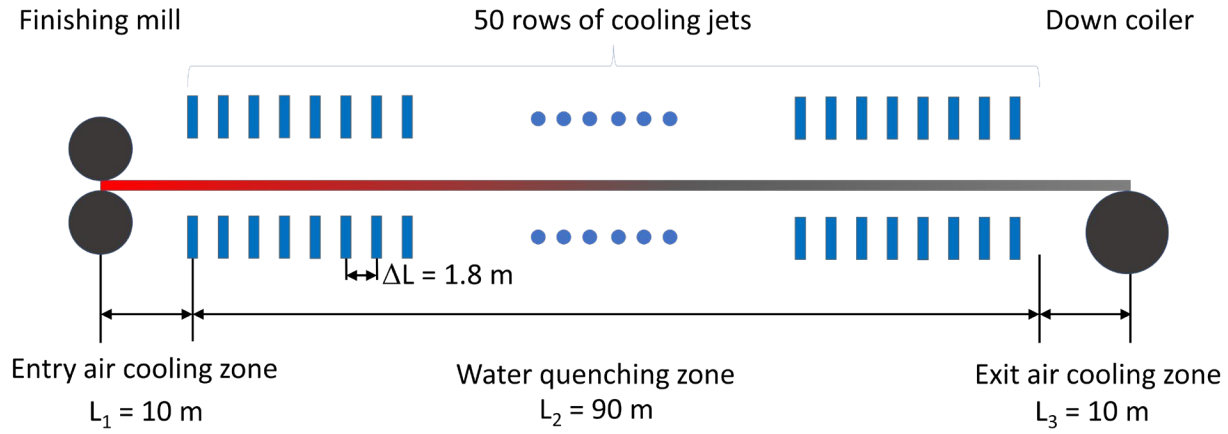

Figure 5.2. Schematic of the runout table with dimensions.

The thermal boundary conditions for top and bottom strip surface inside the water quenching zone are illustrated in Figure 5.3. The cooling system is considered as planar where the cooling condition is uniform across the transverse direction of strip. For simplicity concern, two assumptions are made about the impingement and parallel flow zone. The first one is that there is no air cooling zone between two active rows of cooling jets on the top surface. Thus, the top surface is divided into impingement zones and parallel water flow zones. The bottom surface is divided into impingement zones and air cooling zones. The second assumption is that the impingement zone is symmetrical with respect to the centerline of cooling jet. The length of the impingement zone, l, is proportional to the nozzle diameter, d, with a ratio r. According to Hall et al[95], a typical length of the impingement zone is expressed as $l = 4d$. Therefore, the impingement zone length is set as 4 cm in the test case with the nozzle diameter of 1 cm.

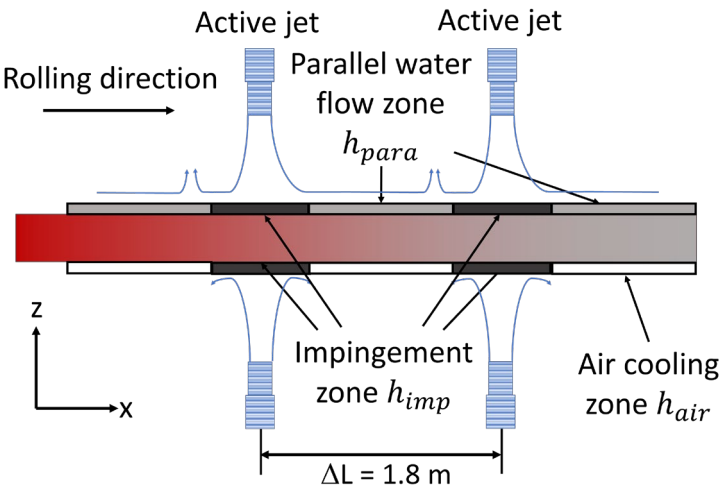

Figure 5.3. Thermal boundary conditions in the water quenching zone during runout table cooling.

Different correlations listed in Table 5.1 are used to determine the heat transfer coefficients for each cooling zone. The empirical correlations adopted in this study show that the heat transfer coefficient for water quenching zone increases with decreasing strip surface temperature, which agrees with experimental results found by several researchers[96–98]. Because the thickness of the strip is much smaller than its width and length, heat extraction at side surfaces of the strip is neglected. Therefore, thermal boundary conditions for the side surfaces of the strip are set as adiabatic with zero thermal gradient.

Table 5.1. Heat transfer coefficients (in $W/m^2°C$) in the water quenching zone[45,55,57,59].

Top surface	
Impingement zone	$h_{imp,top} = 4h_{para}$
Parallel water flow zone	$h_{para} = 200 \times \frac{2420 - 21.7T_w}{(T-100)^{0.8}}$
Bottom surface	
Impingement zone	$h_{imp,bottom} = 0.35h_{imp,top}$
Air cooling zone	$h_{air} = h_{rad}$

Note: Surface temperature T and cooling water temperature T_w are in °C.

For the mechanical boundary conditions, full displacement constraint is applied for the trailing end of the strip segment to prevent rigid body motion. Other surfaces are set as free surface without traction force.

5.2 Results and discussion

5.2.1 Effect of boron on the runout table cooling of steel strips

The runout table cooling process for steel strips with and without boron is simulated with the same cooling conditions and process parameters. The strip velocity is 5 m/s and it takes 22 s for the strip segment to complete the runout table cooling. The cooling curves at different positions of strips are shown in Figure 5.4(a) for both grades of steel. At the first 10 m, both strips are in the entry air cooling zone with a slow cooling rate. Due to the small thickness of strip and the low heat transfer coefficient for air cooling, the Biot number is estimated to be around 0.01 and thus the temperature distribution across strip thickness is quite uniform. Once the strips enter the water quenching zone, the temperature drops drastically at surface of strips and a large thermal gradient is observed across thickness. Serrations are found for cooling curves at top and bottom surfaces of both strips. In the impingement region, the intensive water cooling results in the highest local heat flux, and the surface temperature drops significantly. When moved into the parallel flow zone for top surface or air cooling zone for bottom surface, surface temperature abruptly rises up due to the heat conduction from the interior of strip. The top surface shows the lowest temperature because it is cooled with both jet impingement and parallel water flow. Since the bottom surface is cooled by jet impingement and air cooling, the difference between temperatures at bottom surface and strip center is small. Under the same cooling condition, two strips show identical cooling curves at the first 60 m of runout table since 0.003 wt.% of boron addition causes little difference in thermal properties of steel. However, the effect of boron becomes significant as cooling proceeds and phase transformation occurs. For the steel without B, although the fast cooling rate of water quenching prevents the formation of ferrite and pearlite, bainite starts to form when temperature drops below 500 °C. The latent heat released as austenite transforms to bainite results in a slower cooling rate for steel strips without B. For the steel with B, all of the diffusion-controlled phase transformations are delayed and will not occur during the short time period on the runout table according to the TTT diagram in Figure 1.3. At the exit of the water quenching zone, the top

surface temperature of the steel strip with B is 140 ℃ lower than that of the steel without B. In the exit air cooling zone, the temperatures at top surface quickly recover to the central temperature and uniform temperature distributions are achieved for both cases at the end of the runout table. Due to the effect of boron, the final coiling temperatures are 480 and 356 ℃ for strip without and with B, respectively.

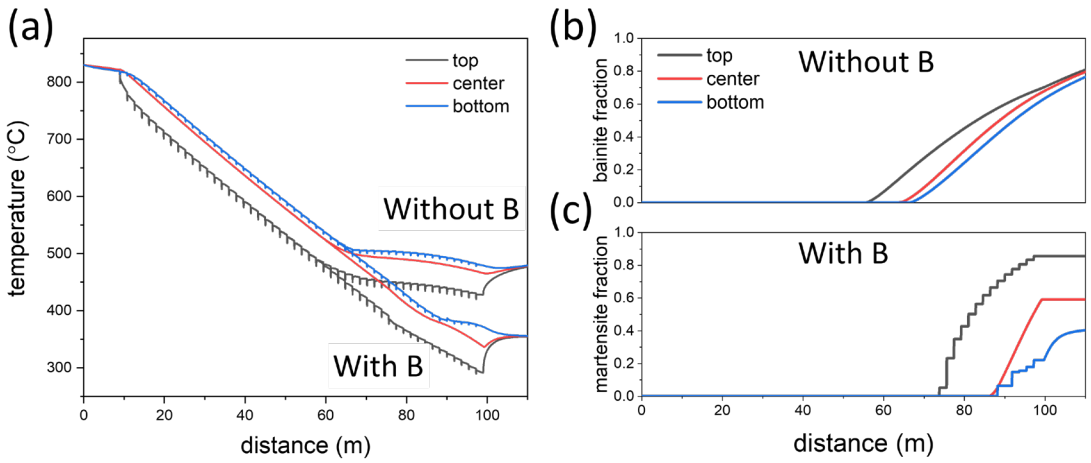

Figure 5.4. Predicted (a) temperature profiles at different positions of steel strips during runout table cooling; (b) and (c) are the phase evolutions of bainite and martensite for steel without and with B, respectively.

The phase evolutions during the runout table cooling for both strips at various positions are shown in Figure 5.4(b) and (c). For the steel without B, bainite starts to form at the top surface during cooling and an almost uniform phase distribution of 78% bainite is observed at the coiling temperature. The fast cooling rate for the steel with B results in martensite formation and the final distribution is not uniform. Since martensite transformation is directly related to temperature, top surface of the strip with the lowest minimum temperature consists of the most martensite, which is twice the fraction for the bottom surface. The Austenite transformation is not completed for both cases, and it will continue when the strips are further cooled as coils.

Based on the significant influence of boron addition on the temperature history and phase evolutions, the difference in stress development for the two strips are expected. The development of transverse stress σ_{yy} at the strips surfaces and center are presented in Figure 5.5. Like the serration found in temperature curves for strip surfaces, evident serrations are also found in stress development curves. When a certain point on the surfaces is directly under jet impingement

cooling, the fast drop in temperature will cause thermal strain as contraction and result in increment in stress. Once the point passes the impingement zone, temperature recovers quickly with thermal expansion and stress decreases correspondingly. At the center of strip thickness where the temperature change is less drastically, the serration becomes less obvious. For both strips, stress developments are identical before phase transformation, and the thermal stresses stay at a relatively low level with a magnitude less than 100 MPa even at the top surface with fastest cooling rate. Peak value of stress is always found during phase transformation. The martensitic transformation for the steel with B induces the highest peak tensile stress of 403 MPa at the top surface. The non-uniform martensite distribution also contributes to the residual stress after cooling. Compared to the steel with B, the stress induced by bainite formation is less significant and the peak tensile stress remains below 200 MPa across the strip.

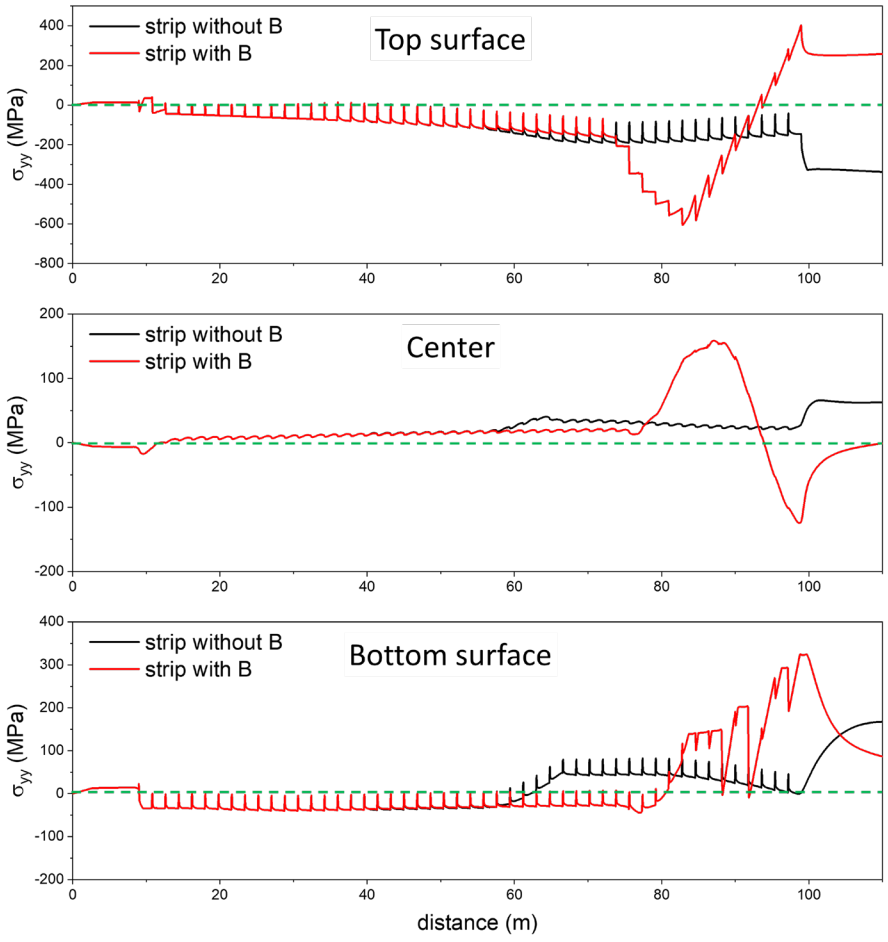

Figure 5.5. Development of transverse stress σ_{yy} at the top, bottom surfaces and center of strips with and without B. The evident serration in the curves for the top and bottom surface is due to the temperature drop and recovery caused by jet impingement.

5.2.2 Cooling strategy for boron-containing steel strips

Comparison of the runout table cooling process between the two grades of steel under the same cooling condition shows that the boron-containing steel strip exhibits totally different cooling curve, phase evolution, and stress development, despite the low level of boron addition. The appropriate cooling condition for the non-boron steel can cause problems such as large residual stresses and non-uniform phase distributions for the runout table cooling of boron-containing steel. The fast cooling rate results in low coiling temperature and martensite formation. The strip products of boron-containing steel used for press hardening are usually produced with a ferritic-pearlitic microstructure via slow cooling. If the strips leave the runout table with a fully austenitic microstructure, a slower cooling rate can be achieved during the air cooling of the coil. Therefore, adjusting the cooling strategy on the runout table is necessary in controlling the microstructure and reduce residual stresses.

As described in previous section, the water quenching zone of the runout table consists of 50 rows of cooling jets for both sides of the strip. The easiest way to adjust the cooling strategy is to reduce the length of the water quenching zone by shutting down some of the cooling jets. Therefore, a test case with only the first 30 rows of jets being active is performed. The length of water quenching zone is adjusted to 54 m with other cooling conditions remain unchanged. The simulation results are shown in Figure 5.6. The cooling curves in Figure 5.6(a) indicates the increment of coiling temperature after adjustment. The strip exits the water-quenching zone at 64 m and is then subjected to air cooling for the rest section of the runout table. The resultant coiling temperature is 490 ℃, which is higher than the martensite starting temperature T_{M_S} (382 ℃). Therefore, a fully austenitic microstructure is predicted after runout table cooling. Without phase transformation strain from martensite, the stress is only affected by thermal strain. The reduction of stress level is found at all three positions showed in Figure 5.6. The highest tensile stress is observed on the bottom surface of strip, and it is less than 80 MPa. Therefore, the steel strip with B ends up with a uniform microstructure of austenite and low residual stress by effectively adjusting the cooling strategy.

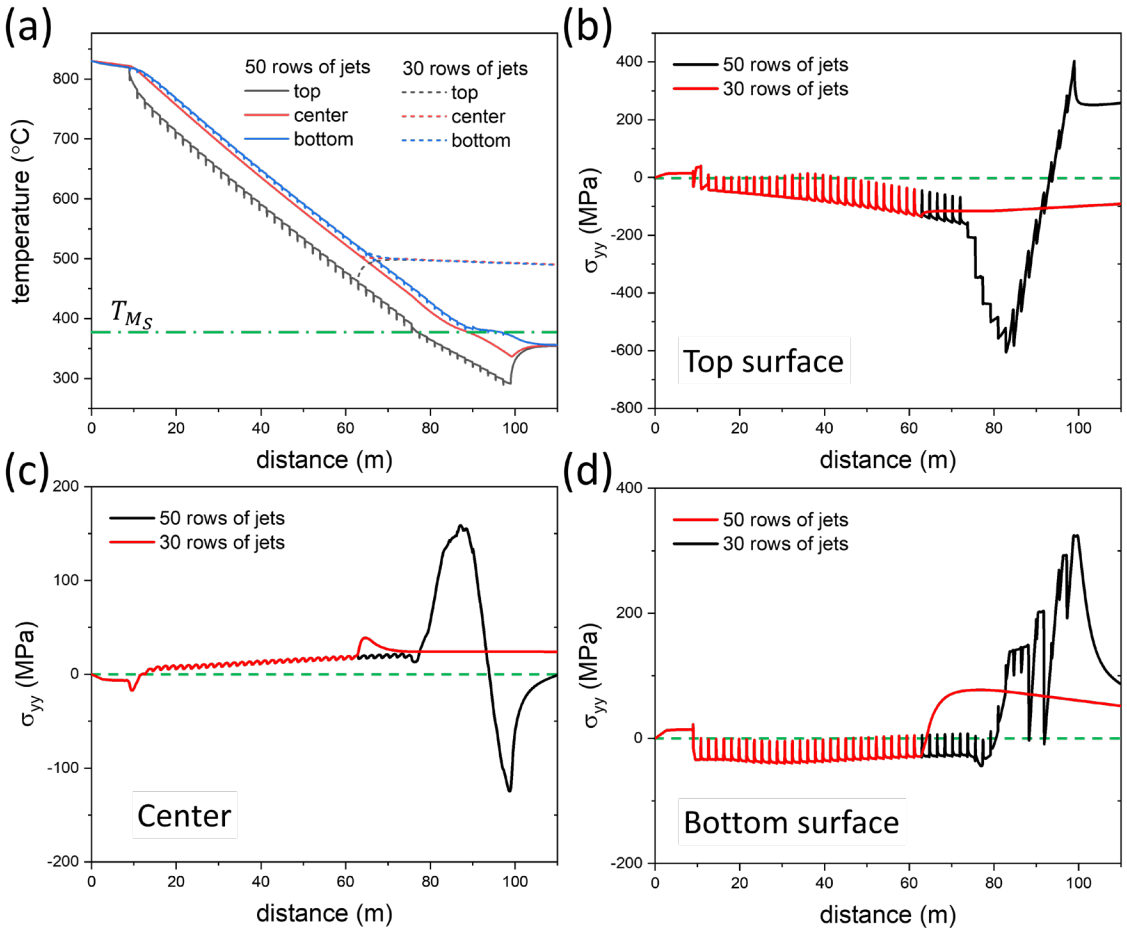

Figure 5.6. (a) Temperature profile and stress development at (b) top, (c) center, and (d) bottom of the strip during runout table cooling with the first 30 rows of cooling jets activated. Predicted coiling temperature is increased and stress levels are reduced.

5.3 Summary

The runout table cooling for steel strips after hot rolling is investigated numerically with the thermomechanical model. The movement of strip is achieved by applying the time dependent thermal boundary conditions. The following conclusions can be drawn from the results of numerical study:

1. During the runout table cooling with fast cooling rate, the addition of boron prevents the diffusion-controlled phase transformations from austenite and results in martensite formation. Under the same cooling conditions, the non-boron steel strip shows a uniform

phase distribution of austenite and bainite before coiling. The boron-containing steel strip exhibits a lower coiling temperature and non-uniform martensite distribution.

2. Due to the fast cooling rate and martensite formation, higher level of stress is developed during cooling of the boron-containing steel strip in comparison with the non-boron steel. Tensile residual stress is found at both sides of the boron-containing strip.
3. The runout table cooling for boron-containing strips can be effectively adjusted to slow the cooling rate. With reduced a water-quenching zone by deactivating multiple rows of cooling jets, a uniform microstructure of austenite with lower residual stress can be achieved for boron-containing strips.

6. CONCLUSIONS AND FUTURE WORK

6.1 Conclusions

Boron addition to steel improves its hardenability, but also causes post-casting problems such as cracking defects in continuously-cast steel slabs after cooling. The purpose of this work was to investigate the cooling process of continuously-cast boron-containing steel with an emphasis on stress development and phase evolution. Because of the difficulties in monitoring the interacting heat transfer, phase transformation, and stress development, a 3D thermomechanical finite volume model was developed to numerically simulate the cooling process. The model was established by coupling the physical phenomena (thermal, metallurgical, and mechanical) that occurs during cooling of steel. The formulation of phase transformation during cooling of steel based on transformation kinetics was developed and validated. The interactions among phase transformation, heat transfer, and stress calculation are achieved through latent heat release, thermal strain, and transformation strain. Beyond the scope of cooling process of steel, this model has an importance to the finite volume solid mechanics community as it includes solid-solid phase transformation to thermomechanical modelling using finite volume method.

The model was used to investigate the role of boron addition on the stress development and phase evolution of steel during cooling process, specifically in the air cooling of continuously-cast steel slabs and the runout table cooling of steel strips. For the air cooling of a single steel slab, due to the change in phase transformation behaviors by boron addition, the boron-containing slab consists of mostly bainite, while the non-boron slab shows a ferritic-pearlitic microstructure. At the edge of slab where post-casting defects such as transverse corner cracks might occur, higher tensile stress and plastic strain were predicted for the boron-containing steel. The high stress can be reduced by adjusting the cooling condition to achieve a slower cooling rate. Less bainite formation, lower stresses, and smaller plastic strain can be achieved with the cooling rate below a certain level. As a method to slow down the cooling rate and preventing slab bowing defects, multiple slabs stacking has been adopted for air cooling of slabs. It was determined that cooling rates is slower in stacked slab, and it leads to lower tensile stress during cooling and compressive residual stress at the edge of slab. For slabs at lower level in a 9-slab stack, slabs stacking can effectively inhibit the slab bowing defect. In the runout table cooling of strips, the suppression of

diffusion-controlled transformation owing to boron addition in boron-containing steel results in non-uniform martensite distribution across strip thickness and high residual stresses, which is detrimental to strip quality. Adjusting the cooling strategy by deactivating multiple rows of cooling jets reduces residual stresses and improves microstructure homogeneity. These studies indicate that it is beneficial for cooling process of boron-containing steel to slow down the cooling rate in practice for both air cooling of slabs and runout table cooling of strips.

6.2 Recommendations for future work

The thermomechanical model developed and implemented in this work has demonstrated that it can be applied to numerical studies of cooling processes of steels with different phase transformation behaviors. In addition to the air cooling of slabs and runout table cooling of strips, the model can be used in cooling of coils after hot rolling and quenching in a press die for press hardening process. The coil cooling can be treated as a subsequent process of the runout table cooling of strips and no additional modification to the model is needed. However, for the die quenching in press hardening process, the model is not sufficient in plasticity calculation as such case requires large deformation. Currently, the model assumes small strain for deformation which means the geometry change due to displacement is neglected. Future work on model development should be focused on updating the change in the size and shape of control volumes at each step based on previous deformation and displacement calculation. As large deformation could cause sever distortion of cells which leads to poor mesh quality and convergence, remeshing approaches might also be implemented.

The application can be expanded to other alloys with solid-solid phase transformation during cooling such as titanium alloys. As demonstrated by Charles[99], titanium alloy Ti-6Al-4V exhibits a similar TTT diagram as steel with diffusion-controlled transformation and martensitic transformation. Therefore, the model can be used for titanium alloys with different input transformation kinetics obtained from their TTT diagram. Currently, the input kinetics are manually calculated based on TTT diagram from software such as JMatPro and Thermo-Calc. Therefore, future work on coupling the model with TTT data from these software directly could be helpful.

REFERENCES

[1] S. Keeler, M. Kimchi, P.J. Mooney, Advanced High-Strength Steels Guidelines Version 6.0, WorldAutoSteel. (2017) 10–12.

[2] H. So, D. Faßmann, H. Hoffmann, R. Golle, M. Schaper, An investigation of the blanking process of the quenchable boron alloyed steel 22MnB5 before and after hot stamping process, Journal of Materials Processing Technology. 212 (2012) 437–449. https://doi.org/10.1016/j.jmatprotec.2011.10.006.

[3] H. Karbasian, A.E. Tekkaya, A review on hot stamping, Journal of Materials Processing Technology. 210 (2010) 2103–2118. https://doi.org/10.1016/j.jmatprotec.2010.07.019.

[4] E.J. Seo, L. Cho, B.C. de Cooman, Application of Quenching and Partitioning (Q&P) Processing to Press Hardening Steel, Metallurgical and Materials Transactions A. 45 (2014) 4022–4037. https://doi.org/10.1007/s11661-014-2316-z.

[5] G. Krauss, Steels: processing, structure, and performance, ASM International. (2015) 363.

[6] H. SUN, Application of Hot Forming High Strength Steel Parts on Car Body in Side Impact, Chinese Journal of Mechanical Engineering. 23 (2010) 252. https://doi.org/10.3901/CJME.2010.02.252.

[7] K. Luitjohan, M. Krane, D. Johnson, Effect of Solute Elements on Boron Segregation in Boron-Containing Steels, ISIJ International. 60 (2020) 92–98. https://doi.org/10.2355/isijinternational.ISIJINT-2019-258.

[8] M.S. Khan, M.H. Razmpoosh, E. Biro, Y. Zhou, A review on the laser welding of coated 22MnB5 press-hardened steel and its impact on the production of tailor-welded blanks, Science and Technology of Welding and Joining. 25 (2020) 447–467. https://doi.org/10.1080/13621718.2020.1742472.

[9] H. Yin, K. Blazek, O. Lanzi, “In-situ” Observation of Remelting Phenomenon after Solidification of Fe–B Alloy and B-bearing Commercial Steels, ISIJ International. 49 (2009) 1561–1567. https://doi.org/10.2355/isijinternational.49.1561.

[10] J. Sun, H. Zhu, W. Wang, Y. Duan, Effect of boron segregation on the surface crack of low carbon boron-bearing steel, Results in Physics. 13 (2019) 102153. https://doi.org/10.1016/j.rinp.2019.02.089.

[11] S. Louhenkilpi, Continuous Casting of Steel, in: Treatise on Process Metallurgy, Elsevier, 2014: pp. 373–434. https://doi.org/10.1016/B978-0-08-096988-6.00007-9.

[12] X. Huang, B.G. Thomas, Modeling of steel grade transition in continuous slab casting processes, Metallurgical Transactions B. 24 (1993) 379–393. https://doi.org/10.1007/BF02659140.

[13] J.K. Brimacombe, K. Sorimachi, Crack formation in the continuous casting of steel, Metallurgical Transactions B. 8 (1977) 489–505. https://doi.org/10.1007/BF02696937.

[14] K.-E. Blazek, O. Lanzi, H. Yin, Boron effects on the solidification of steel during continuous casting, Revue de Métallurgie. 105 (2008) 609–625. https://doi.org/10.1051/metal:2009005.

[15] K.E. Luitjohan, M.J.M. Krane, V. Ortalan, D.R. Johnson, Investigation of the metatectic reaction in iron-boron binary alloys, Journal of Alloys and Compounds. 732 (2018) 498–505. https://doi.org/10.1016/j.jallcom.2017.10.238.

[16] F. Zarandi, S. Yue, The Effect of Boron on Hot Ductility of Nb-microalloyed Steels, ISIJ International. 46 (2006) 591–598. https://doi.org/10.2355/isijinternational.46.591.

[17] S.K. Kim, N.J. Kim, J.S. Kim, Effect of boron on the hot ductility of Nb-containing steel, Metallurgical and Materials Transactions A. 33 (2002) 701–704. https://doi.org/10.1007/s11661-002-0133-2.

[18] E. López-Chipres, I. Mejía, C. Maldonado, A. Bedolla-Jacuinde, J.M. Cabrera, Hot ductility behavior of boron microalloyed steels, Materials Science and Engineering: A. 460–461 (2007) 464–470. https://doi.org/10.1016/j.msea.2007.01.098.

[19] P. Zhao, Y. Zhang, Effect of boron on hot ductility oflow carbon low alloyed steel, Materials Science and Technology. 17 (2001) 843–846. https://doi.org/10.1179/026708301101510627.

[20] K.C. Cho, D.J. Mun, J.Y. Kim, J.K. Park, J.S. Lee, Y.M. Koo, Effect of Boron Precipitation Behavior on the Hot Ductility of Boron Containing Steel, Metallurgical and Materials Transactions A. 41 (2010) 1421–1428. https://doi.org/10.1007/s11661-010-0211-9.

[21] K.C. Cho, D.J. Mun, Y.M. Koo, J.S. Lee, Effect of niobium and titanium addition on the hot ductility of boron containing steel, Materials Science and Engineering: A. 528 (2011) 3556–3561. https://doi.org/10.1016/j.msea.2011.01.097.

[22] K. Taguchi, S. Takaya, M. Numata, T. Kato, Effect of Deoxidizing Element on the Hot Ductility of Boron-Containing Steel, ISIJ International. 60 (2020) 2829–2837. https://doi.org/10.2355/isijinternational.ISIJINT-2020-192.

[23] L.H. Chown, L.A. Cornish, Investigation of hot ductility in Al-killed boron steels, Materials Science and Engineering: A. 494 (2008) 263–275. https://doi.org/10.1016/j.msea.2008.04.026.

[24] A. Grill, J.K. Brimacombe, F. Weinberg, Mathematical analysis of stresses in continuous casting of steel, Ironmaking and Steelmaking. 3 (1976) 38–47.

[25] K. Sorimachi, J.K. Brimacombe, Improvements in mathematical modelling of stresses in continuous casting of steel, Ironmaking and Steelmaking. 4 (1977) 240–245.

[26] B.G. Thomas, Modeling of the continuous casting of steel—past, present, and future, Metallurgical and Materials Transactions B. 33 (2002) 795–812. https://doi.org/10.1007/s11663-002-0063-9.

[27] J. Sengupta, B.G. Thomas, M.A. Wells, The use of water cooling during the continuous casting of steel and aluminum alloys, Metallurgical and Materials Transactions A. 36 (2005) 187–204. https://doi.org/10.1007/s11661-005-0151-y.

[28] A. Grill, K. Sorimachi, J.K. Brimacombe, Heat flow, gap formation and break-outs in the continuous casting of steel slabs, Metallurgical Transactions B. 7 (1976) 177–189. https://doi.org/10.1007/BF02654916.

[29] S. Koric, L.C. Hibbeler, R. Liu, B.G. Thomas, Multiphysics Model of Metal Solidification on the Continuum Level, Numerical Heat Transfer, Part B: Fundamentals. 58 (2010) 371–392. https://doi.org/10.1080/10407790.2011.540954.

[30] J.-E. Lee, T.-J. Yeo, K. Hwan OH, J.-K. Yoon, U.-S. Yoon, Prediction of cracks in continuously cast steel beam blank through fully coupled analysis of fluid flow, heat transfer, and deformation behavior of a solidifying shell, Metallurgical and Materials Transactions A. 31 (2000) 225–237. https://doi.org/10.1007/s11661-000-0067-5.

[31] W. Chen, Y.Z. Zhang, C.J. Zhang, L.G. Zhu, W.G. Lu, B.X. Wang, J.H. Ma, Thermo-mechanical simulation and parameters optimization for beam blank continuous casting, Materials Science and Engineering: A. 499 (2009) 58–63. https://doi.org/10.1016/j.msea.2007.11.116.

[32] M. Janik, H. Dyja, S. Berski, G. Banaszek, Two-dimensional thermomechanical analysis of continuous casting process, Journal of Materials Processing Technology. 153–154 (2004) 578–582. https://doi.org/10.1016/j.jmatprotec.2004.04.129.

[33] M. Bellet, A. Heinrich, A Two-dimensional Finite Element Thermomechanical Approach to a Global Stress-Strain Analysis of Steel Continuous Casting, ISIJ International. 44 (2004) 1686–1695. https://doi.org/10.2355/isijinternational.44.1686.

[34] S. Yu, M. Long, Q. Wang, D. Chen, P. Xu, H. Duan, S. Wu, Effect of the strand corner structure on the corner stress during the bending and straightening processes in slab continuous casting, Journal of Manufacturing Processes. 48 (2019) 270–282. https://doi.org/10.1016/j.jmapro.2019.10.032.

[35] C. Şimşir, C.H. Gür, A FEM based framework for simulation of thermal treatments: Application to steel quenching, Computational Materials Science. 44 (2008) 588–600. https://doi.org/10.1016/j.commatsci.2008.04.021.

[36] T. Inoue, K. Tanaka, An elastic-plastic stress analysis of quenching when considering a transformation, International Journal of Mechanical Sciences. 17 (1975) 361–367. https://doi.org/10.1016/0020-7403(75)90028-4.

[37] S. Denis, E. Gautier, A. Simon, G. Beck, Stress–phase-transformation interactions – basic principles, modelling, and calculation of internal stresses, Materials Science and Technology. 1 (1985) 805–814. https://doi.org/10.1179/mst.1985.1.10.805.

[38] , C. Hakan Gür, , A. Erman Tekkaya, Numerical and experimental analysis of quench induced stresses and microstructures, Journal of the Mechanical Behavior of Materials. 9 (1998) 237–256. https://doi.org/10.1515/JMBM.1998.9.4.237.

[39] C.H. Gür, A.E. Tekkaya, Numerical investigation of non-homogeneous plastic deformation in quenching process, Materials Science and Engineering: A. 319–321 (2001) 164–169. https://doi.org/10.1016/S0921-5093(01)01064-4.

[40] C. Şimşir, C.H. Gür, 3D FEM simulation of steel quenching and investigation of the effect of asymmetric geometry on residual stress distribution, Journal of Materials Processing Technology. 207 (2008) 211–221. https://doi.org/10.1016/j.jmatprotec.2007.12.074.

[41] M.R. Allazadeh, C.I. Garcia, FEM technique to study residual stresses developed in continuously cast steel during solid–solid phase transformation, Ironmaking & Steelmaking. 38 (2011) 566–576. https://doi.org/10.1179/1743281211Y.0000000046.

[42] P. Wikström, C. Nilsson, F. Berntsson, Thermomechanical modeling of cooling slabs under a hood after continuous casting, Materials Research Express. 4 (2017) 116517. https://doi.org/10.1088/2053-1591/aa9858.

[43] Z. Liu, Experiments and mathematical modelling of controlled runout table cooling in a hot rolling mill, 2001.

[44] H.-H. Cho, Y.-G. Cho, D.-W. Kim, S.-J. Kim, W.-B. Lee, H.N. Han, Finite Element Investigation for Edge Wave Prediction in Hot Rolled Steel during Run Out Table Cooling, ISIJ International. 54 (2014) 1646–1652. https://doi.org/10.2355/isijinternational.54.1646.

[45] C.G. Sun, H.N. Han, J.K. Lee, Y.S. Jin, S.M. Hwang, A Finite Element Model for the Prediction of Thermal and Metallurgical Behavior of Strip on Run-out-table in Hot Rolling., ISIJ International. 42 (2002) 392–400. https://doi.org/10.2355/isijinternational.42.392.

[46] S. Serajzadeh, Prediction of temperature distribution and phase transformation on the run-out table in the process of hot strip rolling, Applied Mathematical Modelling. 27 (2003) 861–875. https://doi.org/10.1016/S0307-904X(03)00085-4.

[47] A. Mukhopadhyay, S. Sikdar, Implementation of an on-line run-out table model in a hot strip mill, Journal of Materials Processing Technology. 169 (2005) 164–172. https://doi.org/10.1016/j.jmatprotec.2005.04.039.

[48] G. Guedia Guemo, V. Prodanovic, M. Militzer, Simulation of Runout Table Cooling, Steel Research International. 90 (2019) 1800361. https://doi.org/10.1002/srin.201800361.

[49] H.-J. Li, L.-G. Li, Y.-L. Li, G.-D. Wang, Online Monitor and Control of Cooling Temperature on Run-out Table of Hot Strip Mill, Steel Research International. 86 (2015) 1225–1233. https://doi.org/10.1002/srin.201400269.

[50] A. Faghri, Y. Zhang, BOILING, in: Transport Phenomena in Multiphase Systems, Elsevier, 2006: pp. 765–852. https://doi.org/10.1016/B978-0-12-370610-2.50015-5.

[51] I. Filipovic, F.P. Incropera, R. Viskanta, QUENCHING PHENOMENA ASSOCIATED WITH A WATER WALL JET: I. TRANSIENT HYDRODYNAMIC AND THERMAL CONDITIONS, Experimental Heat Transfer. 8 (1995) 97–117. https://doi.org/10.1080/08916159508946494.

[52] J. Filipovic, R. Viskanta, F.P. Incropera, T.A. Vesiocki, Thermal behaviour of a moving steel strip cooled by an array of planar water jets, Steel Research. 63 (1992) 438–446. https://doi.org/10.1002/srin.199201738.

[53] T.L. Bergman, A.S. Lavine, F.P. Incropera, D.P. DeWitt, Fundamentals of heat and mass transfer, USA: John Wiley & Sons. ISBN. (2015) 571–577.

[54] Z.D. Liu, D. Fraser, I.V. Samarasekera, Experimental Study and Calculation of Boiling Heat Transfer on Steel Plates During Runout Table Operation, Canadian Metallurgical Quarterly. 41 (2002) 63–74. https://doi.org/10.1179/cmq.2002.41.1.63.

[55] M.S. Gadala, F. Xu, Study on the 2-D Simulation of the Cooling Process of Steel Strips on a Run-Out Table, Numerical Heat Transfer, Part A: Applications. 58 (2010) 1–19. https://doi.org/10.1080/10407782.2010.490456.

[56] L. Ning, D. Yang, J. Lin, T.A. Dean, Effect of Laminar Cooling on Phase Transformation Evolution in Hot Rolling Process, Journal of Iron and Steel Research International. 17 (2010) 28–32. https://doi.org/10.1016/S1006-706X(10)60179-3.

[57] H.N. Han, S.H. Park, Model for cooling and phase transformation behaviour of transformation induced plasticity steel on runout table in hot strip mill, Materials Science and Technology. 17 (2001) 721–726. https://doi.org/10.1179/026708301101510447.

[58] H.N. Han, J.K. Lee, H.J. Kim, Y.-S. Jin, A model for deformation, temperature and phase transformation behavior of steels on run-out table in hot strip mill, Journal of Materials Processing Technology. 128 (2002) 216–225. https://doi.org/10.1016/S0924-0136(02)00454-5.

[59] J. Karimi Kerdabadi, M. Haghanimanesh, A. Karimipour, D. Toghraie, I. Tlili, The experimental/numerical investigation of variations in strip speed, water shower pattern and water temperature on high-temperature strip cooling rate in hot strip mill, Journal of Thermal Analysis and Calorimetry. 143 (2021) 293–308. https://doi.org/10.1007/s10973-019-09052-4.

[60] Y. Zheng, N. Li, S. Li, Hot-rolled strip laminar cooling process plant-wide temperature monitoring and control, Control Engineering Practice. 21 (2013) 23–30. https://doi.org/10.1016/j.conengprac.2012.09.004.

[61] R.-M. Guo, Heat transfer of laminar flow cooling during strip acceleration on hot strip mill runout tables, Iron and Steelmaker. 20 (1993) 49–49.

[62] H. YOSHIDA, Analysis of Flatness of Hot Rolled Steel Strip after Cooling, Transactions of the Iron and Steel Institute of Japan. 24 (1984) 212–220. https://doi.org/10.2355/isijinternational1966.24.212.

[63] A. Milenin, P. Kustra, R. Kuziak, M. Pietrzyk, Model of Residual Stresses in Hot-rolled Sheets with Taking into Account Relaxation Process and Phase Transformation, Procedia Engineering. 81 (2014) 108–113. https://doi.org/10.1016/j.proeng.2014.09.135.

[64] Z. Zhou, P.F. Thomson, Y. Lam, D.D.W. Yuen, Numerical analysis of residual stress in hot-rolled steel strip on the run-out table, Journal of Materials Processing Technology. 132 (2003) 184–197. https://doi.org/10.1016/S0924-0136(02)00850-6.

[65] H.-H. Cho, Y.-G. Cho, D.-W. Kim, S.-J. Kim, W.-B. Lee, H.N. Han, Finite Element Investigation for Edge Wave Prediction in Hot Rolled Steel during Run Out Table Cooling, ISIJ International. 54 (2014) 1646–1652. https://doi.org/10.2355/isijinternational.54.1646.

[66] X. Wang, F. Li, Q. Yang, A. He, FEM analysis for residual stress prediction in hot rolled steel strip during the run-out table cooling, Applied Mathematical Modelling. 37 (2013) 586–609. https://doi.org/10.1016/j.apm.2012.02.042.

[67] S. Sjöström, Interactions and constitutive models for calculating quench stresses in steel, Materials Science and Technology. 1 (1985) 823–829. https://doi.org/10.1179/mst.1985.1.10.823.

[68] W.A. Johnson, R.F. Mehl, Reaction kinetics in processes of nucleation and growth, Trans. Am. Inst. Min. Metall. Eng. 135 (1940) 416–442.

[69] M. Avrami, Kinetics of Phase Change. I General Theory, The Journal of Chemical Physics. 7 (1939) 1103–1112. https://doi.org/10.1063/1.1750380.

[70] E.B. Hawbolt, B. Chau, J.K. Brimacombe, Kinetics of austenite-ferrite and austenite-pearlite transformations in a 1025 carbon steel, Metallurgical Transactions A. 16 (1985) 565–578. https://doi.org/10.1007/BF02814230.

[71] F.M.B. Fernandes, S. Denis, A. Simon, Mathematical model coupling phase transformation and temperature evolution during quenching of steels, Materials Science and Technology. 1 (1985) 838–844. https://doi.org/10.1179/mst.1985.1.10.838.

[72] C.H. Gür, J. Pan, Handbook of thermal process modeling of steels, CRC Press. (2008) 21–23. https://doi.org/10.1179/174951409x12542264514365.

[73] N. Saunders, Z. Guo, A.P. Miodownik, J.-P. Schillé, The Calculation of TTT and CCT diagrams for General Steels, JMatPro Software Literature. (2004).

[74] D.P. Koistinen, R.E. Marburger, A general equation prescribing the extent of the austenite-martensite transformation in pure iron-carbon alloys and plain carbon steels, Acta Metallurgica. 7 (1959) 59–60. https://doi.org/10.1016/0001-6160(59)90170-1.

[75] H. Jasak, H.G. Weller, Application of the finite volume method and unstructured meshes to linear elasticity, International Journal for Numerical Methods in Engineering. 48 (2000) 267–287. https://doi.org/10.1002/(SICI)1097-0207(20000520)48.

[76] M.L. Wilkins, Modeling the Behavior of Materials, in: Theoretical Foundation for Large-Scale Computations for Nonlinear Material Behavior, Springer Netherlands, Dordrecht, 1984: pp. 147–163. https://doi.org/10.1007/978-94-009-6213-2_7.

[77] I. Demirdžic, D. Martinovic, A. Ivankovic, Numerical simulation of thermal deformation in welded workpiece, Zavarivanje. 31 (1988) 209–219.

[78] P. Cardiff, Ž. Tuković, H. Jasak, A. Ivanković, A block-coupled Finite Volume methodology for linear elasticity and unstructured meshes, Computers & Structures. 175 (2016) 100–122. https://doi.org/10.1016/j.compstruc.2016.07.004.

[79] I. Demirdžić, D. Martinović, Finite volume method for thermo-elasto-plastic stress analysis, Computer Methods in Applied Mechanics and Engineering. 109 (1993) 331–349. https://doi.org/10.1016/0045-7825(93)90085-C.

[80] E.C. Bryant, J. Hwang, M.M. Sharma, Arbitrary Fracture Propagation in Heterogeneous Poroelastic Formations Using a Finite Volume-Based Cohesive Zone Model, in: Day 3 Thu, February 05, 2015, SPE, 2015. https://doi.org/10.2118/SPE-173374-MS.

[81] D. Lee, P. Cardiff, E.C. Bryant, R. Manchanda, H. Wang, M.M. Sharma, A New Model for Hydraulic Fracture Growth in Unconsolidated Sands with Plasticity and Leak-Off, in: Day 2 Tue, September 29, 2015, SPE, 2015. https://doi.org/10.2118/174818-MS.

[82] H. Jasak, H.G. Weller, Finite volume methodology for contact problems of linear elastic solids, in: Proceedings of 3rd International Conference of Croatian Society of Mechanics, 2000: pp. 253–260. https://www.researchgate.net/publication/228497087.

[83] P. Cardiff, A. Karač, A. Ivanković, Development of a finite volume contact solver based on the penalty method, Computational Materials Science. 64 (2012) 283–284. https://doi.org/10.1016/j.commatsci.2012.03.011.

[84] I. Demirdžić, S. Muzaferija, Numerical method for coupled fluid flow, heat transfer and stress analysis using unstructured moving meshes with cells of arbitrary topology,

Computer Methods in Applied Mechanics and Engineering. 125 (1995) 235–255. https://doi.org/10.1016/0045-7825(95)00800-G.

[85] C.J. Greenshields, H.G. Weller, A unified formulation for continuum mechanics applied to fluid-structure interaction in flexible tubes, International Journal for Numerical Methods in Engineering. 64 (2005) 1575–1593. https://doi.org/10.1002/nme.1409.

[86] P. Cardiff, I. Demirdžić, Thirty Years of the Finite Volume Method for Solid Mechanics, Archives of Computational Methods in Engineering. 28 (2021) 3721–3780. https://doi.org/10.1007/s11831-020-09523-0.

[87] R. Hill, The mathematical theory of plasticity, Oxford university press, 1998.

[88] A. Afkar, M.N. Camari, A. Paykani, Design and analysis of a spherical pressure vessel using finite element method, World Journal of Modelling and Simulation. 10 (2014) 126–135.

[89] P. Cardiff, A. Karač, P. de Jaeger, H. Jasak, J. Nagy, A. Ivanković, Ž. Tuković, An open-source finite volume toolbox for solid mechanics and fluid-solid interaction simulations, ArXiv Preprint ArXiv:1808.10736. (2018).

[90] H. Sadiq, M.B. Wong, J. Tashan, R. Al-Mahaidi, X.-L. Zhao, Determination of Steel Emissivity for the Temperature Prediction of Structural Steel Members in Fire, Journal of Materials in Civil Engineering. 25 (2013) 167–173. https://doi.org/10.1061/(ASCE)MT.1943-5533.0000607.

[91] N. Mansouri, M. Mirhosseini, A. Saboonchi, Thermal modeling of strip across the transfer table in the hot rolling process, Applied Thermal Engineering. 38 (2012) 91–104. https://doi.org/10.1016/j.applthermaleng.2011.12.049.

[92] C. Ma, W. He, H. Qiao, C. Zhao, Y. Liu, J. Yang, Flow Field in Slab Continuous Casting Mold with Large Width Optimized with High Temperature Quantitative Measurement and Numerical Calculation, Metals (Basel). 11 (2021) 261. https://doi.org/10.3390/met11020261.

[93] J. Selker, O. Dani, Heat Flow and Thermal Effects in Soil, in: Soil Hydrology and Biophysics, Oregon State University, 2021: pp. 243–266.

[94] S.I. Luk'yanov, N.V. Shvidchenko, S.S. Krasilnikov, R.S. Pishnograev, D.V. Shvidchenko, M.V. Konovalov, Optimizing speed of a run-out table of the hot strip mill, The International Journal of Advanced Manufacturing Technology. 105 (2019) 1675–1684. https://doi.org/10.1007/s00170-019-04324-7.

[95] D.E. Hall, F.P. Incropera, R. Viskanta, Jet Impingement Boiling From a Circular Free-Surface Jet During Quenching: Part 1—Single-Phase Jet, Journal of Heat Transfer. 123 (2001) 901–910. https://doi.org/10.1115/1.1389061.

[96] H. Wang, W. Yu, Q. Cai, Experimental study of heat transfer coefficient on hot steel plate during water jet impingement cooling, Journal of Materials Processing Technology. 212 (2012) 1825–1831. https://doi.org/10.1016/j.jmatprotec.2012.04.008.

[97] H. Leocadio, J.C. Passos, Experimental investigation of heat transfer characteristics during water jet impingement cooling of a high-temperature steel surface, Ironmaking & Steelmaking. 48 (2021) 819–832. https://doi.org/10.1080/03019233.2021.1872467.

[98] S. Sikdar, A. Mukhopadhyay, Numerical determination of heat transfer coefficient for boiling phenomenon at runout table of hot strip mill, Ironmaking & Steelmaking. 31 (2004) 495–502. https://doi.org/10.1179/030192304225019306.

[99] C. Charles, Microstructure model for Ti-6Al-4V used in simulation of additive manufacturing, Doctoral thesis, Luleå University of Technology, 2016.